

UNIVERSIDADE DE SÃO PAULO  
INSTITUTO DE FÍSICA DE SÃO CARLOS

Erika Toneth Ponce Ayala

**Analysis of sono-photodynamic effects with PpIX - *in vitro* and *in vivo* studies**

São Carlos

2020



**Erika Toneth Ponce Ayala**

**Analysis of sono-photodynamic effects with PpIX - *in vitro* and *in vivo* studies**

Dissertation submitted to the Post Graduate Program in Physics at the Instituto de Física de São Carlos, Universidade de São Paulo to obtain the Master degree in Science.

Concentration area: Applied Physics

Advisor: Prof. Dr. Sebastião Pratavieira

**Corrected version**  
**(Original version available on the Program Unit)**

**São Carlos**  
**2020**

I AUTHORIZE THE REPRODUCTION AND DISSEMINATION OF TOTAL OR PARTIAL COPIES OF THIS DOCUMENT, BY CONVENTIONAL OR ELECTRONIC MEDIA FOR STUDY OR RESEARCH PURPOSE, SINCE IT IS REFERENCED.

Ponce Ayala, Erika Toneth

Analysis of sono-photodynamic effects with PpIX - in vitro and in vivo studies / Erika Toneth Ponce Ayala; advisor Sebastião Pratavieira - corrected version -- São Carlos 2020.

105 p.

Dissertation (Master's degree - Graduate Program in Applied Physics) -- Instituto de Física de São Carlos, Universidade de São Paulo - Brasil , 2020.

1. Sonodynamic therapy. 2. Photodynamic therapy. 3. Protoporphyrin IX. 4. Spectroscopy analysis. 5. Rat liver necrosis. I. Pratavieira, Sebastião, advisor. II. Title.

*With love to my godmother Nancy Lopez and my aunt Facunda Ayala, who died this year and unfortunately I could not say goodbye as I wished. I keep the best memories of you, I will always carry them in my heart.*



## ACKNOWLEDGEMENTS

I would like to thank God for always taking care of me, guiding me through the stormy path of life, giving me the opportunity day by day to grow as a person, as a professional, to enjoy life and give back to it giving my best. Thank you for, without a doubt, the most precious treasure I have: my beautiful family. I am very thankful to my parents Neil and Redina, for the love and education they gave me, for the effort they made so that nothing ever lacks me, and I could continue chasing my goals and dreams. Thank you so much for always trusting me, making me feel so safe and comforted in moments of weakness. I thank my sisters, Emily and Tamara, my two little princesses whom I adore and who without knowing it, turned my troubled days into the most fun and endearing. I would also like to thank my grandparents, uncles, cousins and nephews, both paternal and maternal ones, whose messages during this time outside my country helped me to feel not that far from home.

This project would not have been possible without the support of Prof. Dr. Vanderlei Bagnato, whose trust in me I will always be sincerely thankful for. You are a model and motivation for me so that, just like you, I can work honestly in favor of Science and, through it, give back to society some of what I received.

I would like to thank my advisor, Prof. Dr. Sebastião Pratavieira, for his guidance and teachings at each step of this process, for always looking for opportunities so that I can develop and grow as a scientist, but also for showing me a friendlier side that made him not only my advisor but also a friend whom I could trust. I am very thankful to Dr. Fernanda Alves and Dr. José Dirceu Vollet Filho, for the time they dedicated to my research, for the teachings and support they gave me when I had to develop procedures that had never been done before but which, with their advice, I finally succeeded to achieve. Thank you very much for this! No doubt you were key pieces during the development of this study. I am thankful to Dr. Michelle Requena, Dr. Marlon Garcia and René Casarin, who cordially made themselves available in cases of technical assistance and clear many of my doubts.

I want to thank very much my boyfriend Claver, whose words of comfort and motivation helped me to keep going and fighting for my goals. I thank my best friends Kimberly, Leslie and Lucero, my sisters at heart, infinite thanks for this sincere friendship of ours. I thank my friends Gastón, José, Edward, Victor, Yordania, Loraine, Claudia and Johan. My stay in a different country, far from home, was very pleasant thanks to them.

Finally, the present work was carried out thanks to the support provided by Brazilian Funding Agencies: Coordenação de Aperfeiçoamento de Pessoal de Nível Superior - Brasil (CAPES) - Finance Code 001; CNPq (465360/2014-9 and 306919/2019-2) and

São Paulo Research Foundation (FAPESP) grants: 2013/07276-1 (CEPOF); 2014/50857-8 (INCT).



*“Each has the age of his heart, his experience, his faith.”*

*George Sand*



## ABSTRACT

PONCE AYALA, E.T. **Analysis of sono-photodynamic effects with PpIX** - *in vitro* and *in vivo* studies. 2020. 105p. Dissertation (Master in Science) - São Carlos Institute of Physics, University of São Paulo, São Carlos, 2020.

Sono-photodynamic therapy (SPDT) is a relatively new and promising approach to cancer treatment, based on the combination of an sono-photoactive drug, low-intensity ultrasound and light. This combined therapy increases anticancer effects by the induction of cell death into deeper body regions. This study aims to analyze the mechanisms and effects of the sono-photodynamic (SPD) action on Protoporphyrin IX (PpIX) solutions and PpIX-loaded rat healthy liver. *In vitro*, PpIX 5 $\mu$ M solutions were irradiated with light (635 nm, 30-50  $mW/cm^2$ ) (photodynamic (PD) action), ultrasound (1MHz, 1-2  $W/cm^2$ ) (sonodynamic(SD) action) and the combination of both sources. This combination was carried out in three different ways: applying both sources simultaneously (SPD action) and applying one source after the other (PD+SD and SD+PD action). The absorption spectra of PpIX solutions recorded during irradiation, showed that the PpIX decay rate ( $k$ ) induced by SPD action was approximately the sum of those induced by the PD and SD action ( $k_{SPD} \simeq k_{SD} + k_{PD}$ ). *In vivo*, rats were intraperitoneal injected with 5-aminolevulinic acid (ALA) at doses of 500 mg/kg body weigh to load the rat liver with higher concentration of PpIX. At 3h (time of optimum drug concentration in the liver) after injection, the PpIX-loaded livers were irradiated with light (635 nm,  $180 \pm 9 J/cm^2$ ) (PD action), ultrasound (1.0 MHz,  $765 \pm 38 J/cm^2$ ) (SD action), and the combination of both sources (SPD, PD+SD, SD+PD action). For these procedures, a single probe capable of irradiating light and ultrasound simultaneously was built. After 30 hours, animals were sacrificed, the livers were surgically removed and analyzed through scanned histological slides. The SPD and PD+SD action induced greater necrosis depth than either PD or SD action. These results suggested that the combined action could improve the drug decay rate, as well as having a greater scope than either PD or SD action, but it certainly must be more widely studied.

**Keywords:** Sonodynamic therapy. Photodynamic therapy. Protoporphyrin IX. Spectroscopy analysis. Rat liver necrosis.



## RESUMO

PONCE AYALA, E.T. **Análise dos efeitos sono-fotodinâmicos com PpIX** - estudos *in vitro* e *in vivo*. 2020. 105p. Dissertação (Mestrado em Ciências) - São Carlos Institute of Physics, University of São Paulo, São Carlos, 2020.

A terapia sonofotodinâmica (TSFD) é uma abordagem relativamente nova e promissora para o tratamento do câncer, baseada na combinação de uma droga sono-fotoativa, ultrassom de baixa intensidade e luz. Esta terapia combinada aumenta os efeitos anticâncer pela indução da morte celular em regiões mais profundas do corpo. Este estudo tem como objetivo analisar os mecanismos e efeitos da ação sono-fotodinâmica (SFD) em soluções de Protoporfirina IX (PpIX) e em fígado de rato saudável na presença de PpIX. *In vitro*, as soluções PpIX 5  $\mu\text{M}$  foram irradiadas com luz (635 nm, 30-50  $\text{mW}/\text{cm}^2$ ) (ação fotodinâmica (FD)), ultrassom (1 MHz, 1-2  $\text{W}/\text{cm}^2$ ) (ação sonodinâmica (SD)) e a combinação de ambas as fontes. Esta combinação foi realizada de três maneiras diferentes: aplicando ambas as fontes simultaneamente (ação SFD) e aplicando uma fonte após a outra (ação FD+SD e ação SD+FD). Os espectros de absorção das soluções da PpIX registrados durante a irradiação, mostraram que a taxa de decaimento de PpIX ( $k$ ) induzida pela ação SFD foi aproximadamente a soma daquelas induzidas pela ação FD e SD ( $k_{SFD} \simeq k_{SD} + k_{FD}$ ). *In vivo*, os ratos foram injetados por via intraperitoneal com 5-aminolevulínico (ALA) em doses de 500 mg/kg do peso corporal. Após 3 horas da injeção (tempo para a concentração ideal do fármaco no fígado), os fígados carregados com PpIX foram irradiados com luz (635 nm,  $180 \pm 9 \text{ J}/\text{cm}^2$ ) (ação FD), ultrassom (1,0 MHz,  $765 \pm 38 \text{ J}/\text{cm}^2$ ) (ação SD) e a combinação de ambas as fontes (ação SFD, FD+SD, SD+FD). Para esses procedimentos, foi construída uma única sonda capaz de irradiar luz e ultrassom simultaneamente. Após 30 horas, os animais foram sacrificados, os fígados foram removidos cirurgicamente e analisados através de lâminas histológicas digitalizadas. A ação SFD e FD+SD induziram maior profundidade de necrose do que a ação FD ou SD. Esses resultados sugerem que a ação combinada pode melhorar a taxa de degradação da droga utilizada como sensibilizador, além de ter um escopo maior do que a ação PD ou SD, mas certamente deve ser mais amplamente estudada.

**Palavras-chave:** Terapia sonodinâmica. Terapia fotodinâmica. Protoporfirina IX. Análise espectroscópica. Necrose fígado de rato.



## LIST OF FIGURES

Figure 1 – Clinical photodynamic therapy. DLI: Drug-light interval. <i>PS*</i> : active photosensitizer. . . . .	29
Figure 2 – Electromagnetic spectrum and schematic representation of an EMW. . . . .	30
Figure 3 – Light interaction with a biological tissue: (a) light refraction according Snell’s Law, where $v_1, n_1$ and $v_2, n_2$ are the light speed and the refraction index of the surrounding media and tissue, respectively; (b) light reflection on the surface of a tissue according Fresnel’s Law, where $\phi_1$ and $\phi_2$ are the incident and reflection angle respectively; (c) absorption phenomena according to Lambert-Beer’s law, where $I_0$ is the incident light intensity, $I_x$ is the light intensity after light propagation at a depth $x$ in the tissue, and $\phi_{abs}$ is the tissue absorbance coefficient; (d) scattering phenomena. . . . .	31
Figure 4 – (A) Optical window for PDT in tissue defined by the absorption spectra of tissue chromophores. (B) Light penetration depth in tissue according light wavelength. Light with a longer wavelength propagates through the tissue more deeply. . . . .	32
Figure 5 – Examples of light sources for clinical PDT. (A) Diode lasers with fiber-optic light delivery applied by (B) interstitial irradiation. (C) PDT treatment using the large area probe of a LED-based device (Lince, Brazil). (D) PDT device based on narrow LED strips. (E) Tungsten filament lamp and (F) Fluorescent lamps in a U form used for ALA-PpIX skin treatments. . . . .	35
Figure 6 – Diagram of energy levels and their respective transitions proposed by Alexander Jablonsky. IC: internal conversion, ISC: intersystem crossing, VR: vibrational relaxation, $S_x$ : PS singlet states, $T$ : PS triplet state. . . . .	36
Figure 7 – Schematic representation of PDT-induced effects on tumor cells, tumor tissue and immune system. . . . .	37
Figure 8 – Three major cell death morphotypes induced by PDT: (A) apoptotic, (B) necrosis and (C) autophagy. (D) Morphological features of apoptotic, necrotic and autophagic cells. The scale bar represents 1 $\mu\text{m}$ . . . . .	38
Figure 9 – Schematic overview of both PDT and SDT against cancer. The PS or SS is administered systematically or locally into the tumor tissue, followed by light or ultrasound irradiation, respectively. The light-PS and ultrasound-SS interaction generates chemical and physical effects that lead to tumor cells eradication. . . . .	39

Figure 10 – (A) Acoustic wave range. (B) Schematic representation of an acoustic wave (sinusoidal waveform). C: Compression phase and R: Rarefaction phase. (C) Representations of (i) longitudinal and (ii) transverse or shear waves. . . . .	40
Figure 11 – Three reaction zones in the cavitation process. . . . .	43
Figure 12 – Acoustic cavitation of microbubbles: Non inertial or stable cavitation and inertial or transient cavitation. . . . .	44
Figure 13 – Bubble growth and implosion in a sonicated liquid, is the physical phenomenon responsible for sonochemical effects during inertial cavitation. Dark color regions: $+\Delta P$ , Light color regions: $-\Delta P$ . . . . .	45
Figure 14 – Some of the sonochemical reactions identified in the cavitational events	46
Figure 15 – Ultrasound-tissue interactions. . . . .	47
Figure 16 – Ultrasound penetration depth according ultrasound frequency. The lower the output frequency is, the deeper will be the penetration into the tissues. . . . .	48
Figure 17 – Chemical structures of (A) porphyrin-based sonosensitizers, (B) xanthene-based sonosensitizers, (C) non-steroidal anti-inflammatory drug-based sonosensitizers, and (D) other sonosensitizers. . . . .	49
Figure 18 – (A) Lateral and face view of the transducer shows its components and the effective radiating area (ERA). The piezoelectric crystal produces the ultrasonic energy, but ERA is through which majority of the energy is emitted. (B) The reverse piezoelectric effect leads piezoelectric crystal expands and contracts, producing positive and negative electrical charges. (C) Rarefaction and compression of molecules by ultrasound. . . . .	50
Figure 19 – (A) Continuous and pulsed mode. Pulse period is the sum of the pulse duration time (pulse width) plus the time between ultrasonic pulses (pulse interval). Pulse width is composed by a small number of cycles. (B) Relationship between ultrasound output mode and temperature. Over time, pulsed output still results in small increases in tissue temperature, but does not reach therapeutic ranges. . . . .	51
Figure 20 – The schematic representation of an ultrasound beam shows the irregular intensity of the near field and the spatial peak intensity in the far field.	52
Figure 21 – <b>Sonomechanical SDT mechanisms.</b> They are based on the interaction of <i>microjetting</i> , <i>microstreaming</i> , and <i>shock waves</i> phenomena with the destabilized cell membrane. . . . .	53



Figure 22 – <b>Sonochemical SDT mechanisms.</b> Though inertial cavitation phenomenon is possible to trigger sonoluminescence and high levels of heat (4000-25,000 K), which interact with nearby sonosensitizers (shown in green) by (a) a PDT-like mechanism and (b) pyrolysis respectively. As a result of this interaction reactive oxygen species are generated, inducing cellular death. . . . .	54
Figure 23 – PpIX absorption and fluorescence spectrum, with a dominant peak at 407nm and 635 nm, respectively. . . . .	55
Figure 24 – Chemical structures of (A) 5-ALA and (B) PpIX. . . . .	56
Figure 25 – Light and US source devices: (A) LINCÉ and (B) SONOMED IV. . . . .	59
Figure 26 – Experimental setup for experiments of the SPD group. . . . .	62
Figure 27 – The sono-photodynamic probe is composed by an ultrasound transducer with the implementation of a UV-Visible optical fiber positioned in the middle. . . . .	63
Figure 28 – Overview scheme of the experimental setup for liver steady state measurements. . . . .	64
Figure 29 – Simultaneous irradiation on PpIX-loaded rat liver using (A) the sono-photodynamic probe connected to (B) a multifiber diode laser and (C) an ultrasound machine. . . . .	65
Figure 30 – Flow chart of each protocol. US:ultrasound, RL:red light . . . . .	66
Figure 31 – The absorption spectra of (A) DMSO, and (B) PpIX 1, (C) 3, (D) 5, (E) 10 and (F) 20 $\mu\text{M}$ before and after each 3 minutes of sonication - SD action. . . . .	69
Figure 32 – The absorption spectrum of a PpIX 5 $\mu\text{M}$ solution diluted in DMSO and $\text{H}_2\text{O}_2$ with different percentages (1-50%) of $\text{H}_2\text{O}_2$ . . . . .	70
Figure 33 – (A) The mean absorbance values at 280 nm over sonication time. (B) The mean absorbance values at 280 nm before and after ultrasound irradiation for each solution (1-20 $\mu\text{M}$ ). The solid line and error bars represent the linear fit and standard deviation, respectively. . . . .	71
Figure 34 – Graphic representation of the natural logarithm of the mean normalized absorbance at (A) Soret band (1-20 $\mu\text{M}$ ) and (B) Q bands (PpIX 20 $\mu\text{M}$ ) over sonication time. (C) The mean absorbance at Soret band before and after sonication. (D) The mean number of decomposed moles of PpIX by 15 min of sonication (purple bars). Solid line and error bars represent the linear fit and standard deviation, respectively. . . . .	72
Figure 35 – (A) The mean Sp formation rate $k_{Sp}$ at approx. 280 nm and (B) the mean PpIX decay rate $k_{PpIX}$ at Soret band according the PpIX initial concentration. The error bars represent the standard deviation. . . . .	72

Figure 36 – The absorption spectrum of PpIX solution before and after being heated up to 45 °C . . . . .	73
Figure 37 – (A) The mean Sp absorbance at 280 nm and (B) the natural logarithm of the mean PpIX normalized absorbance at Soret band during 15 min of ultrasound irradiation and 12 hours after that. Error bars represent the standard deviation. . . . .	73
Figure 38 – The absorption spectra and temperature of the PpIX 5 $\mu$ M solution each 5 min of sonication with pulse repetition frequency of 100 Hz, duty cycle of 50% and ultrasound intensity of (A) 1, (B) 1.5 and (C) 2 $W/cm^2$ . . . . .	74
Figure 39 – (A) The absorption spectra and temperature of the PpIX 5 $\mu$ M solution before and after 30 min of sonication with three different US intensities. (B) Graphic representation of the natural logarithm of the mean normalized absorbance of PpIX at Soret band over sonication time. (C) Mean absorbance at 280 nm band over sonication time. Error bars represent the standard deviation. . . . .	75
Figure 40 – The absorption spectra and temperature of the PpIX 5 $\mu$ M solution each 5 min of red light irradiation with irradiance of (A) 30 and (B) 50 $mW/cm^2$ . . . . .	76
Figure 41 – (A) The absorption spectra and temperature of the PpIX 5 $\mu$ M solution before and after 30 min of illumination with two different irradiances. (B) Graphic representation of the natural logarithm of the mean normalized absorbance of PpIX at Soret band over illumination time. (C) Mean absorbance at 670 nm band over illumination time. The error bars represent the standard deviation. . . . .	77
Figure 42 – The absorption spectra and temperature of the PpIX 5 $\mu$ M solution each 5 min of simultaneous US and light irradiation. The US intensity and irradiance applied were: (A) 1 $W/cm^2$ -50 $mW/cm^2$ , (B) 1.5-30, (C) 1.5-50 and (D) 2-30, respectively. . . . .	78
Figure 43 – (A) The absorption spectra and temperature of the PpIX 5 $\mu$ M solution before and after 30 min of both ultrasound and light irradiation simultaneously under four different intensity values; (B) Graphic representation of the natural logarithm of the mean normalized absorbance of PpIX at Soret band over irradiation time. Solid line and error bars represent the linear fit and standard deviation, respectively. . . . .	79
Figure 44 – The mean absorbance at (A) 280 nm and (B) 670 nm over irradiation time, under SPD action. Error bars represent the standard deviation. . . . .	80
Figure 45 – The absorption spectra and temperature of the PpIX 5 $\mu$ M solution each 5 min of irradiation during PD+SD action. . . . .	80
Figure 46 – The absorption spectra and temperature of the PpIX 5 $\mu$ M solution each 5 min of irradiation during SD+PD action. . . . .	81

Figure 47 – The mean absorbance at (A) 280 nm and (B) 670 nm over irradiation time under PD+SD and SD+PD action. Error bars represent the standard deviation.	81
Figure 48 – (A) The absorption spectra and the temperature of the PpIX solutions after 30 min of irradiation for each action; (B) Graphic representation of the natural logarithm of the mean normalized absorbance of PpIX at Soret band over irradiation time. Applying U.S. intensity of $1.5 W/cm^2$ and irradiance of $30 mW/cm^2$ . The solid line and error bars represent the linear fit and standard deviation, respectively.	82
Figure 49 – The amount of decomposed PpIX moles by SD, PD, SPD, PD+SD and SD+PD action.	83
Figure 50 – (A) The sonoproducts formation in 280nm band and (B) the photoproducts formation in 670nm band during PD+SD, SD+PD and SPD action.	83
Figure 51 – The not normalized fluorescence spectra recorded before ALA administration, during 3 hours of ALA accumulation, and immediately after (A) SD, (B) PD, (C) SPD, (D) SD+PD and (E) PD+SD action. Maximum fluorescence intensity was detected at 635 nm. Fluorescence emission was scanned from 500 to 800 nm.	84
Figure 52 – (A) Normalized fluorescence intensity at 630 nm band recorded at 0, 60, 120 and 180 min after ALA administration. (B) Normalized fluorescence intensity at 630 nm band recorded after treatment at 197 min (SD, PD and SPD action) and 214 min (PD+SD, SD+PD action). The symbols and error bars represent the mean experimental values and standard deviation, respectively.	85
Figure 53 – Necrosis area: on the rat liver after 30 hours of apply the (a) SD, (b) PD, (c) SPD, (d) PD+SD and (e) SD+PD action. (1) Front side, (2) Reverse side.	86
Figure 54 – Digitized histological slides of liver tissue: (left) the necrosis area and (right) the transition between necrotic (N) and healthy (H) tissue induced by each action. The bars in the left column represents $1000 \mu m$ for SD and PD group; $2000 \mu m$ for SPD group. The bars in the right column represents $100 \mu m$ .	87
Figure 55 – Image processing of the scanned histological slides by the random forest method, showing (yellow region) the necrotic and (green region) non-damaged tissue induced by each action.	88
Figure 56 – Measurements of the mean damaged and non-damaged area obtained through image processing in (A) pixel squared and (B) percentage. Bars represent the SD.	89
Figure 57 – Approval of the proposal with protocol No. 2564110719.	104
Figure 58 – Approval of the proposal amendment with protocol No. 2564110719.2	105



## LIST OF TABLES

Table 1 – Several PS broad families like: porphyrins, chlorophylls and dyes. . . . .	33
Table 2 – Properties of an ideal photosensitizer. <sup>1,2</sup> . . . . .	34
Table 3 – Overview of kinetics of photosensitization during PDT. S: photosensitizer, RH: substrate with H-bond, $S_x$ singlet-state molecule, $T_x$ triplet-state molecule. . . . .	37
Table 4 – Propagation speed of ultrasonic waves according the physical medium where they are propagating through. $\gamma$ : ratio of specific heats, $P_0$ : ambient pressure, $\rho$ : medium's density, $B_T$ : isothermal bulk modulum, $\sigma$ : Poisson's ratio, and Y: Young's modulus. . . . .	41
Table 5 – Ultrasound propagation speed in Biological and Nonbiological Material. Ultrasound speed is greater in materials that are more rigid or less compressible. . . . .	41
Table 6 – Sonomechanical and sonochemical effects through acoustic cavitation. . . . .	44
Table 7 – Percent reflection of ultrasonic energy at various interfaces. . . . .	47
Table 8 – Ultrasound Output Parameters and Measures. . . . .	51
Table 9 – The mean PpIX decay rate ( $k$ ) at Soret band for each action and the additive decay rates ( $k_a$ ) for the combined action. Average $\pm$ standard deviation. . . . .	81



## LIST OF ABBREVIATIONS AND ACRONYMS

ALA	$\delta$ -aminolevulinic acid
DLI	Drug-light interval
DMSO	Dimethyl sulfoxide
DVDMS	Sinoporphyrin sodium
EMW	Electromagnetic wave
ERA	Effective radiating area
INCA	National cancer institute
LASER	Light amplification by stimulated emission of radiation
LED	Light emitting diode
PCD	Programmed cell death
PDT	Photodynamic Therapy
PDT dose	Dose in photodynamic therapy
PpIX	Protoporphyrin IX
Pp	Photoproducts
PS	Photosensitizer
ROS	Reactive oxygen species
RPE	Rayleigh-Plesset equations
SDT	Sonodynamic Therapy
SF1	Sonoflora 1TM
SPDT	Sono-photodynamic Therapy
Sp	Sonoproducts
SS	Sonosensitizer





## LIST OF SYMBOLS

$H_2O_2$	Hydrogen peroxide
$HO^\cdot$	Hydroxyl radicals
$^3O_2$	Molecular oxygen
$\tau$	Photobleaching time
$k$	PpIX decay rate
$^1O_2$	Singlet oxygen
$k_{Pp}$	Photoproducts formation rate
$k_{Sp}$	Sonoproducts formation rate
$O_2^\cdot-$	Superoxide anions



## CONTENTS

<b>1</b>	<b>INTRODUCTION</b>	<b>27</b>
<b>1.1</b>	<b>Photodynamic therapy: Basic principles</b>	<b>29</b>
1.1.1	Light	29
1.1.1.1	Interaction of light with biological tissue	31
1.1.2	Photosensitizers	33
1.1.3	Light sources for PDT	34
1.1.4	Photophysics and photochemistry process in PDT	34
1.1.5	Mechanisms of PDT-mediated target cell death	37
<b>1.2</b>	<b>Sonodynamic therapy: Basic principles</b>	<b>39</b>
1.2.1	Ultrasound	39
1.2.1.1	Acoustic Cavitation	42
1.2.1.2	Interaction of ultrasound with biological tissue	46
1.2.2	Sonosensitizers	48
1.2.3	Ultrasound source for SDT	50
1.2.4	Sonophysics and sonochemistry process in SDT	52
1.2.5	Mechanism of SDT-mediated target cell death	54
<b>1.3</b>	<b>Protoporphyrin IX as a sono-photosensitizing agent</b>	<b>55</b>
<b>2</b>	<b>OBJECTIVES</b>	<b>57</b>
<b>2.1</b>	<b>General objective</b>	<b>57</b>
<b>2.2</b>	<b>Specific objectives</b>	<b>57</b>
2.2.1	<i>in vitro</i> procedures	57
2.2.2	<i>in vivo</i> procedures	57
<b>3</b>	<b>MATERIALS AND METHODS</b>	<b>59</b>
<b>3.1</b>	<b><i>In vitro</i> experiments</b>	<b>59</b>
3.1.1	Sono-photosensitizer	59
3.1.2	Light and ultrasound source devices	59
3.1.3	Analysis of the PpIX absorption spectrum	60
3.1.3.1	PpIX degradation mediated by ultrasound and light irradiation.	60
3.1.3.2	PpIX modification mediated by ultrasound and light irradiation.	60
3.1.4	Experimental procedures	61
3.1.4.1	SD action at different PpIX concentrations.	61
3.1.4.2	SD, PD and combined action at different source intensities.	61
3.1.5	Macroscopic and microscopic analysis	62
3.1.5.1	Statistical analysis	62

<b>3.2</b>	<b><i>In vivo</i> experiments</b>	<b>62</b>
3.2.1	Animals	62
3.2.1.1	Administration of ALA	63
3.2.2	Sono-photodynamic system	63
3.2.3	Fluorescence detection of PpIX in liver	64
3.2.4	Experimental design	64
3.2.5	Macroscopic and microscopic analysis	66
<b>4</b>	<b>RESULTS AND DISCUSSION</b>	<b>69</b>
<b>4.1</b>	<b><i>In vitro</i> experiments</b>	<b>69</b>
4.1.1	Effects of SD action on PpIX solutions with different concentrations.	69
4.1.2	Effects of the SD, PD and SPD action on PpIX solutions at different source intensities.	73
4.1.3	Spectroscopic comparison among SD, PD, SPD, PD+SD and SD+PD action	82
<b>4.2</b>	<b><i>In vivo</i> experiments</b>	<b>84</b>
4.2.1	Fluorescence detection of PpIX in rat liver	84
4.2.2	Macroscopic observations.	85
4.2.3	Histological observations.	86
<b>5</b>	<b>CONCLUSIONS</b>	<b>91</b>
	<b>REFERENCES</b>	<b>93</b>
	<b>ANNEX</b>	<b>101</b>
	<b>ANNEX A – CERTIFICATE OF THE ETHICS COMMITTEE IN THE USE OF ANIMALS (CEUA) OF THE SAO CARLOS INSTITUTE OF PHYSICS (IFSC)</b>	<b>103</b>

## 1 INTRODUCTION

Cancer is the main public health problem in the world and is already among the top four causes of premature death (before the age of 70) in most countries. According to the estimate of the National Cancer Institute (INCA), there will be 625 thousand new cases of cancer each year between 2020-2022 in Brazil.<sup>3</sup> Conventional clinical treatments against cancer such as surgery, radiotherapy, chemotherapy and immunotherapy have beneficial effects in the fight against cancer. However, they can cause side and psychological effects at patients which temporarily or permanently worsen the patient life quality. Besides, all these treatments have some limitations, like treating metastatic tumors in case of surgery, tolerance exerted by cancer cells during a long period of radiotherapy and chemotherapy, the high price of immunotherapy or refractory cancer cases. So, searching for new alternative therapies becomes extremely necessary.

Photodynamic therapy (PDT) is an anticancer and antimicrobial modality with highly selective cytotoxic process toward target cells, based in the interaction of light, a photoactive drug (photosensitizer, PS) and molecular oxygen ( $^3O_2$ ). PDT has been gaining space within the modalities of cancer treatment in the world, being indicated as a non invasive first-line treatment for non-melanoma skin cancer by several scientific societies worldwide.<sup>4,5</sup> However, the light attenuation through biological tissues hinders to deliver the sufficient energy to deep-seated targets, limiting the success of PDT to superficial skin lesions with less than 2.0 mm of infiltration.<sup>6,7</sup> So, the PDT treatment of some deep early stage tumors like prostate, brain and lung tumors employs flexible fiber-optics for the light delivery applied by interstitial irradiation.<sup>8,9</sup>

Sonodynamic therapy (SDT) is a promising approach for cancer treatment, based on the synergistic effects of low-intensity ultrasound and a sonoactive drug (sonosensitizer, SS). Unlike visible light, ultrasound has an excellent penetration in biological tissues what allows the sonomechanical and sonochemical ultrasound-SS interaction at deeper body regions and the consequent target cell death.<sup>10,11</sup> Although, the deep understanding of the mechanisms behind SDT-mediated cytotoxic effects is still lacking, there are three potential mechanisms mediated by acoustic cavitation that could explain the complexity of the SDT process.<sup>12</sup> The first one is about severe mechanical forces (i.e., microjets, microstreaming and shock waves) which leading to cell lysis after membrane destabilization by the SS.<sup>13</sup> The second one is sonoluminescence, phenomenon involving the transduction of sound into light which originates the photoactivation of SS through the PDT mechanism.<sup>14-16</sup> The third one is high focal heat bringing about SS pirolysis and reactive oxygen species (ROS) formation, predominantly hydroxyl radicals.<sup>17-19</sup> SDT was firstly raised by Umemura *et al.* in 1990 noting that hematoporphyrin can be activated by ultrasound leading to significant

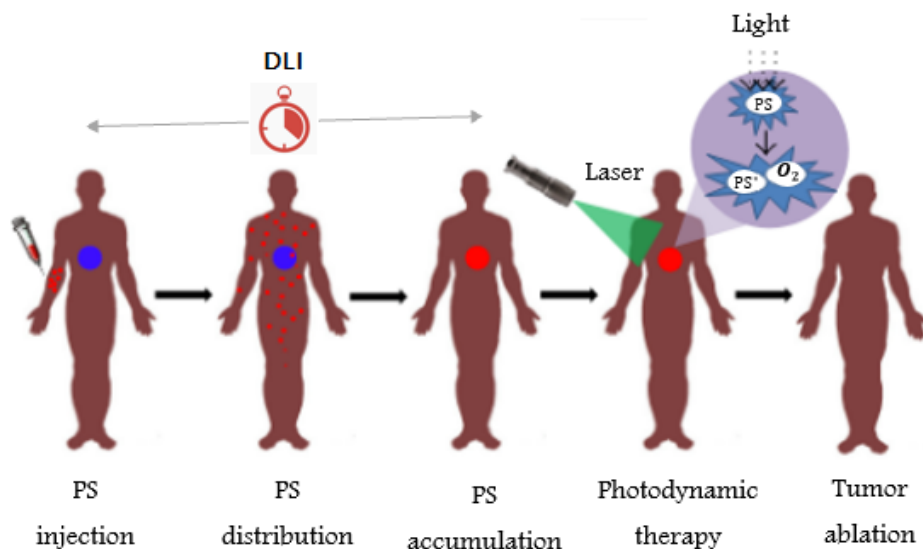
antitumor effects.<sup>15</sup>

An important challenge worldwide is to enable PDT application at deep-seated cancer. That is why studies about: the optimization of drug delivery, the use of flexible fiber-optic devices or the combination of PDT with other therapeutic approaches continue so far.<sup>8,20</sup> The latter point is the case of the sono-photodynamic therapy (SPDT) based on the combined use of PDT and SDT generating higher levels of ROS than either PDT or SDT alone, which justifies the growing interest on it. Several experiments applying the combined action has been increasingly reported until now. Yichen Liu *et al.* noted that using Sinoporphyrin sodium (DVDMS) as sensitizer, the SPD action caused mitochondrial membrane potential loss and excess level of ROS generation, inducing more evident cell apoptosis than either monotherapy (PDT or SDT); besides that, SPDT inhibited tumor growth and metastasis in mouse breast cancer 4T1 xenograft model significantly.<sup>21</sup> Jin *et al.* showed that SPDT applied in a transplantable mouse squamous cell carcinoma model using two sensitizers: PH-1126 and 4TX-70, had an additive effect at inhibition of tumor growth and enhanced in 2-3 times the depth of induced-tumor necrosis. In addition to the preclinical studies, some clinical trials have been developed.<sup>22</sup> Wang *et al.* reported that SPDT using a sublingual sensitizer, Sonoflora 1TM (SF1), had significant partial and complete outcomes in 3 advanced refractory breast cancer cases with failed response to conventional therapy.<sup>23</sup> Kenyon *et al.* applied SPDT using a sublingual sensitizer, Sonnelux-1, in a case series of 115 patients with a variety of cancer diagnoses over 4 years reporting extension in median survival times, control tumor progression and reduction tumor mass.<sup>24,25</sup> Li *et al.* reported that SPDT using two new chlorophyll derived sono-photo-sensitizing agents, dramatically enhanced the conventional therapeutic efficacy in patients with pathologically proven advanced refractory esophagocadiac and gastric adenocarcinoma.<sup>26</sup>

In the literature, *in vivo*, *in vitro* and clinical studies applying SPDT used a protocol for energy delivery that consists of light irradiation followed by ultrasound irradiation or vice-versa. There is no literature regarding the application of simultaneous light and ultrasound irradiation during SPDT. In this work we compared the effects induced by the photodynamic (PD), sonodynamic (SD) and the combined action on protoporphyrin IX (PpIX) solutions (*in vitro* phase) and PpIX-loaded rat healthy liver (*in vivo* phase). The combined action was carried out by irradiating with light and ultrasound simultaneously (SPD action) and irradiating one source after the other (SD+PD action, PD+SD action). In addition, a prototype device capable of simultaneously delivering light and ultrasound to the tissue was developed for use at *in vivo* stage.

## 1.1 Photodynamic therapy: Basic principles

PDT is an anticancer modality shown at Figure 1 that requires the presence of three principal components: light, PS and molecular oxygen ( $^3O_2$ ). These components are non-toxic individually, but together through photophysics and photochemistry processes they can generate ROS (mainly singlet oxygen) that induce tumor cell death<sup>2</sup>. PDT clinical protocol initiates with the topical or systemic administration of a photoactive drug (photosensitizer, PS) followed by visible light-based irradiation of PS-loaded target tissue. The light-PS- $^3O_2$  interaction leads to production of ROS inducing target cell death.<sup>6</sup>



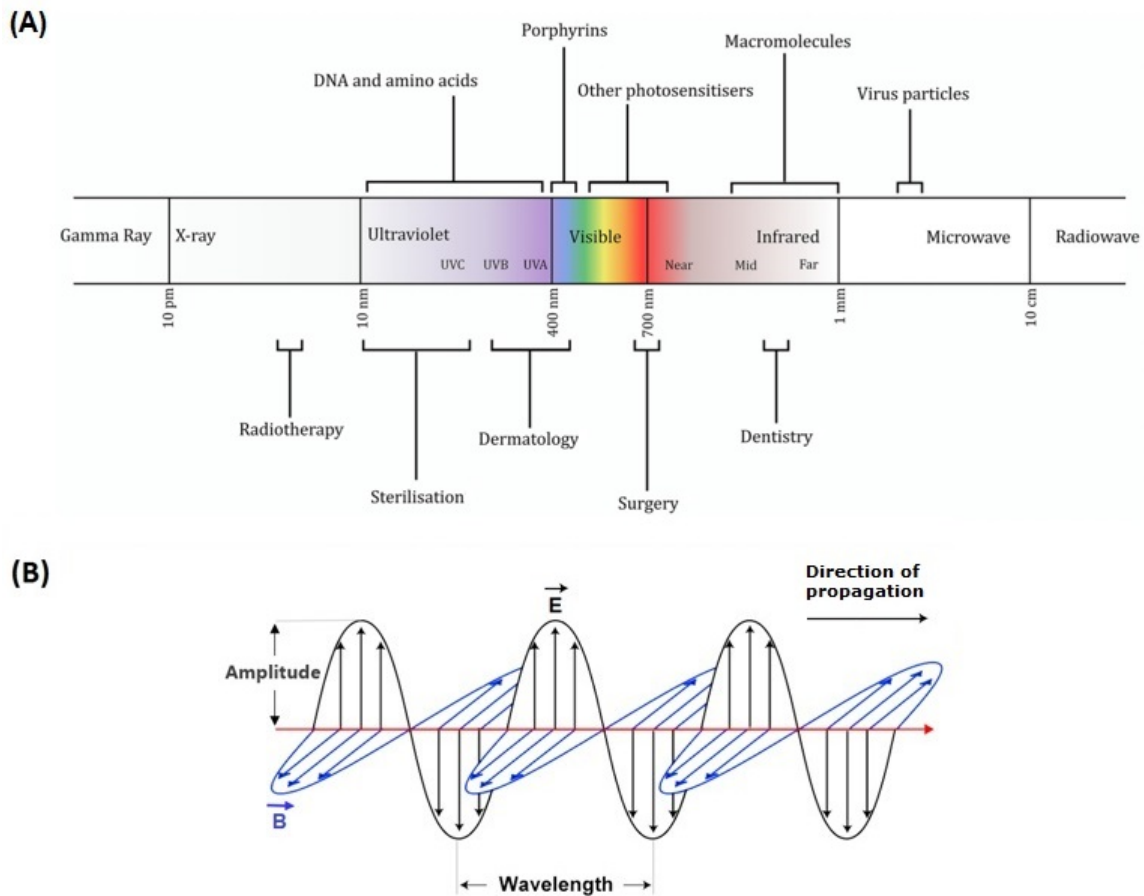
**Figure 1** – Clinical photodynamic therapy. DLI: Drug-light interval.  $PS^*$ : active photosensitizer.

Source: Adapted from XU *et al.*<sup>27</sup>

### 1.1.1 Light

An electromagnetic wave (EMW) is composed of electric and magnetic fields, oscillating perpendicular to one another. Its fundamental properties are frequency ( $\nu$ ), wavelength ( $\lambda$ ) and amplitude (A). Within electromagnetic spectrum, the range of light applied in phototherapy or PDT is composed by near ultraviolet (UVC, 100-280 nm; UVB, 280-315 nm; and UVA, 315-400 nm), visible (VIS, 400-780 nm); and infrared (IR, 780 nm-2000  $\mu$ m) spectra, which are non-ionizing radiation<sup>a</sup>. (Figure 2).

<sup>a</sup> Non-ionizing radiations are classified as near ultraviolet, visible, infrared, microwaves and radio waves, which carries enough energy to excite molecules. Whereas, ionizing radiations, such as Gamma rays, X-rays, and extreme ultraviolet, carries sufficient energy to ionize molecules.



**Figure 2** – (A) Electromagnetic spectrum with classification of wavebands for current applications. (B) Schematic representation of an EMW and its properties. E: Amplitude of electric field and B: Amplitude of magnetic field.

Source: GWYNNE; GALLAGHER<sup>28</sup>

The **light speed** in vacuum is approximately  $3.10^8$  m/s, which is a fundamental constant called *light velocity in vacuum* and symbolized by the letter  $c$ . White light is made up of different frequencies (colors) which travel at the same speed in vacuum, but not in other media. Light speed can be calculated by the following equation

$$v = \lambda\nu = c/n, \quad (1.1)$$

where  $n$  is the refraction index of the media for a specific light frequency,  $\lambda$  is the light wavelength and  $\nu$  is the light frequency.  $n = 1$  at vacuum and  $n > 1$  at nonvacuum media. In fact, at nonvacuum media, the light velocity and wavelength decreases, while the light frequency remains constant.

Light has a **dual nature**, it can behave like a wave moving through space (Wave theory established by Huygens), or it can behave like a particle, carrier of a discrete amount of energy known as a *photon* (Corpuscular theory established by Einstein). A light beam is modeled as a stream of photons, which have no mass and no charge, but each carrying a well-defined energy that depends of the light wavelength and can be calculated



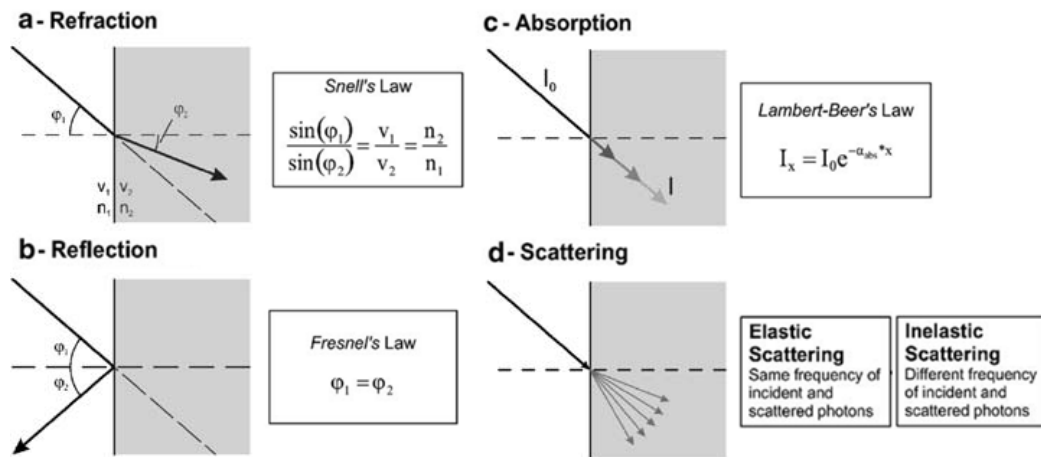
by

$$E = h\nu = hc/\lambda, \quad (1.2)$$

where  $h$  is the Planck's constant,  $\lambda$  is the light wavelength and  $\nu$  is the light frequency, both in meters. When a photon is emitted by the transitions of a molecules from an excited state (high energy) to its ground state (minimum energy), this photon can interact with other discrete particles (e.g., electrons, atoms, and molecules) which can get activated by absorption of the photon energy.

### 1.1.1.1 Interaction of light with biological tissue

When light is irradiated on biological tissue, the incident light intensity is gradually attenuated as its propagation through tissue due to reflection, refraction, absorption and scattering phenomena, which depend on the intrinsic molecules to each biological tissue (Figure 3).<sup>29</sup>



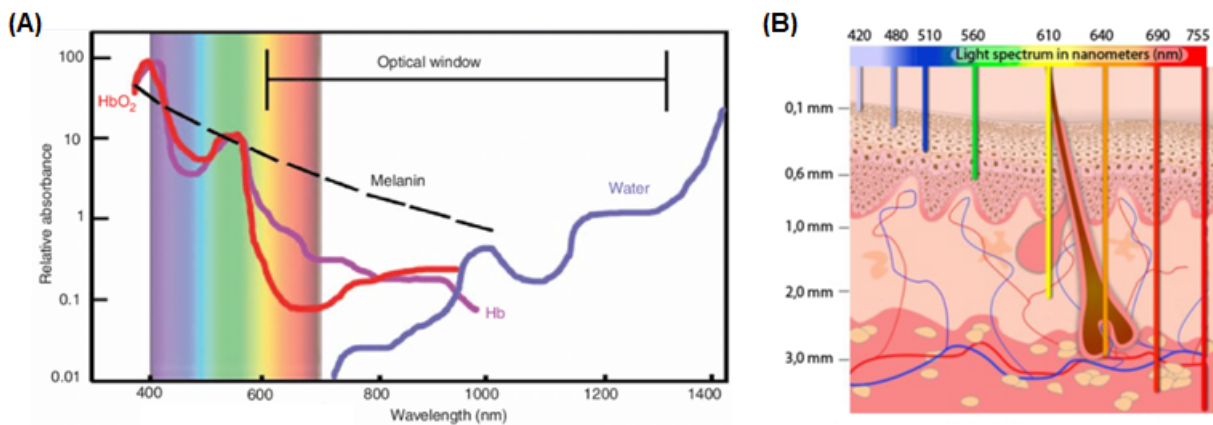
**Figure 3** – Light interaction with a biological tissue: (a) light refraction according Snell's Law, where  $v_1, n_1$  and  $v_2, n_2$  are the light speed and the refraction index of the surrounding media and tissue, respectively; (b) light reflection on the surface of a tissue according Fresnel's Law, where  $\phi_1$  and  $\phi_2$  are the incident and reflection angle respectively; (c) absorption phenomena according to Lambert-Beer's law, where  $I_0$  is the incident light intensity,  $I_x$  is the light intensity after light propagation at a depth  $x$  in the tissue, and  $\phi_{abs}$  is the tissue absorbance coefficient; (d) scattering phenomena.

Source: Adapted from PLAETZER *et al.*<sup>30</sup>

On the interface between two media such us air-tissue, a partial **reflection** of light can occur, losing part of the light out of the tissue in accordance with the Fresnel's law; while the remaining part penetrates the tissue (transmitted light) with a deviation in its incident angle according the Snell's law. This phenomena is called **refraction** and occurs because of the different refractive index of such a media. Both processes can be minimized by applying the light beam perpendicular to the surface between two media.<sup>30</sup>

Fresnel and Snell's law are applicable only to homogeneous media with flat interface (i.e. healthy eye cornea, lens and vitreous body). For the major types of tissues, optically inhomogeneous with rough interfaces, light reflection and transmission will be influenced by multiple scattering and absorption processes.<sup>31</sup> **Scattering** together with refraction cause a directionality change of the light beam, resulting in diffusion of light in adjacent tissues and loss of light intensity. There are two types of scattering, elastic or inelastic. Unlike elastic scattering which is categorized in both Rayleigh and Mie scattering<sup>b</sup>, inelastic scattering does not seem to play an important role in tissues. The light penetration depth is longer in Mie scattering media than in Rayleigh scattering media. **Absorption** is other relevant optical property that reduces the incident light intensity according Lambert–Beer's law, and the light penetration depth.<sup>30,33</sup>

**Light penetration depth** is widely related with chromophores<sup>c</sup>, which absorb certain wavelength, limiting the light penetration in tissue. The most important endogenous chromophores are water, oxyhemoglobin ( $HbO_2$ ) and deoxyhemoglobin, melanin and cytochromes.<sup>2</sup> The absorption spectra of tissue chromophores in figure 4-A, shows that blue light is highly absorbed by the superficial layers of the epidermis; green and yellow light is absorbed by melanin<sup>d</sup>, hemoglobin(Hb) and oxyhemoglobin; red light is basically absorbed by melanin; and infrared light is absorbed by water.<sup>35</sup>



**Figure 4** – (A) Optical window for PDT in tissue defined by the absorption spectra of tissue chromophores. (B) Light penetration depth in tissue according light wavelength. Light with a longer wavelength propagates through the tissue more deeply.

Source: LYONS *et al.*<sup>36</sup>

<sup>b</sup> Rayleigh scattering occurs in all directions when the particle size is much smaller than the light wavelength. Mie scattering corresponds to when the particle size is comparable to the light wavelength.<sup>32</sup>

<sup>c</sup> Chromophores is a part of the molecule that absorbs certain light wavelengths, and reflects the remaining wavelength conferring color on the material. Endogenous chromophores are natural absorption centers at normal biological tissue, while exogenous chromophores are introduced outside into the tissue (e.g. vital dyes and photosensitizers).<sup>34</sup>

<sup>d</sup> Melanin is a group of natural pigments that determine the skin color.

In fact, shorter wavelengths scatter and are absorbed more in tissues, so the optical window for PDT is limited to the region between 600 and 1200 nm. This range is further reduced, since PS molecules excited by  $\lambda > 850$  nm have too low energy to produce singlet oxygen ( $^1O_2$ ) and initiate a photodynamic reaction efficiently.<sup>37</sup> No single light source is ideal for all PDT indications, even with the same PS. While ultraviolet wavelength of light is applied to superficial lesions, red-shifted and near infra-red wavelengths of light are preferable for deeper lesions (Figure 4-B).<sup>28</sup>

### 1.1.2 Photosensitizers

Photosensitizers (PSs) are substances capable of absorbing light energy (exogenous chromophore compound), to later transfer part of the absorbed energy to adjacent molecules (e.g. oxygen molecule). As a result, reactive molecules are generated, ROS for instance. These reactive molecules not only induce target cells to death, but also lead PSs to structural and chemical modifications.<sup>2</sup>

**Photodegradation** or **photobleaching** is the chemical destruction of a PS molecule that results in the splitting of the PS into small fragments, which do not absorb in the visible spectral region, losing their function within PDT. **Photomodification**, also referred as photoproduct formation, are structural modification of side groups or the PS molecular skeleton. In experimental spectroscopy, photodegradation and photomodification can be identified by a lowering of absorbance or fluorescence emission. **Photorelocalization** can change the intracellular localization of a PS molecule, after light exposure. For some hydrophilic sensitizers<sup>e</sup>, photorelocalization from lysosomes to the nucleus occurs.<sup>30</sup> The theoretical considerations outlined above and the specific properties shown at Table 2, allow to define the ideal photosensitizing agent for PDT. As shown at table 1, PSs can be categorized by direct chemical structure and come from several broad families like: porphyrins, chlorophylls and dyes.<sup>1</sup>

**Table 1** – Several PS broad families like: porphyrins, chlorophylls and dyes.

<b>Porphyrin platform</b>	HpD (hematoporphyrin derivative)
	HpD-based
	BPD (benzoporphyrin derivative)
	ALA (5-aminolevulinic acid)
	Texaphyrins
<b>Chlorophyll platform</b>	Chlorins
	Purpurins
	Bacteriochlorins
<b>Dyes</b>	Phtalocyanine
	Napthalocyanine

Source: Adapted from ALLISON *et al.*<sup>1</sup>

<sup>e</sup> Sensitizers can be classified as hydrophilic, hydrophobic, or amphiphilic. Hydrophilic sensitizers are characterized by ionic substituents. They mostly enter cells by endocytosis and are founded in the endolysosomal vesicular system.<sup>38</sup>

**Table 2** – Properties of an ideal photosensitizer.<sup>1,2</sup>

<b>Selectivity</b>	Selectively accumulation in target tissues (e.g. neoplastic cells).
<b>Targetability</b>	Ability for passive or active transport within cells and have a well-defined subcellular target (e.g. mitochondria), since the mechanisms of cell death depend on the place of PS accumulation inside the cell.
<b>Toxicity</b>	Low dark toxicity, non-toxic at therapeutic levels (as in the case of chemotherapeutic agents), with minimal morbidity for the individual. Further, PS metabolism should not create new toxic byproducts.
<b>Biochemical</b>	Solubility and stability in aqueous solutions with physiological PH, to allow circulation and accumulation in cells.
<b>Photophysical</b>	Present high absorption (molar extinction coefficient, $cm^{-1}M^{-1}$ ) within the regions of the magnetic spectrum that are part of the biological optical window in order to get a maximum light penetration in tissue.
<b>Photochemical</b>	High singlet oxygen quantum yield for high photodynamic efficiency but should also be fluorescent to facilitate monitoring its biodistribution by point spectroscopy or imaging.
<b>Elimination</b>	PS must be metabolized quickly, minimizing possible side effects some degree of sunlight precautions are needed. Ideally, this would be measured in hours or days and not weeks or months.

Source: By the author.

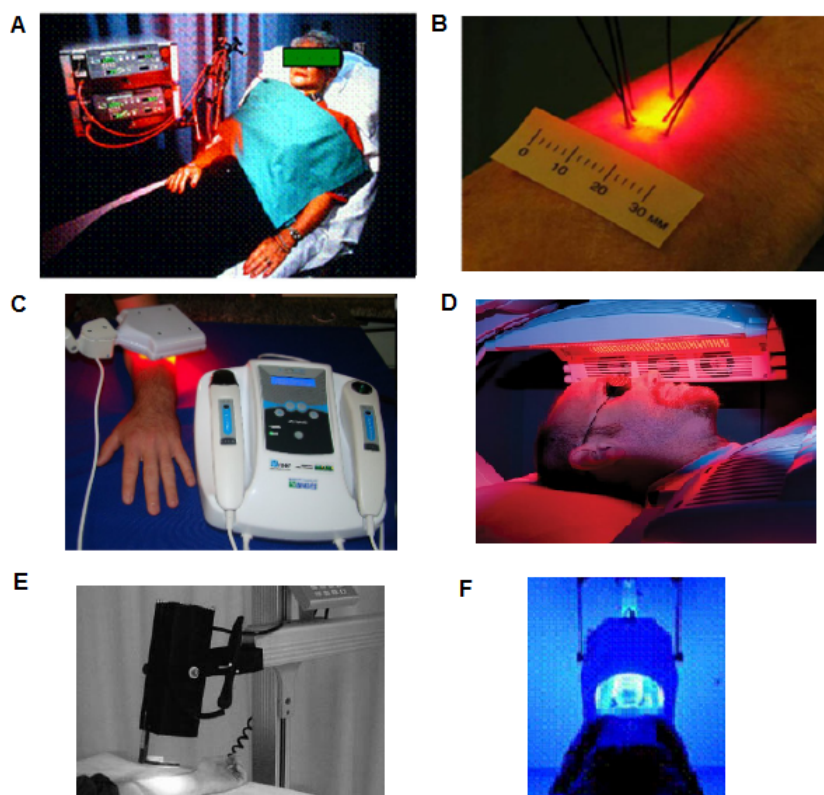
### 1.1.3 Light sources for PDT

Light source is a fundamental aspect in PDT. The basic requirements for PDT light sources are the PS activation spectrum, usually the longest wavelength peak, and to generate adequate power at this wavelength, deliverable to the target tissue ergonomically and with high efficiency. In addition, the sources must be reliable in the clinical environment and be cost-effective.<sup>39</sup> **Lamps, LEDs** (*Light Emitted Diode*) and **lasers** are the three main classes of clinical PDT light sources (Figure 5), which can be associated with accessories such as fibers, filters and lenses. The choice of light source for PDT can be determined by the type of lesion, PS, tumor location, and light dose delivered. The optimal combinations of PSs, light sources, and treatment parameters is crucial for successful PDT.<sup>2</sup>

### 1.1.4 Photophysics and photochemistry process in PDT

The PDT process initiate with the PS administration and accumulation in target cells during a certain period of time (DLI, *drug-light interval*). After DLI, tissue is illuminated with a wavelength corresponding to the PS absorption band, thus, light reaches target cells and activates the PS molecules accumulated within them.<sup>2</sup> Finally, during PS decay process, ROS are generated, leading to the tumor cells death.

Photophysics and photochemistry processes, that happen after light irradiation, are better detailed by the adapted Jablonsky diagram shown in Figure 6. The ground state of the most PS molecules is characterized by two electrons with opposite spins, a total spin of  $S=0$  and a spin multiplicity of 1, called the singlet state  $S_0$ . After the PS molecule in its ground singlet state ( $^1PS$ ) absorb a light quantum, one of the electrons goes to an

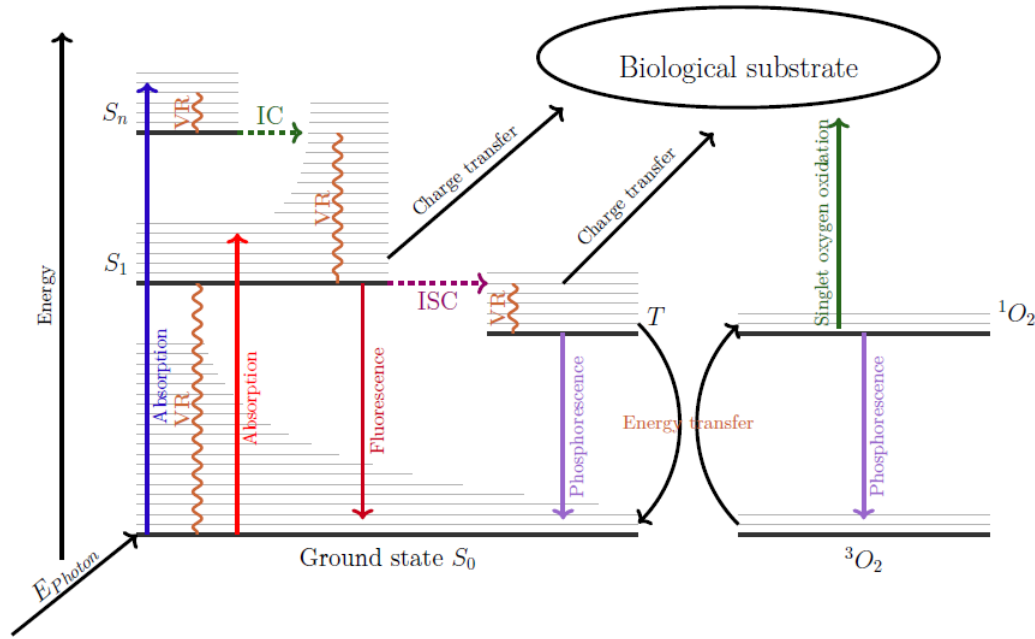


**Figure 5** – Examples of light sources for clinical PDT. (A) Diode lasers with fiber-optic light delivery applied by (B) interstitial irradiation. (C) PDT treatment using the large area probe of a LED-based device (Lince, Brazil). (D) PDT device based on narrow LED strips. (E) Tungsten filament lamp and (F) Fluorescent lamps in a U form used for ALA-PpIX skin treatments.

Source: WILSON; PATTERSON<sup>39</sup>; GRECCO *et al.*<sup>40</sup>

orbital of higher-energy, i.e.  $^1PS$  goes to an excited singlet state  $S_x$ , getting activated. The active PS ( $^1PS^*$ ) has a short lifetime and is very unstable, so  $^1PS^*$  loses excess energy and returns to  $S_0$  after a short period of time. This decay process of  $^1PS^*$  can occur through different reactions shown in Table 3. The electron at an excited singlet state  $S_x$  decays to the lowest vibrational level of  $S_x$  by a **vibrational relaxation** (VR) dissipating energy to the medium as heat. After that, the electron can undergo an **internal conversion** (IC) process to decay until a lower-energy state  $S_{x-1}$ . In this state, PS molecule undergo a new VR to the lowest vibrational level of  $S_{x-1}$ . Repeating these processes, the molecule follows to the energetically lowest PS excited state  $S_1$ . In this state,  $^1PS^*$  can return to  $S_0$  emitting the excess energy as **fluorescence**<sup>f</sup> or heat.<sup>42</sup> Alternatively,  $^1PS^*$  may undergo an **intersystem crossing** (ISC), to form a more stable triplet state  $T$  changing the spin orientation of one electron getting two electrons with equal spins, a total spin of

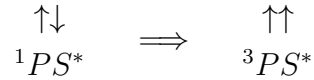
<sup>f</sup> Fluorescence is a form of luminescence (light emission of a molecule that has absorbed light or other electromagnetic radiation) whose typical lifetimes are of the order of nanoseconds.



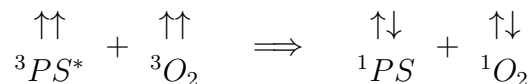
**Figure 6** – Diagram of energy levels and their respective transitions proposed by Alexander Jablonsky. IC: internal conversion, ISC: intersystem crossing, VR: vibrational relaxation,  $S_x$ : PS singlet states,  $T$ : PS triplet state.

Source: SANCHEZ *et al.*<sup>41</sup>

$S=1$  and a spin multiplicity of 3, as follows:



The PS in  $T$  ( ${}^3PS^*$ ) can interact with the biological substrate via charge transfer, forming superoxide anions ( $O_2^-$ ), hydrogen peroxide ( $H_2O_2$ ) and hydroxyl radicals ( $HO^-$ ), and returns to its fundamental state  $S_0$  emitting the excess energy as **phosphorescence**<sup>8</sup>. This process is referred as "**Type I mechanism**". Also  ${}^3PS^*$  can interact with the molecular triplet oxygen ( ${}^3O_2$ ) (ground state of oxygen) present in cells.  ${}^3PS^*$  transfers the excess energy to  ${}^3O_2$ , which will be transferred to an excited singlet state ( ${}^1O_2$ ), and returns to its fundamental state  $S_0$ .<sup>43</sup> This process is referred as "**Type II mechanism**", where the electronic spins are flipped in the following manner:



The singlet oxygen ( ${}^1O_2$ ) is highly cytotoxic and induce oxidative stress of the cell hosting the PS with consequent cell death via apoptosis and/or necrosis. Usually, Type I and Type II mechanisms take place at the same time.<sup>44</sup>

<sup>8</sup> Phosphorescence is a form of luminescence whose typical lifetimes may last up to a few milliseconds or seconds.

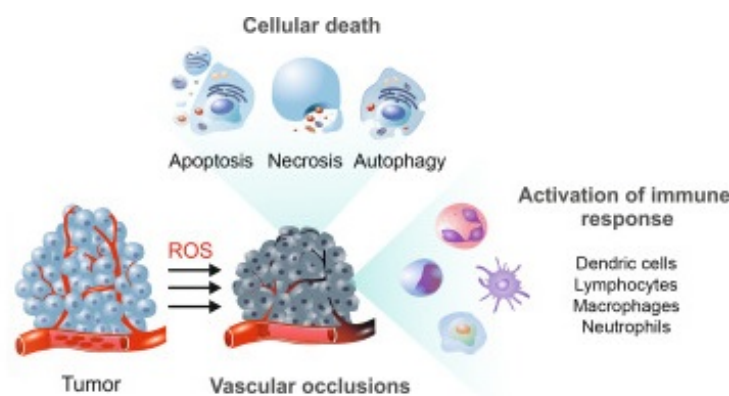
**Table 3** – Overview of kinetics of photosensitization during PDT. S: photosensitizer, RH: substrate with H-bond,  $S_x$  singlet-state molecule,  $T_x$  triplet-state molecule.

<i>Excitation</i>	
• Singlet state absorption	$S_0 + h\nu \Rightarrow S_1, S_2, \dots, S_x$
<i>Decays</i>	
• Internal conversion	$S_x, \dots, S_2 \Rightarrow S_1 + \text{heat}$
• Radiative singlet decay	$S_1 \Rightarrow S_0 + h\nu'$ (fluorescence)
• Nonradiative singlet decay	$S_1 \Rightarrow S_0 + \text{heat}$
• Intersystem crossing	$S_1 \Rightarrow T_1$
• Radiative triplet decay	$T_1 \Rightarrow S_0 + h\nu''$ (phosphorescence)
• Nonradiative triplet decay	$T_1 \Rightarrow S_0 + \text{heat}$
<i>Type I mechanisms</i>	
• Hydrogen transfer	$T_1 + RH \Rightarrow SH^\bullet + R^\bullet$
• Electron transfer	$T_1 + RH \Rightarrow S^{\bullet-} + RH^{\bullet+}$
• Formation of hydrogen dioxide	$SH^\bullet + {}^3O_2 \Rightarrow S_0 + HO_2$
• Formation of superoxide anion	$S^{\bullet-} + {}^3O_2 \Rightarrow S_0 + O_2^{\bullet-}$
<i>Type II mechanisms</i>	
• Intramolecular exchange	$T_1 + {}^3O_2 \Rightarrow T_0 + {}^1O_2$
• Cellular oxidation	${}^1O_2 + \text{cell} \Rightarrow \text{cell}_{ox}$

Source: Adapted from NIEMZ<sup>44</sup>

### 1.1.5 Mechanisms of PDT-mediated target cell death

The photodynamically effects that contribute either the reduction or disappearance of tumors can be **direct tumor cell death**; **tumor vascular damage** leading to tissue ischemia<sup>h</sup> following of tumor cells death; **immune modulation** or the combination of these processes (Figure 7).<sup>45</sup>

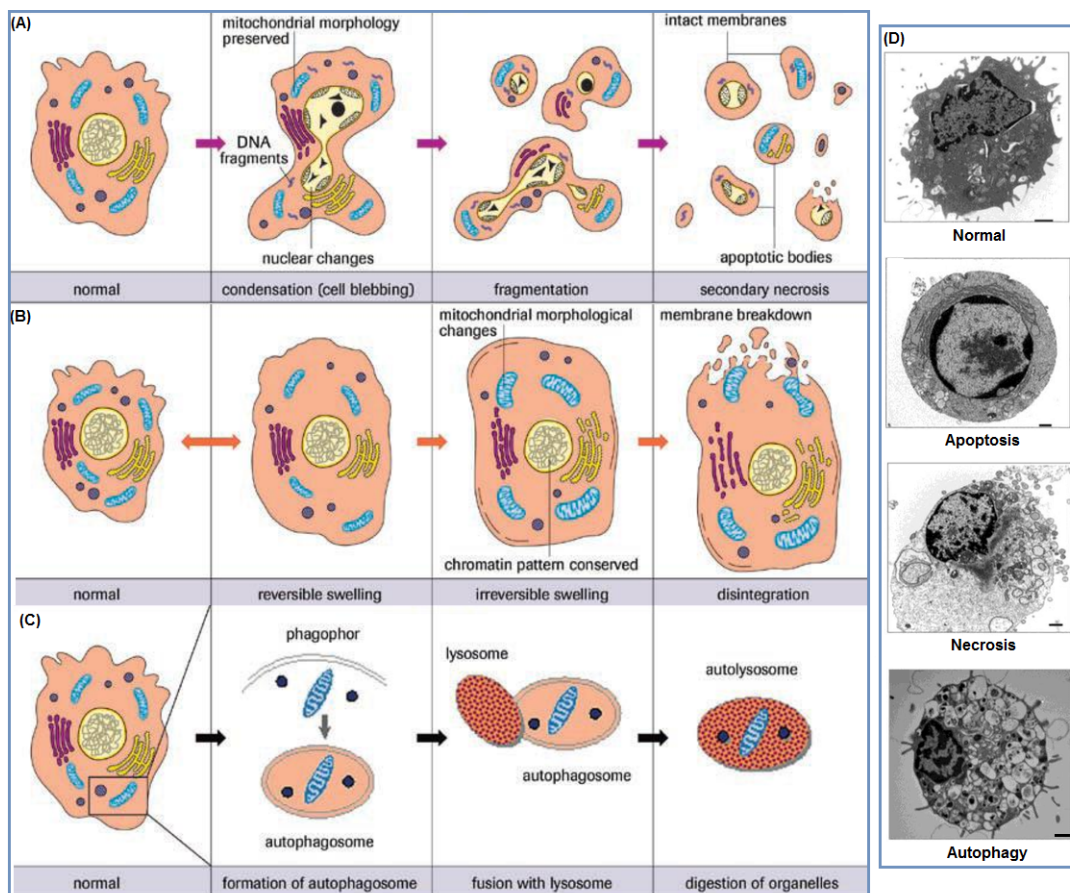


**Figure 7** – Schematic representation of PDT-induced effects on tumor cells, tumor tissue and immune system.

Source: By the author

<sup>h</sup> Ischemia is a restriction in blood supply to tissues, causing a shortage of oxygen as well as nutrients that are needed for cellular metabolism (to keep tissue alive). Ischemia is generally caused by problems with blood vessels (such as vasoconstriction, thrombosis or embolism).

At the molecular level, **direct tumor cell death** induced by PDT is generated by the irreversible photodamage at vital subcellular targets such as cell(plasma), mitochondria, lysosomes, Golgi apparatus and endoplasmic reticulum (ER) membranes. It is generally accepted that the primary site of photodamage resides at the same intracellular localization or within few nanometers from PS, since the photogenerated singlet oxygen ( $^1O_2$ ) has a very short life ( $<0.04 \mu s$ ) and limited diffusion in biological systems ( $<0.02 \mu m$ ). Most PSs do not accumulate in cell nuclei, so PDT has a much lower potential of causing DNA damage, mutations or carcinogenesis compared with therapies that involve ionizing radiation.<sup>46</sup> PDT-mediated direct tumor cell death can be elicited through three mechanisms: **apoptosis**, **autophagy** or **necrosis**.



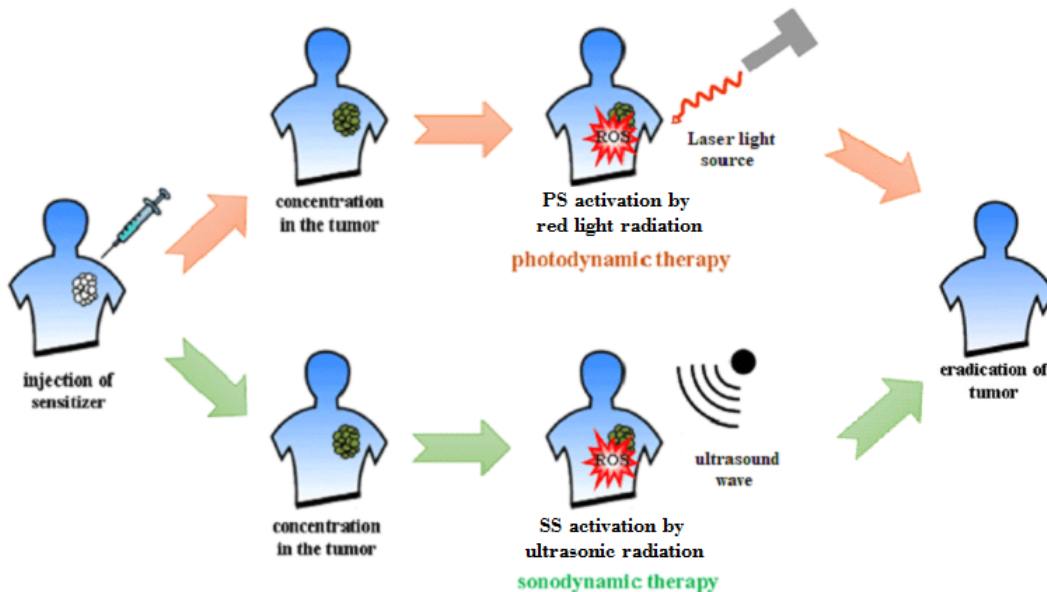
**Figure 8** – Three major cell death morphotypes induced by PDT: (A) apoptotic, (B) necrosis and (C) autophagy. (D) Morphological features of apoptotic, necrotic and autophagic cells. The scale bar represents 1  $\mu m$ .

Source: RODE *et al.*<sup>47</sup>; EDINGER<sup>48</sup>.



## 1.2 Sonodynamic therapy: Basic principles

SDT is a minimally invasive anticancer modality with a similar clinical protocol to PDT shown at Figure 9. SDT requires basically the presence of low-intensity ultrasound and a SS. These components are individually harmless, but together can lead to tumor cell death at deep-tissue.<sup>49</sup>



**Figure 9** – Schematic overview of both PDT and SDT against cancer. The PS or SS is administered systemically or locally into the tumor tissue, followed by light or ultrasound irradiation, respectively. The light-PS and ultrasound-SS interaction generates chemical and physical effects that lead to tumor cell eradication.

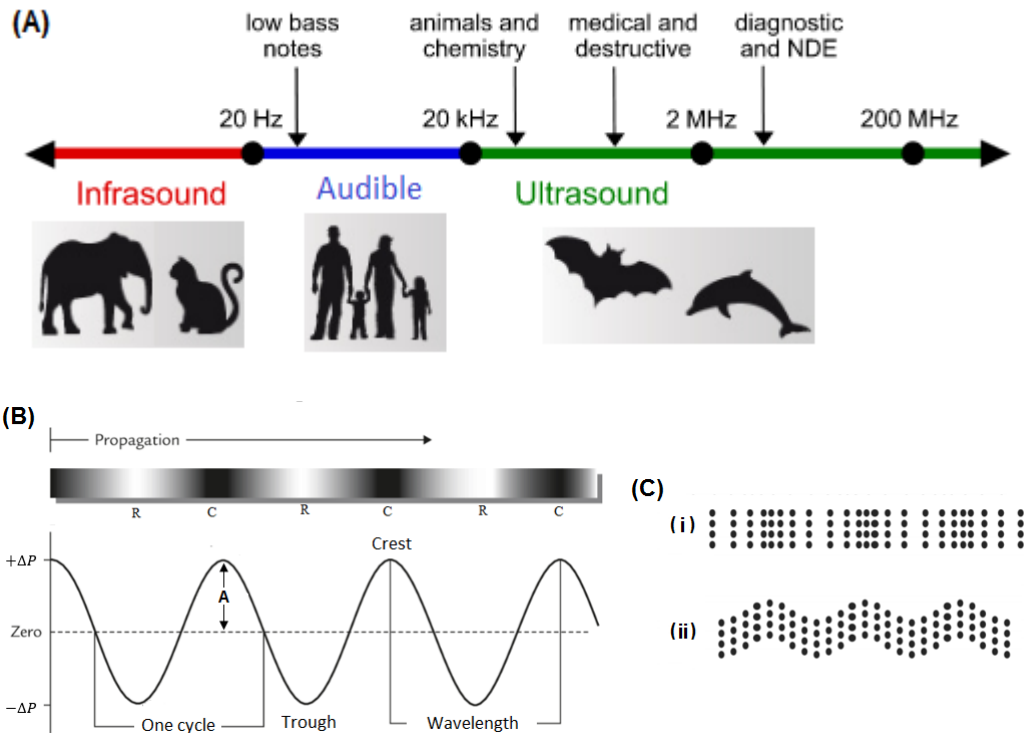
Source: Adapted from CANAVESE *et al.*<sup>50</sup>

### 1.2.1 Ultrasound

Ultrasound (US) is an acoustic wave, emanated from some animals (e.g. bats, whales) as well as electronic devices (e.g. transducers), with frequency higher than 20 kHz which is outside the human audible range (Figure 10-A). US is transmitted via mechanical waves that alternately compress (Compression phase,  $+\Delta P$ )<sup>i</sup> and stretch (rarefaction phase,  $-\Delta P$ )<sup>j</sup> the molecular structure of the medium during its propagation.<sup>51</sup> These pressure fluctuations transmit the energy within the tissues and produce physiological effects.

<sup>i</sup> Period of high or positive pressure in which molecules of the medium compress resulting in high particle density.

<sup>j</sup> Period of low or negative pressure in which molecules of the medium expand resulting in low particle density.



**Figure 10** – (A) Acoustic wave range. (B) Schematic representation of an acoustic wave (sinusoidal waveform). C: Compression phase and R: Rarefaction phase. (C) Representations of (i) longitudinal and (ii) transverse or shear waves.

Source: By the author.

The properties that describe acoustic waves include **wavelength<sup>k</sup>** ( $\lambda$ ), **frequency<sup>l</sup>** ( $\nu$ ) and **amplitude<sup>m</sup>** ( $A$ ). The crests and troughs represent specific amplitudes of the wave that correspond to compression and rarefaction peak values (Figure 10-B).<sup>52</sup> According frequency and amplitude of ultrasonic waves, they are applied at medicine for diagnostic applications (2.5 to 15 MHz and a low amplitude) or therapeutic applications (0.75 to 3.3 MHz and a high amplitude).<sup>52</sup>

When an ultrasonic wave is propagated within material, the type of wave is classified such as **longitudinal** or **transverse wave** (Figure 10-C). At longitudinal wave, the molecule displacement occurs parallel to the direction of sound propagation. These waves are capable of traveling through gaseous, liquid and solid materials. At transverse or shear waves, the particle displacement occurs perpendicular to the direction of sound propagation. These waves pass through solid materials, not in fluids.<sup>53</sup> Ultrasound propagates in soft tissue as a longitudinal wave. When the longitudinal waves strike harder biological materials such as bone, they become transverse waves.

<sup>k</sup> Distance from one crest to the next, or from one trough to the next (i.e. one complete cycle)

<sup>l</sup> Number of cycles per second, expressed in Hertz (Hz)

<sup>m</sup> Intensity of the sound, does not depend on frequency or wavelength.

Unlike light, ultrasound is not an electromagnetic wave but a mechanical wave that transmits acoustic energy and require a physical medium by which to do it. Audible sound (e.g. human voice) can be transmitted in the air, however ultrasound's high frequency requires a medium denser than air to be transmitted, water for instance. In a uniform medium, ultrasonic waves travel with a constant **propagation speed**, calculated according the physical medium of propagation (Table 4 and 5).

**Table 4** – Propagation speed of ultrasonic waves according the physical medium where they are propagating through.  $\gamma$ : ratio of specific heats,  $P_0$ : ambient pressure,  $\rho$ : medium's density,  $B_T$ : isothermal bulk modulium,  $\sigma$ : Poisson's ratio, and Y: Young's modulus.

Medium	US wave type	US speed
Solid	Longitudinal wave	$\sqrt{\frac{Y(1-\sigma)}{\rho(1+\sigma)(1-2\sigma)}}$
	Shear waves	$\sqrt{\frac{Y}{2\rho(1+\sigma)}}$
Liquid	Longitudinal wave	$\sqrt{\frac{\gamma B_T}{\rho}}$
Gaseous	Longitudinal wave	$\sqrt{\frac{\gamma P_0}{\rho}}$

Source: By the author.

**Table 5** – Ultrasound propagation speed in Biological and Nonbiological Material. Ultrasound speed is greater in materials that are more rigid or less compressible.

Nonbiological material	US speed (m/s)	Biological material	US speed (m/s)
Acetone	1174	Fat	1475
Air	881	Brain	1560
Aluminum (rolled)	6420	Liver	1570
Brass	4700	Kidney	1560
Ethanol	1207	Spleen	1570
Glass (Pyrex)	5640	Blood	1570
Acrylic plastic	2680	Muscle	1580
Mercury	1450	Lens of eye	1620
Water (distilled), 25 °C	1498	Skull bone	8860
Water (distilled), 50 °C	1540	Soft tissue	1540

Source: By the author.

**Acoustic impedance** ( $Z$ ) is a measure of the resistance that a material offers to the passage of an ultrasound wave and is expressed in units of rayls ( $Kg/m^2s$ ). The acoustic impedance of the wave is defined as

$$Z = \pm \rho c, \quad (1.3)$$

where, + is for the positive-going wave and - is for the negative-going wave,  $\rho$  is the material's density and  $c$  is the ultrasound propagation velocity in the material. The greater

the difference in acoustic impedance between two materials, the stronger will be the echo (i.e. reflected wave) arising from their interface. For example, the acoustic impedance variation between the air and skin is so great, so, virtually all the ultrasound beam will be reflected.<sup>52</sup> To avoid this, an acoustic coupling agent<sup>n</sup>, is required to permit penetration of the ultrasound beam into the body.<sup>54</sup>

The **acoustic intensity** (I) expressed in  $W/m^2$ , is defined as the average rate of flow of energy through a unit area normal to the direction of ultrasound propagation.<sup>10</sup> To estimate the acoustic pressure ( $P_a$ ), the acoustic intensity (I) is often used, both are directly related as

$$I = P_a^2 / 2\rho_0 c, \quad (1.4)$$

where  $\rho_0$  is the density of a medium (fluid) and  $c$  is the speed of sound in the fluid.  $\rho_0$  represents the acoustic impedance of the medium. An increase in ultrasound intensity means an increase in the acoustic pressure.<sup>55</sup>

#### 1.2.1.1 Acoustic Cavitation

When distance between molecules of a fluid exceed the critical molecular distance necessary to hold the fluid intact, liquid will break down and voids will be created. This happen due to a sufficiently large negative pressure applied to the medium.<sup>51</sup> In this way, **microbubbles** (MBs)<sup>o</sup> are formed during ultrasound irradiation of fluids. At rarefaction phase, gas enters the bubble as fluid is pulled away causing the bubble to grow in size, while in the compression phase, the fluid compresses the bubble causing gas to be dispersed to form a smaller-sized bubble.<sup>12</sup> MBs existence has been extensively researched and confirmed, while the mechanism behind their creation and stabilization continue to be explored.<sup>56-58</sup> From the viewpoint of the bubble as a microreactor, there are **three zones** in the cavitation process: cavity interior, gas-liquid interface and the bulk medium around the bubble, shown at figure 11.

**Acoustic cavitation** is an ultrasonically induced phenomenon that involves the formation, growth, and collapse of MBs in response to the pressure pulses occurring within fluid.<sup>51</sup> The acoustic cavitation intensity is benefited in fluids with low vapor pressure ( $P_v$ ) and high viscosity ( $\mu$ ), surface tension ( $\sigma$ ) and density ( $\rho$ ), however, MBs are more readily formed in fluids with opposite characteristics (i.e. high  $P_v$ , low  $\mu$ ,  $\sigma$ , and  $\rho$ ).<sup>55</sup> According the MBs behavior, acoustic cavitation can be classified as **non inertial** and **inertial cavitation** (Figure 12).

<sup>n</sup> Compound that provides a chemical bond between two dissimilar materials, usually an inorganic and an organic (e.g. transducer head-tissue), facilitating the transmission of the ultrasound energy.

<sup>o</sup> MBs also called cavitation nuclei, are small gas microspheres, typically 1-8  $\mu\text{m}$  in diameter, filled with an inert gas. MBs can be present as small undissolved gas bubbles in biological media or exogenously administered.<sup>55</sup>

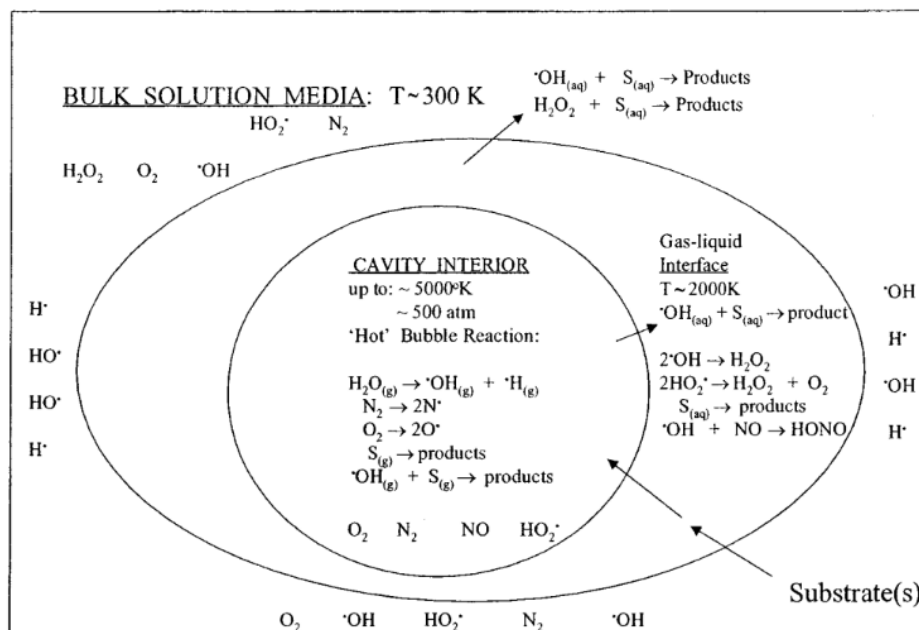
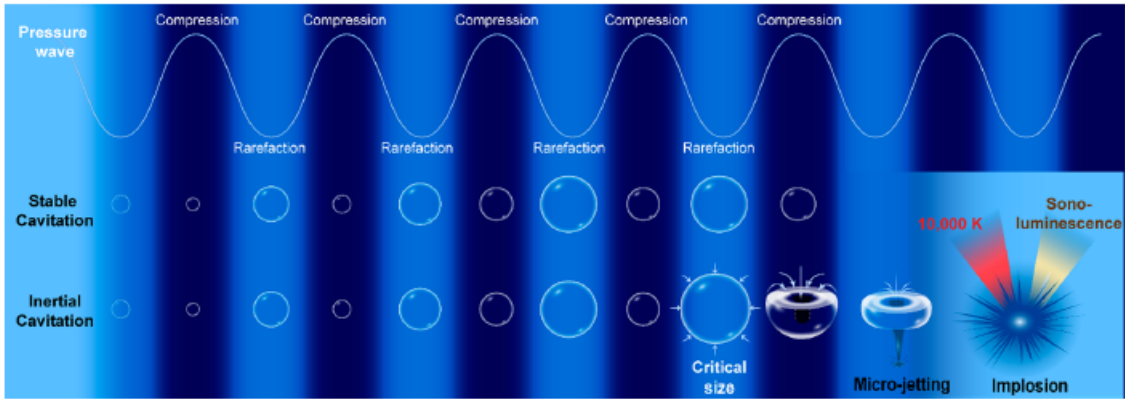


Figure 11 – Three reaction zones in the cavitation process.

Source: ADEWUYI<sup>55</sup>

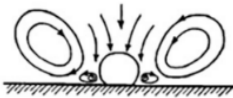

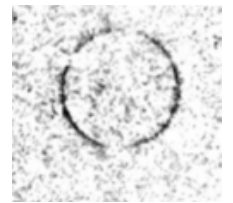
**Non inertial or stable cavitation** with a lifetime of many acoustic cycles, is kept for ultrasound intensities below the acoustic pressure threshold. Stable cavitation refers to the expand and contract of bubbles with stable oscillation around the same resting radius, and with long lifetime.<sup>10</sup> At increasing acoustic pressures, nonlinear bubble oscillations arise, creating *shear stress* and *microstreaming* in nearby environments, shown to produce stresses sufficient to disrupt cell membranes or even cause cell death through exposure of the protoplasm, depending on the degree of energy input.<sup>56</sup> **Inertial or transient cavitation** with a lifetime of one or a few acoustic cycles, emerge when ultrasound intensity beyond the acoustic pressure threshold is delivered within the fluid. Inertial cavitation involves the very rapid growth of MBs until reach a critical upper size, where the bubble can no longer absorb energy as efficiently from the sound waves. Without this energy, the cavity can no longer sustain their structure, so the liquid rushes in and the cavity implodes in its immediate vicinity (Figure 13).<sup>59</sup> The bubble implosion releases energy, giving rise to *several mechanical forces* (microstreaming, microjetting and shock waves) and locally *high levels of temperature* (4000-25000 K) and *pressure* (above 800 atm) with very short-lived, since the cavity itself is so small that the heat dissipates quickly to be registered. The high levels of temperature and pressure, may trigger sonochemical effects like *sonoluminescence* and *pyrolysis* of the water vapor inside the bubble, generating ROS.<sup>17,60,61</sup> At higher acoustic pressure, the cavitation bubble collapse will be more violent, eliciting greater sonochemical effects. While both inertial and non inertial cavitation are able to generate sonomechanical effects, only inertial cavitation can produce sonochemical effects (Table 6).<sup>56</sup>



**Figure 12** – Acoustic cavitation of microbubbles: Non inertial or stable cavitation and inertial or transient cavitation.

Source: CHOI *et al.*<sup>12</sup>

**Table 6** – Sonomechanical and sonochemical effects through acoustic cavitation.

Stable cavitation	Sonomechanical effects	Shear stress	At increasing acoustic pressures, nonlinear bubble oscillations arise, creating mechanical shearing in nearby environments, producing stresses sufficient to disrupt cell membranes. <sup>51</sup>
		Microstreaming <sup>10</sup> 	Strongly oscillating stable cavitation bubbles as well as collapsing transient bubbles induce fluid flow and promote radiation forces on particles. <sup>10</sup>
Inertial cavitation	Sonomechanical effects	Microjetting <sup>51</sup> 	Just before the bubble collapse near a solid surface, the liquid pressure on the bubble surface near a solid boundary becomes much lower than that on the other side of the bubble surface. As a result, a jet penetrates into a bubble and finally hits the solid surface. <sup>51</sup>
		Shock waves <sup>10</sup> 	When bubble reaches the sub-micron range in size, the trapped gas inside suddenly decelerates the wall motion. This results in the release of a strong pressure wave followed by shock waves, capable of mechanically disrupting nearby cell membranes. <sup>10</sup>
	Sonochemical effects	ROS generation	In a heated interior of a bubble, water vapor and oxygen, if present, are dissociated and oxidants such as $OH\cdot$ , $H\cdot$ , $HO_2$ , $H_2O_2$ are formed. <sup>62,63</sup>
		Sonoluminescence	Phenomenon that involves the transduction of sound into light. This light production has been confirmed by reports such as CRUM, L. <i>et. al.</i> <sup>64</sup> among others. <sup>14,65,66</sup>

Source: MASON *et al.*<sup>51</sup>; YASUI<sup>10</sup>.

Theoretical models have been proposed that approximate the dynamics of cavity implosion at various levels of accuracy.<sup>59</sup> Assuming adiabatic bubble collapse, the

**maximum temperature and pressure** within the collapsed cavitation bubbles were predicted by Noltingk and Nepprias<sup>67,68</sup> from approximate solutions of Rayleigh-Plesset equations<sup>P</sup> (RPEs):

$$T_{max} = T_0 \left[ \frac{P_a(n-1)}{P_v} \right], \quad (1.5)$$

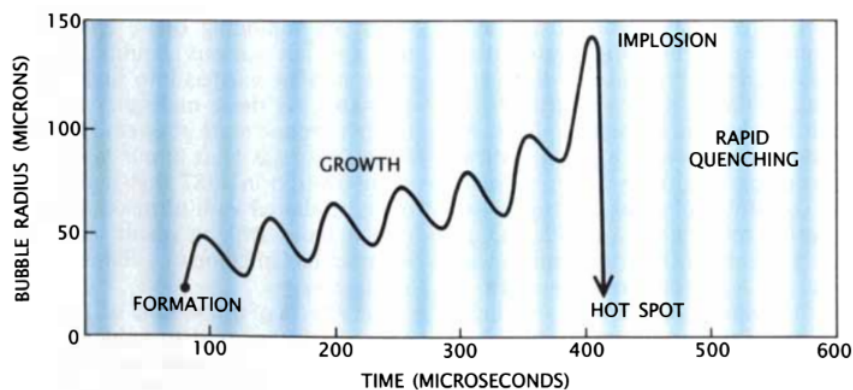
$$P_{max} = P_v \left[ \frac{P_a(n-1)}{P_v} \right]^{\frac{n}{n-1}}, \quad (1.6)$$

where  $T_0$  is the ambient temperature or temperature of bulk solution,  $P_v$  is the vapor pressure of the solution,  $P_a$  is the acoustic pressure in the bubble at the moment of transient collapse, and  $n$  is the polytropic index of the cavity medium. As seen in equations 1.5 and 1.6, higher temperatures and pressures are generated with monatomic gases with higher polytropic index.<sup>55</sup>

According to Raleigh, the main condition of effective action for ultrasonic cavitation is that the **time of cavity collapse** should be smaller than half the ultrasonics period, as shown in equation 1.7. For a bubble under constant external pressure (hydrostatic), the relation is given by

$$\tau \approx 0.915 R_{max} \left( \frac{\rho}{P_h} \right) < \frac{T}{2}, \quad (1.7)$$

where  $\tau$  is the time of cavitation bubble collapse,  $R_{max}$  is the maximum radius of cavitation bubble,  $T$  is the ultrasonic period,  $P_h$  is the hydrostatic pressure, and  $\rho$  is the density of the fluid. When the acoustic power  $P_a$  increases,  $R_{max}$  and  $\tau$  also increase. Frequency has significant effect on the cavitation process. At lower frequency, ultrasound induces greater  $R_{max}$ , leading to more violent cavitation with higher localized temperatures and pressures.<sup>55</sup>

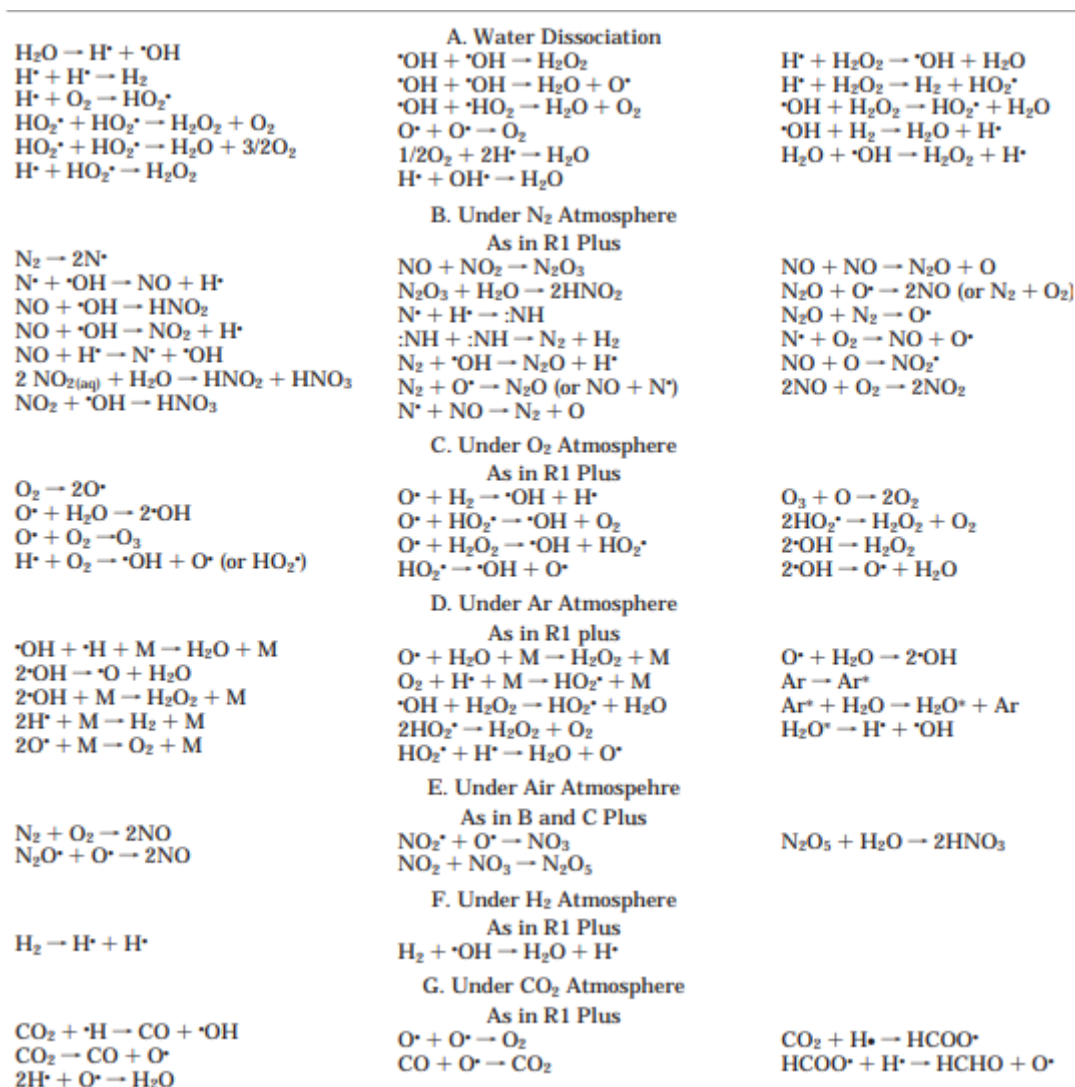


**Figure 13** – Bubble growth and implosion in a sonicated liquid, is the physical phenomenon responsible for sonochemical effects during inertial cavitation. Dark color regions:  $+\Delta P$ , Light color regions:  $-\Delta P$ .

Source: SUSLICK<sup>59</sup>

<sup>P</sup> Equations describing the oscillation of an acoustically driven bubble

One indicator of cavitation activity within a sonicated sample is the occurrence of **sonochemical reactions** shown at figure 14. These reactions are thought to be indicative of inertial cavitation.<sup>69</sup>



**Figure 14** – Some of the sonochemical reactions identified in the cavitation events

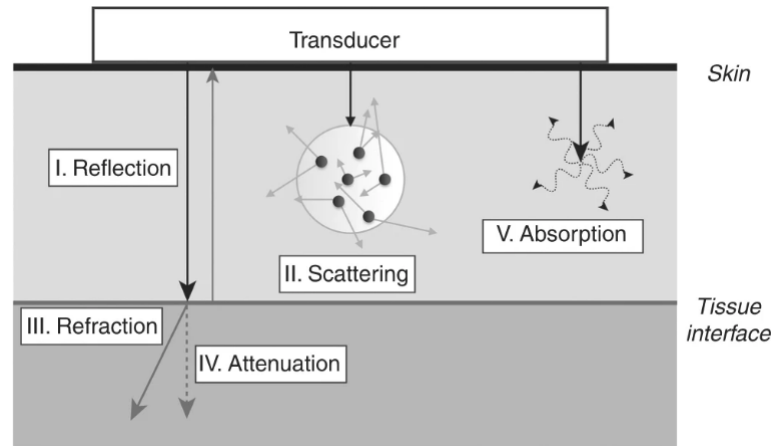
Source: ADEWUYI<sup>55</sup>

### 1.2.1.2 Interaction of ultrasound with biological tissue

When the ultrasound beam strikes an acoustical interface<sup>9</sup> such as different tissue layers, its course is influenced by the degree of change in density at the junction between both tissues, leading the ultrasonic wave to suffer **reflection** and **refraction** phenomena. Also, the ultrasound beam can suffer **scattering** and **absorption** phenomena along its propagation due the internal friction intrinsic to any medium in which it's propagating. On the acoustical interface, a partial *reflection* can occurs when part of the incident

<sup>9</sup> Surface where two materials of different densities meet.





**Figure 15** – Ultrasound-tissue interactions.

Source: OTTO<sup>70</sup>

ultrasonic energy reverses its direction out of the tissue. An echo is an example of reflection. The law of reflection states that the reflection angle equals the incidence angle.<sup>71</sup> The musculotendinous junction, intermuscular and soft tissue-bone interfaces are highly reflective interfaces (Table 7). *Refraction* is the bending of an ultrasound wave as a result of its speed change when enters a medium of different density. When US leaves a dense layer and enters a less dense layer, its speed increases. US tends to refract as it passes through joint spaces, potentially creating a standing<sup>r</sup> wave. *Scattering* consists of the deviation of the direction of ultrasonic wave propagation. US is scattered by the many cell and tissue elements that are smaller than the wavelength. The *absorption* phenomenon occurs by the tissue collecting the wave's energy and changing it into kinetic energy and then possibly into heat. The absorption of the US energy has a directly relation with the US frequency, but also depends on the protein content of the tissues (especially collagen). Protein-rich tissues such as muscles, tendon, and ligaments tend to absorb US energy.

**Table 7** – Percent reflection of ultrasonic energy at various interfaces.

Interface	Energy reflected (%)
Water-soft tissue	0.2
Soft tissue-Fat	1
Soft tissue-Bone	15-40
Soft tissue-Air	99.9

Source: STARKEY<sup>72</sup>

Each time ultrasound wave suffer these physical phenomena along its propagation through different tissue interfaces, the ultrasonic energy decrease, which is called **attenuation**.<sup>53</sup> The energy lost from an ultrasound beam in traveling the unit distance

<sup>r</sup> A single-frequency wave formed by the collision of two waves of equal frequency and speed traveling in opposite directions. The energy cannot be transmitted by a standing wave, so it's focused in a confined area.

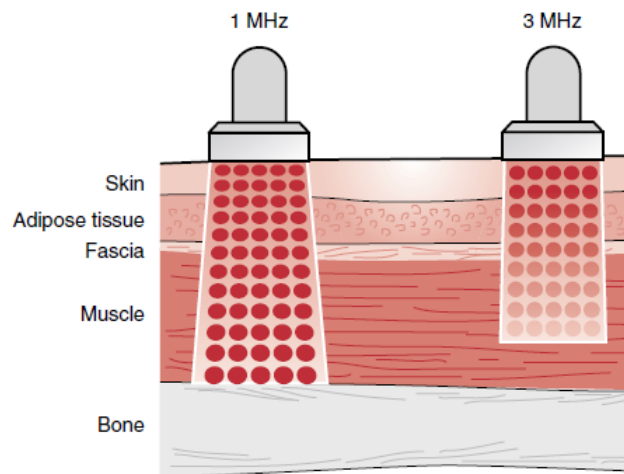
of  $dI/dx$  is given by

$$\frac{dI}{dx} = \alpha x \quad (1.8)$$

$$I(x) = I_0 e^{\alpha x} \quad (1.9)$$

where  $\alpha$  is the intensity attenuation coefficient (measured in dB/MHz.cm),  $I_0$  is the initial intensity of acoustic wave at the point of origin  $x=0$  and  $I_x$  is the reduced intensity at a distance  $x$  from the origin.

The **ultrasound penetration depth** within a biological tissue is affected by US attenuation of such tissue, having an inverse relation with the US frequency. For diagnostic applications in deep body parts, such as abdominal, obstetrical and gynecological ultrasound, and in echocardiography, the frequency range is generally between 2.5 and 7.5 MHz. For superficial body parts, such as the thyroid and the eye, and peripheral vascular applications, higher ultrasonic frequencies in the range of 7.5–15 MHz can be used.<sup>52,54</sup>



**Figure 16** – Ultrasound penetration depth according to ultrasound frequency. The lower the output frequency is, the deeper will be the penetration into the tissues.

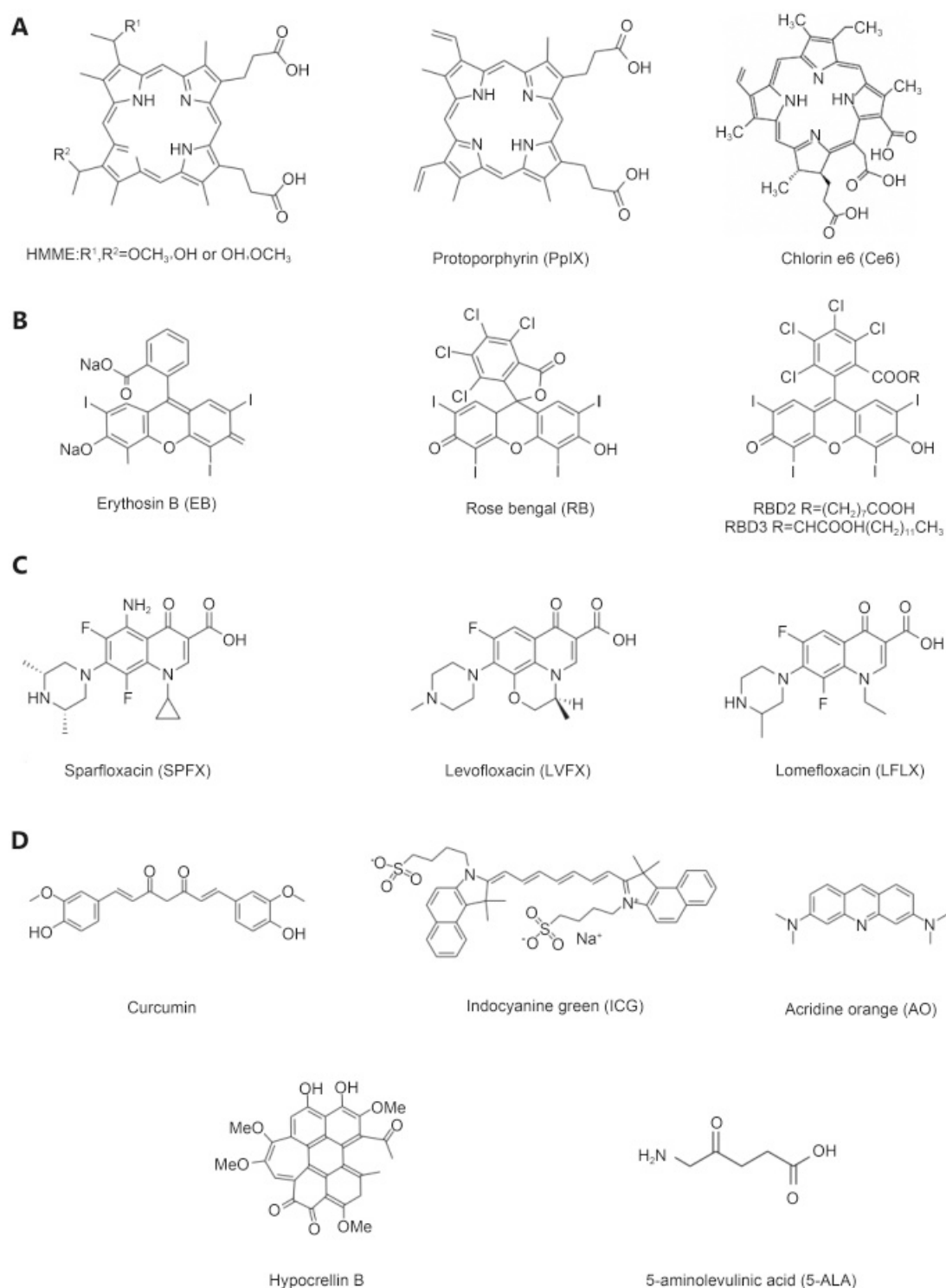
Source: STARKEY<sup>72</sup>

### 1.2.2 Sonosensitizers

Sonosensitizer (SS) is an acoustically susceptible molecule that is activated by deep-tissue-penetrating low intensity ultrasound. In 1989, Yumita *et al.*<sup>73</sup> found several hematoporphyrin derivatives (HPDs)<sup>s</sup> used in PDT also induced significant cell damage when they are activated with ultrasound. It has since been demonstrated that several newly-generated HPDs have potential to be used as SS in SDT.<sup>15,74</sup> The selection of a

<sup>s</sup> Hematoporphyrin derivative (HPDs) is a complex mixture of monomeric and aggregated porphyrins with photosensitizing activity.

suitable SS has become an important issue in current investigations of SDT.<sup>16,49,75</sup> The chemical structure of several kinds of sonosensitizers are shown in Figure 17.

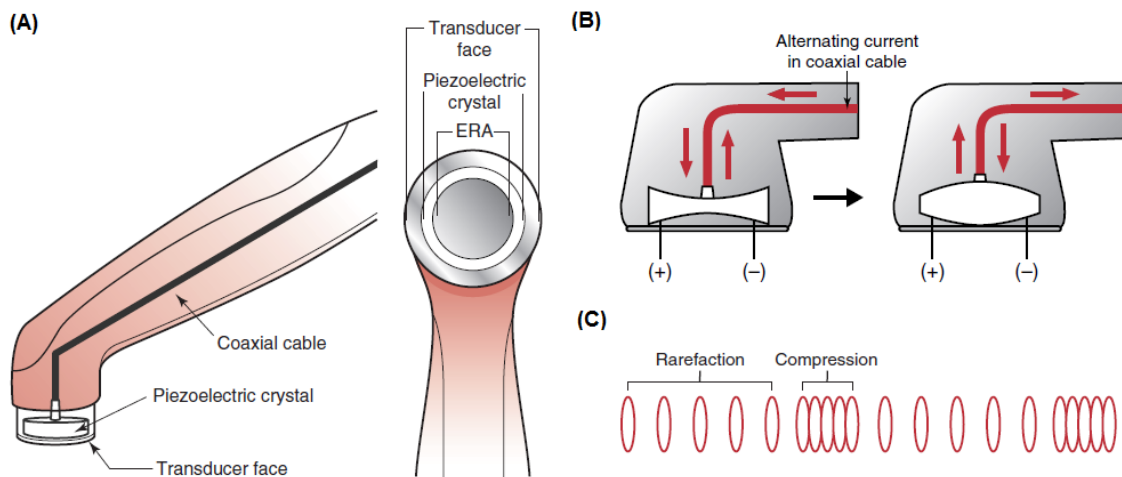


**Figure 17** – Chemical structures of (A) porphyrin-based sonosensitizers, (B) xanthene-based sonosensitizers, (C) non-steroidal anti-inflammatory drug-based sonosensitizers, and (D) other sonosensitizers.

Source: WAN *et al.*<sup>49</sup>

### 1.2.3 Ultrasound source for SDT

Therapeutic ultrasound is produced by a **transducer** via the *reverse piezoelectric effect*<sup>t</sup>. This effect occurs when an alternating current is passed through a *piezoelectric crystal*<sup>u</sup> housed in the transducer, originating the vibration of the piezoelectric crystal that finally results in ultrasonic sound waves that are passed along to the body transmitting acoustical energy (Figure 18).



**Figure 18** – (A) Lateral and face view of the transducer shows its components and the effective radiating area (ERA). The piezoelectric crystal produces the ultrasonic energy, but ERA is through which majority of the energy is emitted. (B) The reverse piezoelectric effect leads piezoelectric crystal expands and contracts, producing positive and negative electrical charges. (C) Rarefaction and compression of molecules by ultrasound.

Source: STARKEY<sup>72</sup>

Most medical ultrasound equipment operates in the ultrasonic frequency range of 1-15 MHz. Depending on the **output parameters** described in table 8, the ultrasound effects include increased rate of tissue repair and wound healing, increased blood flow and tissue extensibility, reduction of pain and muscle spasm, and changes in cell membrane permeability. Ultrasonic energy is also used to deliver medications to the subcutaneous tissues.<sup>54</sup> As shown in figure 19, a transducer can operate in **continuous or pulsed mode**. A continuous output (i.e. 100% duty cycle) induce a high increases in tissue temperature, since the heat produced by one cycle adds to the heat produced by the prior cycle, causing primarily thermal effects. On the other hand, a pulsed output (e.g. 10, 25 or 50% duty cycle) lead each pulse width, creates a brief increase in temperature, but the pulse interval

<sup>t</sup> The piezoelectric effect is the formation of electric dipoles by the application of pressure on a material. Inverse piezoelectric effect is the deformation of a material by the application of an electric field.

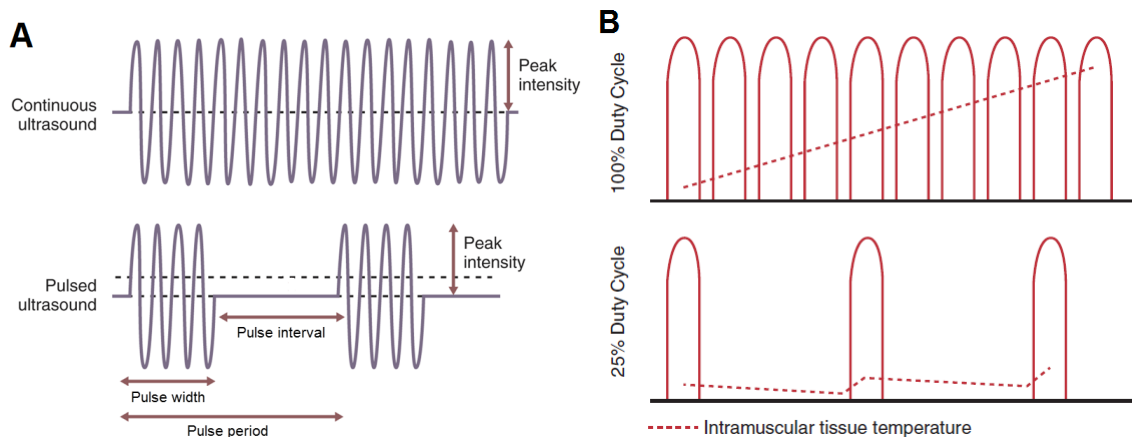
<sup>u</sup> Piezoelectric crystals are elastic bodies such as crystallized quartz ( $SiO_2$ ), barium titanate ( $BaTiO_3$ ) and zirconate titanate.

allows the heat to dissipate, producing primarily nonthermal effects. It's important to have on mind that pulsing the out-put reduces the temperature increase, but it does not entirely eliminate tissue heating.

**Table 8** – Ultrasound Output Parameters and Measures.

Parameter	Description
Intensity	The intensity describes the amount of power generated by unit, measured in $W/cm^2$ .
Frequency	The output frequency determines the effective depth of penetration. A 1 MHz output targets tissues up to 5 cm deep; 3 MHz has a penetrating depth of at least 2 cm. These depths are influenced by tissue geometry and their relative location to bone.
Effective radiating area (ERA)	The area of the transducer that produces ultrasonic waves. Measured in square centimeters ( $cm^2$ ). The actual ERA is usually significantly smaller than the contact area of the sound head. Larger ERAs produce a more focused beam than smaller ERAs
Duty cycle (DC)	The percentage of time that ultrasonic energy is being emitted from the sound head. A 100 % duty cycle indicates a constant ultrasound output and produces primarily thermal effects within the body. A low duty cycle produces non thermal effects. Heating effects increase as the duty cycle increases.
Beam nonuniformity ratio (BNR)	The BNR describes the consistency (uniformity) of the ultrasound output as a ratio between the spatial peak intensity (SPI) and the spatial average intensity (SAI). The lower the ratio, the more uniform the beam. A BNR greater than 8:1 is unsafe.
Treatment duration	The treatment duration is determined by the output intensity and the specific goals of the treatment.

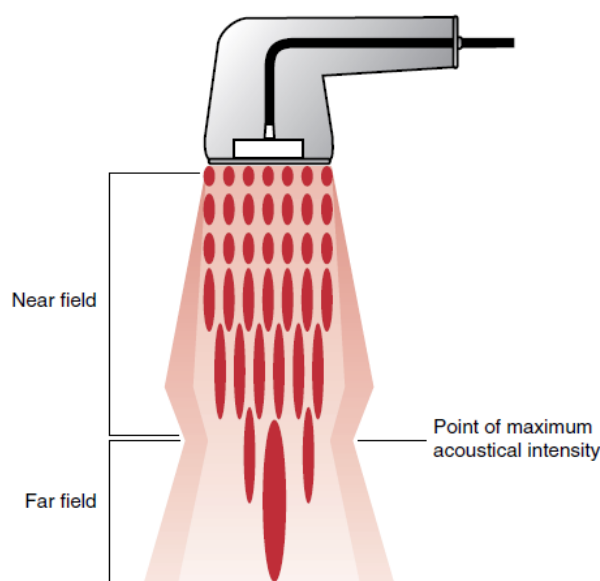
Source: Adapted from STARKEY<sup>72</sup>



**Figure 19** – (A) Continuous and pulsed mode. Pulse period is the sum of the pulse duration time (pulse width) plus the time between ultrasonic pulses (pulse interval). Pulse width is composed by a small number of cycles. (B) Relationship between ultrasound output mode and temperature. Over time, pulsed output still results in small increases in tissue temperature, but does not reach therapeutic ranges.

Source: Adapted from STARKEY<sup>72</sup>

Low-frequency acoustic waves, such as human voice (50-4 kHz), diverge in all directions, however the frequencies used in therapeutic ultrasound (0.75-3.3 MHz) produce relatively focused beams. The higher the frequency of the acoustic wave, the less the **acoustic beam** diverges. The near field or Fresnel zone shown at figure 20, is the portion of the ultrasound beam used for therapeutic purposes. The pressure variations occur because the transducer head acts as if it were formed by many smaller transducers, each producing its own ultrasound wave. The areas close to the transducer are individually distinguishable, while at far distances from the head the ultrasound beam is more unified.



**Figure 20** – The schematic representation of an ultrasound beam shows the irregular intensity of the near field and the spatial peak intensity in the far field.

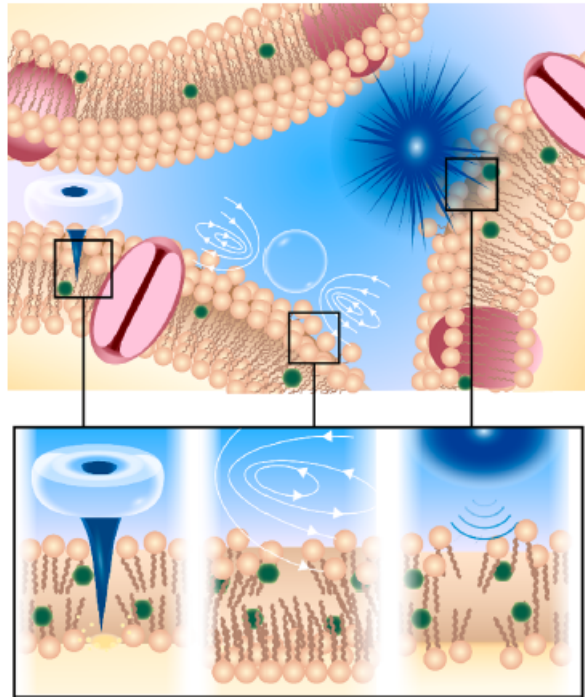
Source: STARKEY<sup>72</sup>

#### 1.2.4 Sonophysics and sonochemistry process in SDT

Several studies results, both in vitro and in vivo, suggest that SDT-mediate biological effects are elicited by both sonomechanical and sonochemical mechanisms.<sup>11</sup> So, despite SDT mechanism of action continues to be explored, it was proposed that interaction of sonosensitizers with cavitating bubbles in biological media is the driving force behind SDT.

The **sonomechanical SDT mechanisms** are based on the interaction of cavitation-mediate mechanical events with the SS-mediate destabilized cell membrane, eliciting hydrodynamic stress and cell damage (Figure 21). The hydrophobic porphyrin core is known to embed into the lipid region of cell membrane bilayers, creating not only preferential accumulation of the molecule, but also potential enhancement of mechanical stresses.<sup>76</sup> Thus, sonosensitizers may enact their synergistic SDT effects by lowering the pressure threshold needed for trigger cavitation mechanical events such us *microjetting*, *microstreaming*, and

*shock waves* (Table 6). In this way, cell membrane becomes more vulnerable to the inherent cavitation mechanical events already mentioned. These theorized porphyrin-membrane interactions is based on photosensitizer-membrane modeling performed for PDT.

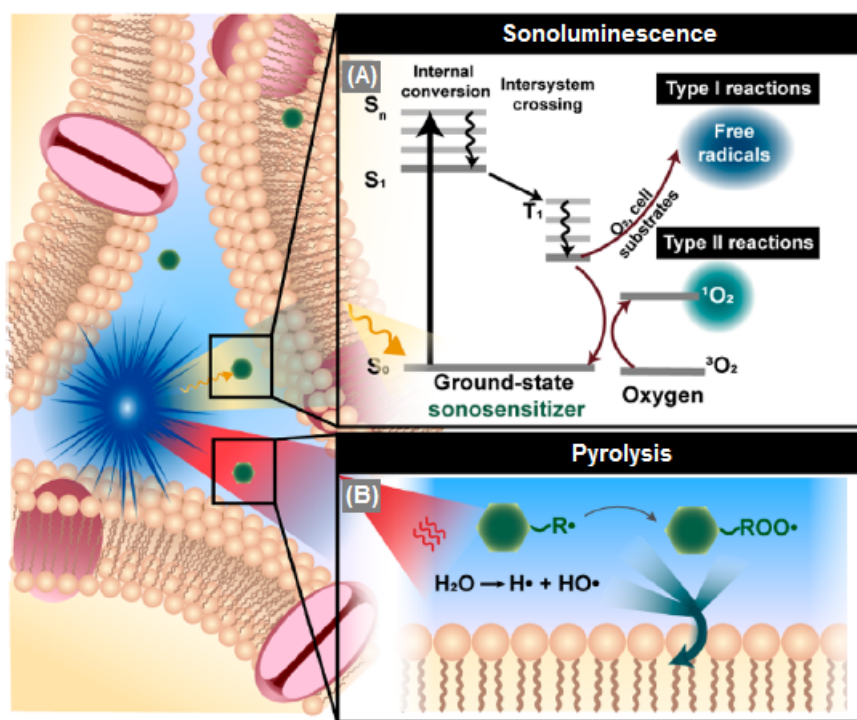


**Figure 21 – Sonomechanical SDT mechanisms.** They are based on the interaction of *microjetting*, *microstreaming*, and *shock waves* phenomena with the destabilized cell membrane.

Source: CHOI *et al.*<sup>12</sup>

The **sonochemical SDT mechanisms**, are based on the ROS generation through the interaction of sonosensitizers with inertial cavitation-mediate phenomena such as: sonoluminescence and pyrolysis (Figure 22). The *Sonoluminescence* is thought to excite photoactive sonosensitizers from the ground state to a short-lived excited singlet state, basically following a PDT-like mechanism shown in section 1.1.4, to finally generate ROS, both hydroxyl radicals and singlet molecular oxygen. Sonoluminescence can be observed as occurring after stimulation in the ultrasonic frequency range, from 20 kHz up to 3 MHz, and is influenced by acoustic pressure, frequency, liquid properties, temperature and specific gas content.<sup>19</sup> The sonosensitizer activation is made feasible through the emission of sonoluminescent light over a broad range encompassing the Soret band of many porphyrin sonosensitizers as demonstrated by Umemura *et al.*<sup>15</sup>. Sonoluminescence was recently observed by Giuntini *et al.*<sup>19</sup>, studying the ultrasound-mediated various metal-porphyrin complexes activation. Alternatively, *pyrolysis* of sonosensitizers may be the source of ROS generation following SDT. The high focal temperatures generated from inertial cavitation can cause the thermolysis of water, yielding free radicals that can interact with sonosensitizers to generate longer-lived cytotoxic peroxy radicals. Sonosensitizers may also

be directly decomposed into radical species in the vicinity of the sonochemical hotspot. The formation of these sensitizer-derived peroxy radicals was observed by Riesz *et al.*<sup>63</sup>.



**Figure 22 – Sonochemical SDT mechanisms.** Though inertial cavitation phenomenon is possible to trigger sonoluminescence and high levels of heat (4000-25,000 K), which interact with nearby sonosensitizers (shown in green) by (a) a PDT-like mechanism and (b) pyrolysis respectively. As a result of this interaction reactive oxygen species are generated, inducing cellular death.

Source: CHOI *et al.*<sup>12</sup>

### 1.2.5 Mechanism of SDT-mediated target cell death

Several *in vitro* studies show the type of SDT-induced cellular death. Yumita *et al.* suggested that the combination of ultrasound and NPe6 sonochemically induces apoptosis as well as necrosis in HL-60 cells. In their study, HL-60 cells exposed to ultrasound in the presence of a photochemically active chlorine (NPe6), showed membrane blebbing and cell shrinkage as well as DNA ladder formation, caspase-3 activation and a substantially enhanced nitroxide generation, however these events were not observed in cells exposed to either ultrasound or NPe6 alone at the same intensity and concentration, respectively.<sup>77</sup> Song *et al.* found that ALA-mediated SDT produced strong apoptotic effects on SAS cells, which were exposed to SDT with 10  $\mu\text{g}/\text{ml}$  ALA resulting in higher lipid peroxidation level and more cells losing their mitochondrial membrane potential than cells treated by ultrasound alone.<sup>78</sup> Li *et al.* found primarily that a Caspase-dependent apoptosis could be induced by PpIX-SDT in MDA-MB-231 cells, and the intracellular ROS is involved during

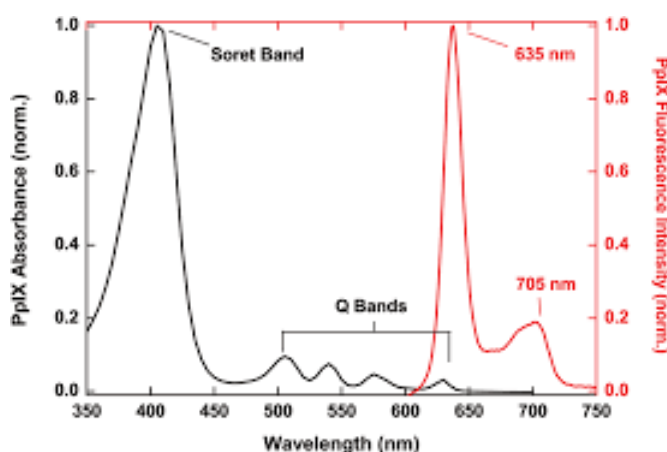


the apoptotic process. Besides, several distinct sonochemical effects were found after SDT treatment, including the decrease of cell viability, generation of intracellular ROS, the loss of mitochondrial membrane potential.<sup>79</sup>

*In vivo* experiments also were carried out in order to found biological sonodynamic effect. Wang *et al.* revealed that SDT with SF1 (sonoflora-1) did inhibit growth of mouse S-180 sarcoma and the inhibitory effect was sound intensity dependent. In this study, pathological slices showed coagulated necrosis or metamorphic tissue with inflammatory reaction in the tumor taken from 2 to 36 hours after SDT.<sup>80</sup> Y *et al.* investigated the anti-tumor efficiency of sonodynamic therapy on human tongue squamous carcinoma SAS cell line. Through the use of ROS scavenger, ALA-ultrasound induced SAS cell apoptosis by the generation of ROS. The process initially damaged mitochondria, activated pro-apoptotic factors Bax and cytochrome c, suppressed the anti-apoptotic factor Bcl-2, and activated caspase-3 to executed apoptosis through mitochondrial signaling pathway.<sup>81</sup>

### 1.3 Protoporphyrin IX as a sono-photosensitizing agent

Protoporphyrin IX (PpIX) is an organic compound, specifically a porphyrin, that plays an important role in living organisms as a precursor to other critical compounds like hemoglobin and chlorophyll. The PpIX is an endogenous fluorescent photosensitizer, present in hemoglobin, myoglobin and in most cytochromes. It absorbs throughout the visible and near-ultraviolet region. As shown in Figure 23, PpIX has five absorption bands in the visible spectrum: a large one around 400 nm called ‘Soret’ band and four smaller peaks called ‘Q-band’.

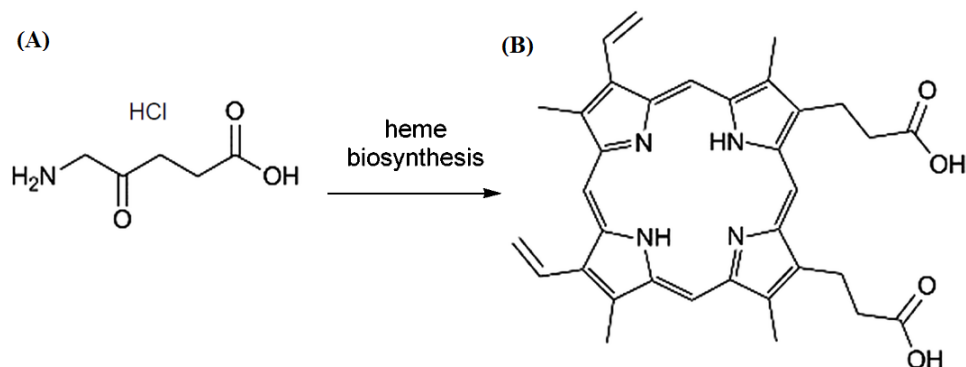


**Figure 23** – PpIX absorption and fluorescence spectrum, with a dominant peak at 407nm and 635 nm, respectively.

Source: VALENTINE *et al.*<sup>82</sup>

The physiological concentration of PpIX inside the body is controlled by its precursor 5-aminolevulinic acid (5-ALA), which can be administered and enzymatically

converted into PpIX via the heme biosynthesis pathway (Figure 24).<sup>83</sup> By supplying ALA to cells, it is possible to overcome the negative feedback mechanisms in the synthesis of haem and accumulate PpIX well above the physiological concentration.<sup>84</sup>



**Figure 24** – Chemical structures of (A) 5-ALA and (B) PpIX.

Source: BAGNATO *et al.*<sup>2</sup>

PpIX is one of the more photolabile photosensitizers used in PDT since it preferably accumulates in tumor cells instead of peripheral normal cells. PpIX has also been suggested as a good sonosensitizer, which makes it a convenient sensitizer for this work.<sup>1,75,79</sup> Besides, its precursor, 5-aminolevulinic acid (5-ALA), was used in previous works to mediate treatments in rat liver, and had been approved in Brazil for clinical use in PDT treatment.<sup>85,86</sup>

## 2 OBJECTIVES

### 2.1 General objective

Analyze the mechanisms and effects of the sono-photodynamic (SPD) action on Protoporphyrin IX (PpIX) solutions and PpIX-loaded rat healthy liver.

### 2.2 Specific objectives

#### 2.2.1 *in vitro* procedures

- Evaluate the effects of the SD action using solutions with different PpIX concentrations.
- Evaluate the effects of the PD, SD and SPD action applying different ultrasound and light intensities.
- Compare the effects of the PD, SD and combined action.

#### 2.2.2 *in vivo* procedures

- Develop a prototype capable of irradiating ultrasound and light simultaneously and individually.
- Evaluate the necrotic-healthy tissue transition in rat liver induced by the PD, SD and combined action.
- Compare the necrosis area in rat liver induced by the PD, SD and combined action.



### 3 MATERIALS AND METHODS

#### 3.1 *In vitro* experiments

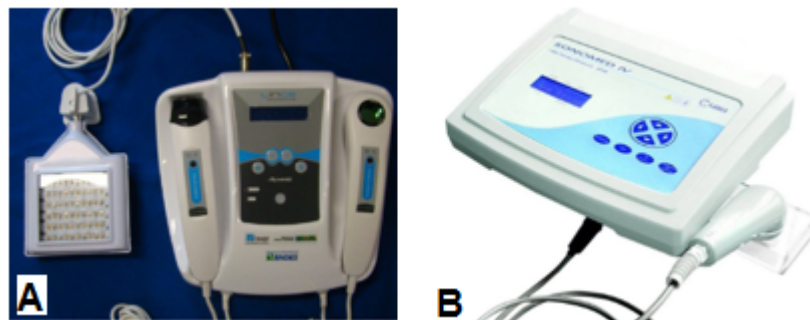
##### 3.1.1 Sono-photosensitizer

The sono-photosensitizer employed was Protoporphyrin IX (PpIX) (Sigma Aldrich, USA) with a purity  $\geq 95\%$ . The material was supplied as a powder and diluted in 100% Dimethyl Sulfoxide PA-ACS (DMSO) (Labsynth<sup>®</sup>, Brazil) to get a  $0.25 \text{ mg/mL}$  stock solution, which was stored in the dark at  $4 \text{ }^\circ\text{C}$  before experiments.

##### 3.1.2 Light and ultrasound source devices

*Light source device.* The apparatus used for light delivery was the photodynamic device LINCE (MMOptics Ltda., Brazil), which have two PDT treatment probes: the small and large probe area. For the experiments, it was applied the large probe area ( $8.0 \times 7.6 \text{ cm}$ ), composed by 60 LED arrays: 30 arrays emitting at  $630 \pm 10 \text{ nm}$  (red light range), and 30 arrays emitting at  $450 \pm 10 \text{ nm}$  (blue light range).<sup>40</sup> For the experiments, just the 30 LEDs emitting at red light range were lit.

*Ultrasound source device.* The apparatus used for US delivery was the therapeutic ultrasound SONOMED IV (CARCI, Brazil) with resonance frequency of 1 MHz and effective radiation area of  $3.5 \pm 0.7 \text{ cm}^2$ . For the simultaneously light and US irradiation, the transducer was placed in the petri dish and immersed in the PpIX solution, while the laser light source was placed under the petri dish irradiating the PpIX solution from bottom to top.



**Figure 25** – Light and US source devices: (A) LINCE and (B) SONOMED IV.

Source: By the author

The emitted irradiance by LINCE was measured with a spectroradiometer (calibrated USB 2000, Ocean Optics, USA). While the emitted US power by SONOMED IV was calibrated with an ultrasound power meter (Glutty Max, Brazil).

### 3.1.3 Analysis of the PpIX absorption spectrum

To study the effects on PpIX solution by light, ultrasound or the combined irradiation of both sources, it was measured the absorption spectrum of the PpIX solutions during irradiation. By means of the measured absorption spectrum, the spectroscopic changes and the PpIX degradation induced by irradiation of each excitation source were analyzed.

#### 3.1.3.1 PpIX degradation mediated by ultrasound and light irradiation.

It was proposed a first order mechanisms to describe the kinetics of the PpIX concentration in solutions exposed to ultrasound and light irradiation. In this way, the PpIX concentration ( $[PpIX]$ ) varies over time according the sum of the rates of all the processes that participate in the PpIX relaxation (e.g. RV, IC, ISC, fluorescence and phosphorescence),<sup>4</sup> written as:

$$\frac{d[PpIX]}{dt} = - \left( \sum_i k_i \right) [PpIX], \quad (3.1)$$

where  $\frac{d[PpIX]}{dt}$  represents the temporal evolution of the PpIX ground state concentration, and  $k_i$  represents the characteristic rates of each relaxation process.

Integrating (3.1), we obtain:

$$\ln [PpIX_t] = -kt + \ln [PpIX_0], \quad (3.2)$$

where  $k$  represents the PpIX decay rate, and  $[PpIX_t]$  is the PpIX concentration at  $t$  time. Through the Lambert-Beer's law, we can directly relate the concentration and absorbance of the PpIX, so, we obtain

$$\ln A_t = -kt + \ln A_0, \quad (3.3)$$

where  $A_0$  and  $A_t$  are the PpIX absorbance at initial and  $t$  time respectively.

#### 3.1.3.2 PpIX modification mediated by ultrasound and light irradiation.

Upon *light irradiation* and in the presence of oxygen, PpIX forms visible absorbing photoproducts (Pp) at 670nm band approximately.<sup>87,88</sup> It was observed that the absorbance values of the Pp linearly grew over illumination time as follow:

$$A_t = k_{Pp} \cdot t, \quad (3.4)$$

where  $k_{Pp}$  is the Pp formation rate,  $t$  is illumination time and  $A_t$  is the Pp absorbance value at  $t$  time.

Upon *ultrasound irradiation* and in the presence of oxygen, it was observed that the PpIX absorbing band at approx. 280 nm increased over sonication time, so it was

thought to represent a formation of sonoproducts (Sp). It was found that the absorbance values of the Sp linearly grew over sonication time as follow:

$$A_t = k_{Sp} \cdot t + a, \quad (3.5)$$

where  $k_{Sp}$  is the Sp formation rate,  $t$  is the sonication time,  $A_t$  is the Sp absorbance at  $t$  time, and  $a$  is the initial PpIX absorbance in the range of 275-285 nm, which has a directly dependence with initial concentration of PpIX.

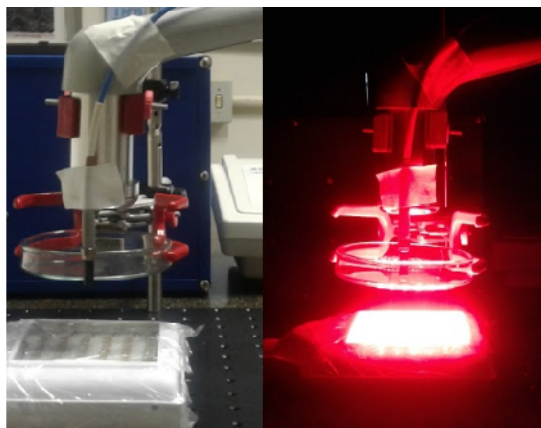
### 3.1.4 Experimental procedures

#### 3.1.4.1 SD action at different PpIX concentrations.

Before sonication, the stock solution was diluted in DMSO to obtain final PpIX concentrations of 1, 3, 5, 10 and 20  $\mu\text{M}$ . Then, PpIX solutions were sonicated during 15 minutes with ultrasound intensity of  $1.5 \text{ W/cm}^2$ , modulation frequency of 100 Hz and duty cycle of 50%. The absorption spectrum was measured before and after every 3 minutes of sonication to analyze the sonodynamic (SD) action under different initial concentrations of the PpIX. In order to verify the solution stability, the samples were stored in a dark environment at 4 °C, the absorption spectra was measured again 12 hours later.

#### 3.1.4.2 SD, PD and combined action at different source intensities.

PpIX solutions with concentration of 5  $\mu\text{M}$  were divided in five groups related to the 5 actions we wanted to study: the sonodynamic (SD), photodynamic (PD), sonophotodynamic (SPD), SD+PD and PD+SD action. The last 3 mentioned actions involve the irradiation of both exciting sources but following different protocols, explained below. At **SD group**, the solutions were sonicated with ultrasound intensities of 1, 1.5 and 2  $\text{W/cm}^2$ , pulse repetition frequency of 100Hz and duty cycle of 50%. At **PD group**, the solutions were illuminated with irradiance of 30 and 50  $\text{mW/cm}^2$ . At **SPD group**, the solutions were irradiated with both ultrasound and red laser light simultaneously as shown in Figure 26, applying ultrasound and light intensity of 1  $\text{W/cm}^2$ -50  $\text{mW/cm}^2$ , 1.5  $\text{W/cm}^2$ -30  $\text{mW/cm}^2$ , 1.5  $\text{W/cm}^2$ -50  $\text{mW/cm}^2$  and 2  $\text{W/cm}^2$ -30  $\text{mW/cm}^2$ , respectively. For these 3 groups, the irradiation time was 30 minutes. Different source intensities were applied in order to determine the relation between PpIX degradation and source intensity. At **SD+PD group**, PpIX solution was firstly sonicated with ultrasound intensity of 1.5  $\text{W/cm}^2$ , pulse repetition frequency of 100 Hz and duty cycle of 50% during 30 minutes. After that, the same solution was illuminated with irradiance of 30  $\text{mW/cm}^2$  during 30 more minutes. Finally, at **PD+SD group**, PpIX solution was irradiated with the same source parameters but in opposite order of the previous group. According to the measured temperatures during SD, PD and SPD action, the light and US intensities applied in these two groups were chosen in such a way that they do not generate a sufficient increase in temperature to generate heating effects. By the SD+PD, PD+SD and SPD groups, it was



**Figure 26** – Experimental setup for experiments of the SPD group.

Source: By the author

possible to compare the effects generated by the combined action applying the same total dose, but delivered in three different ways. The absorption spectrum was measured before and after every 5 minutes of irradiation in all groups.

### 3.1.5 Macroscopic and microscopic analysis

During the exposure time, the increase in temperature of each solutions was monitored with a digital thermometer. The PpIX absorption spectrum was measured in the range of 260-700 *nm* using a spectrophotometer Varian Cary 50 (Varian, Australia).

#### 3.1.5.1 Statistical analysis

All the data are from three independent experiments, so they were presented as means $\pm$ standard deviation. In order to identify if the data had a normal distribution, it was performed the Shapiro-Wilks statistical test. The one-way analysis of variance (ANOVA) was used to analyze differences among groups. All graphs and statistical analyses were performed with Origin 9.50 software (OriginPro, USA). Differences with  $p < 0.05$  were considered statistically significant.

## 3.2 *In vivo* experiments

### 3.2.1 Animals

Male Wistar Hannover rats weighing 250-300 g were acquired from the University of São Paulo campus of Ribeirão Preto (São Paulo, Brazil) and used to induce necrosis in liver cells applying the SD, PD and the combined action (SPD, SD+PD and PD+SD action). They were housed in animal cages on a 12 hours light–dark illumination schedule. All animal procedures were carried out with the standards required by the Ethics Committee



in Use of Animals (CEUA) of the São Carlos Institute of Physics at the University of São Paulo. This study protocol has a process number of N<sup>o</sup> 2564110719 (see annex A).

### 3.2.1.1 Administration of ALA

Solutions of 5-ALA (PDT Pharma, Brazil) were freshly prepared by dissolving 100 mg of ALA in 1 mL of phosphate-buffered saline (PBS: 136.9 mM sodium chloride, 2.7 mM potassium chloride, 8.1 mM di-sodium hydrogen phosphate, 1.5 mM potassium di-hydrogen phosphate, pH=7.0). The pH of the solution was adjusted to 5.0–6.5 by addition of sodium hydroxide. This solution was used within 10 min after preparation. A dose of 500 mg/kg<sup>-1</sup> body weight of ALA was intraperitoneal injected under inhalation anesthesia with isoflurane (BioChimico<sup>®</sup>, Brazil) between 2 and 4% in oxygen - except for the three animals where the PpIX accumulation was monitored, these ones were under general anesthesia.

### 3.2.2 Sono-photodynamic system

A Sono-photodynamic device that allows the ultrasound and light irradiation individually or together was specially built for this study. It's composed mainly by a probe with the implementation of a 300 μm UV-Visible optical fiber (Ocean Optics inc, USA) for laser light delivery. As shown at Figure 27, the transducer (effective radiation area: 3.0 ± 0.3 cm<sup>2</sup>, diameter: 2.5 cm) has a hole (area: 0.13 ± 0.02 cm<sup>2</sup>, diameter: 4 mm) in the middle where the fiber optic ends. The transducer can operate at continuous or pulsed mode, ultrasound intensity: 0-3 W/cm<sup>2</sup>, ultrasound frequency: 1-3 MHz, pulse repetition frequency: 16, 48 and 100 Hz, and duty cycle: 10, 20 and 50%). The light source was a multiFiber diode laser (QuantumTech, Brazil) operating at 635 nm, with controlled power from 0-500 mW.

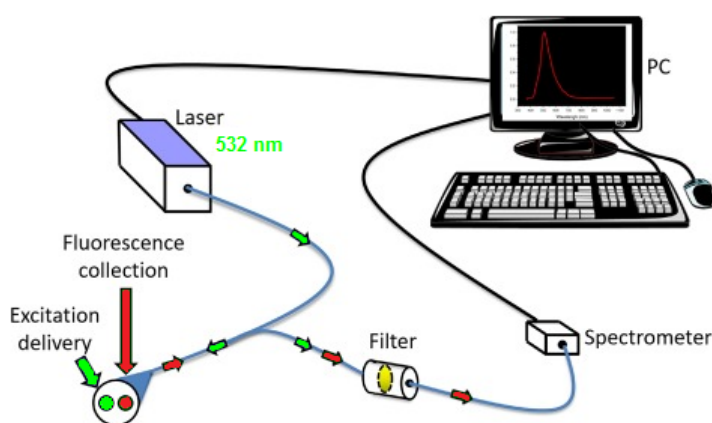


**Figure 27** – The sono-photodynamic probe is composed by an ultrasound transducer with the implementation of a UV-Visible optical fiber positioned in the middle.

Source: By the author

### 3.2.3 Fluorescence detection of PpIX in liver

The time for PpIX accumulation in the liver after ALA injection was 3 hours based on the work of Otake, M. *et al.* where the pharmacokinetics of ALA was investigated.<sup>85</sup> This time between injection and liver treatment was used for all experiments. The accumulation of ALA-induced PpIX at rat liver was monitored by Steady-state fluorescence spectroscopy (SSFS), measuring the fluorescence spectrum before ALA administration (0 minutes), 60, 120 and 180 minutes after ALA injection. The excitation was provided by a frequency-doubled Nd:YAG laser (QuantumTech, Brazil) at 532 nm emitted about 7 mW, assuring no thermal effect by the incident illumination spot. A 600  $\mu\text{m}$  bifurcated optical fiber (Ocean Optics, USA) was used to deliver the laser light and collect the fluorescence from the tissue as shown at Figure 28. A long-pass filter at 550 nm (GG550, Schott, USA) was used to remove the backscattered excitation light. Then, the fluorescence emission was acquired by a spectrophotometer (USB 2000, Ocean Optics, USA) in the range of 500 nm to 800 nm, which was connected to a computer running the OOIBase software (Ocean Optics, USA).



**Figure 28** – Overview scheme of the experimental setup for liver steady state measurements.

Source: Adapted from CAMPOS *et al.*<sup>89</sup>

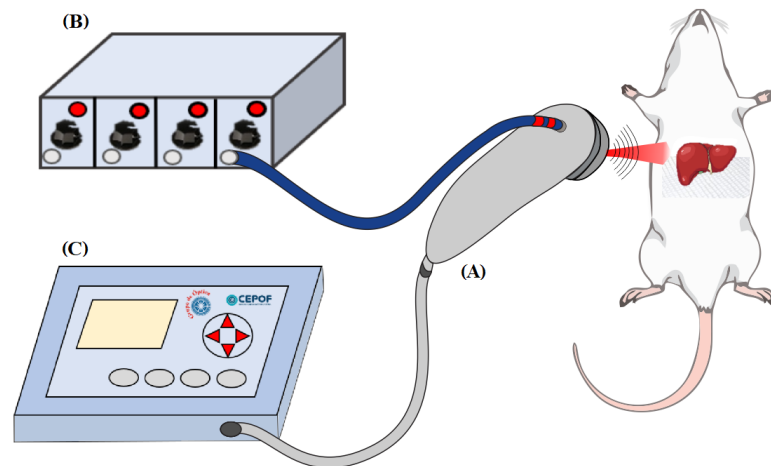
The fluorescence monitoring was carried out just in 3 animals under general anesthesia, however, the fluorescence detection before (180 minutes after ALA injection) and after treatment was measured in all animals. All the fluorescence measurements were recorded at least three different sites of the liver surface.

### 3.2.4 Experimental design

Animals were underwent open surgical intervention after 150 min of ALA administration to expose part of the liver - except for the three animals where the PpIX accumulation was monitored, these ones were underwent open surgical intervention before

ALA injection in order to measure the PpIX fluorescence as explained at section . Prior surgery, animals were anesthetized by intraperitoneal injection of 5% ketamine at a dose of 0.08 mL/100 g body weight and xylazine at a dose of 0.04 mL/100 g of body weight. After the predetermined time for PpIX accumulation in the liver elapsed, a thin layer (3 mm) of acoustic coupling gel was placed on the liver surface before treatments.

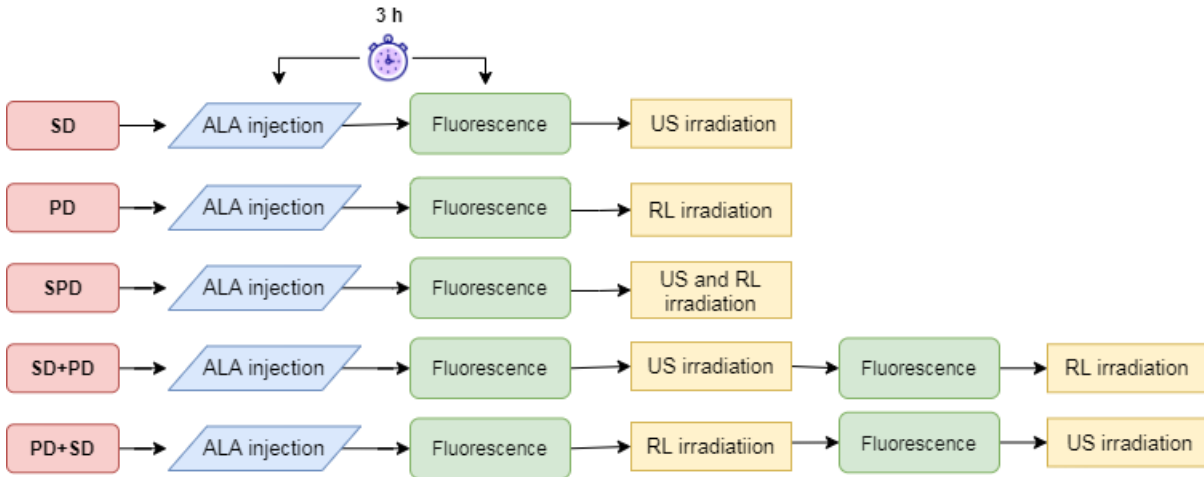
A total of 25 animals were allocated in five treatment groups with three animals each related to the 5 actions we wanted to analyze (SD, PD, SPD, SD+PD and PD+SD action), and five control groups with two animals each. At **SD group**, livers with 5-ALA were sonicated with for 17 minutes. At **PDT group**, livers with 5-ALA were illuminated for 17 minutes. At **SPD group**, livers with 5-ALA were irradiated with both ultrasound and laser light simultaneously as shown in Figure 29. At **SD+PD group**, livers with 5-ALA were sonicated with for 17 minutes, and immediately afterwards the livers were illuminated for more 17 minutes. At **PDT+SDT group**, livers with 5-ALA were illuminated for 17 minutes, immediately afterwards they were sonicated for more 17 minutes. (Figure 30) At control groups, the exposed livers were irradiated as in the previous 5 groups but without ALA administration. For US irradiation, it was used the pulsed mode, US intensity of  $1.5 \text{ W/cm}^2$ , transducer frequency of 1MHz, pulse repetition frequency of 100 Hz and duty cycle of 50%, delivering a total irradiated ultrasound dose of  $765 \pm 38 \text{ J/cm}^2$ . For laser irradiation, it was applied a total dose of  $180 \pm 9 \text{ J/cm}^2$ .



**Figure 29** – Simultaneous irradiation on PpIX-loaded rat liver using (A) the sonophotodynamic probe connected to (B) a multifiber diode laser and (C) an ultrasound machine.

Source: By the author

After treatment, the animals were sutured and allowed to recover from surgery. The autopsy was performed following the animals' death by anesthesia overdose 30 h after irradiation, minimum time needed to observe necrosis according previous studies.<sup>90-92</sup> The exposed livers were removed and collected in containers with buffered formaldehyde solution for later macroscopic and microscopic analysis.



**Figure 30** – Flow chart of each protocol. US:ultrasound, RL:red light

Source: By the author

### 3.2.5 Macroscopic and microscopic analysis

For **macroscopic analysis**, the temperature on the surface of the rat liver, which was in contact with the transducer, was measured before and after each irradiation using an infrared camera FLK-Ti400 60 Hz (Fluke<sup>®</sup>, EUA). The acoustic coupling gel that was placed on the irradiation area, was removed at the end of the treatment for the temperature measurement. The removed livers were inspected to obtain the superficial width of necrosis and its general aspects.

For **microscopic analysis**, liver sections orthogonal to the illumination central area were placed on cassettes and fixed in buffered formaldehyde solution, following by dehydration, clearing and paraffin wax embedding. Each paraffin-embedded sample was cut in sections of 4- $\mu\text{m}$  using a Leica RM 2125RT microtome (Leica, USA). These thin sections were mounted on microscope slides, deparaffinised and stained with haematoxylin and eosin (H&E). Later, the slides were digitized using the Panoramic DESCK device (3DHISTECH, Hungary) for histological slides. The *qualitative assessment* of the digitized histological slides was performed using the Case Viewer program (3DHISTECH, Hungary), which allowed us to determine the overall aspects of the necrotic and healthy portions of the liver. The *quantitative assessment* of histological slides was carried out by the image processing of the scanned histological slides in order to differentiate the necrotic tissue area from the non-necrotic one. The image processing was accomplished with a classification algorithm implemented in Python, using the open-source libraries NumPy and Scikit-learn. The classifier used was the Random Forest that uses various decision trees to classify the data.<sup>93</sup> The overall method decision is the mode of trees' decision.

The average values of the superficial width of necrosis ( $2r_{NEC}$ ) and the necrotic

tissue area ( $A_{NEC}$ ) were calculated by Origin 9.50 software (OriginPro, USA), considering the results of three independent *in vivo* experiments for each group, so the data were presented as means  $\pm$  standard deviation.

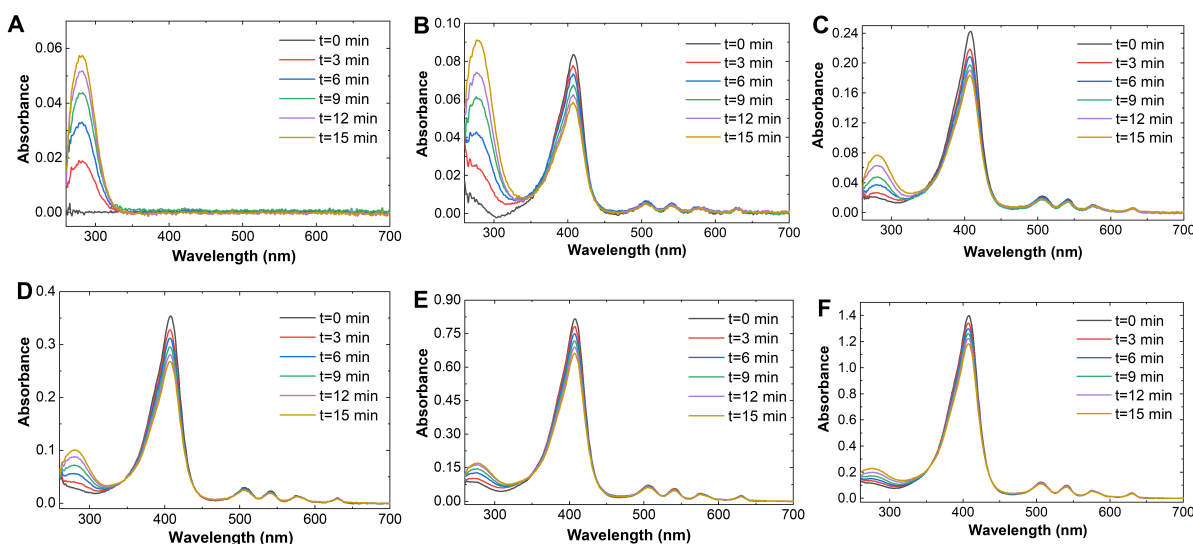


## 4 RESULTS AND DISCUSSION

### 4.1 *In vitro* experiments

#### 4.1.1 Effects of SD action on PpIX solutions with different concentrations.

In order to analyze the SD action at different PpIX concentrations, PpIX solutions with concentration of 1, 3, 5, 10 and 20  $\mu\text{M}$  were sonicated during 15 min. As expected, the PpIX absorption spectra before sonication showed a small band in the range near-ultraviolet region (approx. 280 nm), an strongly absorption band at violet-blue region (approx. 407 nm) and four minor absorption bands at 505, 539, 572, and 630 nm shown at Figure 31 (B-F, black line).<sup>94</sup> The well defined Soret and Q-bands for all molar concentration used in this work showed that there were not formation of PpIX aggregates.<sup>95</sup>

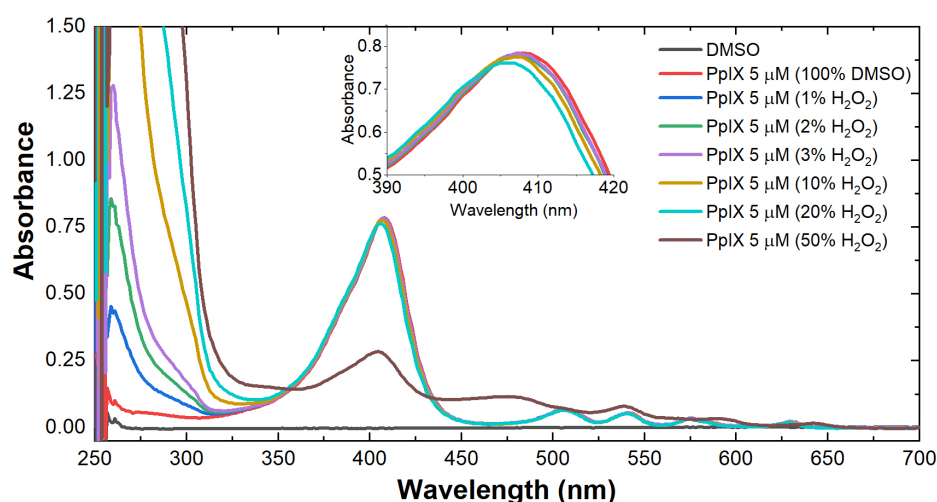


**Figure 31** – The absorption spectra of (A) DMSO, and (B) PpIX 1, (C) 3, (D) 5, (E) 10 and (F) 20  $\mu\text{M}$  before and after each 3 minutes of sonication - SD action.

Source: By the author

*Ultrasound-mediated PpIX modification.* Upon ultrasound irradiation, the absorbance in approx. 280 nm increased over exposure time (Figure 31, color lines), so it was considered a sonoproduct (Sp). It was thought that the Sp could be hydrogen peroxide ( $\text{H}_2\text{O}_2$ ), since the experiments were carried out in an open environment, where the DMSO, an hygroscopic solvent, could have absorbed water from the atmosphere quickly. This fact gives the possibility that the US irradiation could produce OH radicals and H radicals by cavitation, following by the recombination of the OH radical to finally form  $\text{H}_2\text{O}_2$ .<sup>96,97</sup> To evaluate this case, solutions of PpIX 5  $\mu\text{M}$  were prepared using DMSO and  $\text{H}_2\text{O}_2$  as solvents, with different percentages (1-50%) of  $\text{H}_2\text{O}_2$ . Then we compared the

absorption spectra of these solutions (Figure 32) with the absorption spectra of the sonified PpIX  $5\mu\text{M}$  solution (Figure 31-D). In Figure 32, it's shown that the absorption spectra suffered a spectral shift to the left as the percentage of  $\text{H}_2\text{O}_2$  in the solvent increased. Besides, the absorbance value in the Soret and Q bands did not change with the presence in low percentage of A  $\text{H}_2\text{O}_2$ , except at 50% of the solvent volume. Analyzing the ultraviolet region, it was observed that the Sp formation during sonication was approximately at 280 nm, while the formation of bands at ultraviolet region generated by addition of  $\text{H}_2\text{O}_2$  was approximately at 260 nm. So, the hypothesis that Sp could be  $\text{H}_2\text{O}_2$  molecules could not be proven, but it certainly must be further investigated.



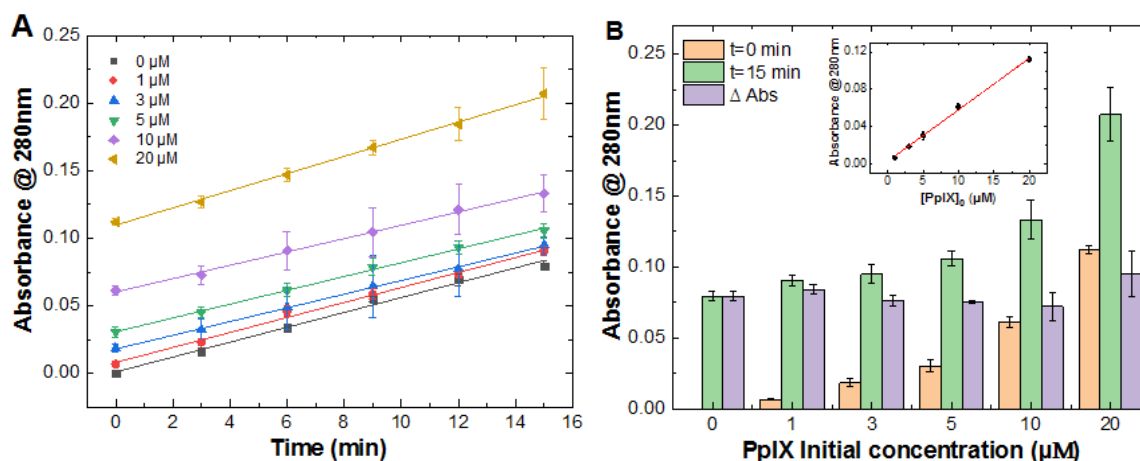
**Figure 32** – The absorption spectrum of a PpIX  $5\mu\text{M}$  solution diluted in DMSO and  $\text{H}_2\text{O}_2$  with different percentages (1-50%) of  $\text{H}_2\text{O}_2$ .

Source: By the author

In Figure 33-A is shown that the Sp absorbance in this range had a linear behavior with sonication time. Performing the linear fitting, by Eq.3.5, it was obtained the Sp formation rates ( $k_{Sp}$ ) shown at Figure 35-A. The  $k_{Sp}$  values were similar for the 6 cases (0,1,3,5,10 and 20  $\mu\text{M}$ ), this indicates that the formation of Sp is independent of the PpIX initial concentration. The Sp absorbance values before and after sonication were represented in a bar graphic shown in Figure 33-B, as well as the Sp absorbance variation which were similar for the 6 cases. It's important to note that PpIX initial absorbance values at 280 nm band showed a good linear dependence with PpIX concentration according the Beer–Lambert law (little graphic in Figure 33-B).

*Ultrasound-mediated PpIX degradation.* The PpIX absorbance decayed significantly at Soret and Q bands following ultrasound irradiation evidencing ultrasound-mediated PpIX degradation (Fig. 31-color lines). As shown in Figure 34-A and Figure 34-B, the natural logarithm of the PpIX normalized absorbance values ( $Abs_t/Abs_0$ ) decreased linearly over sonication time at Soret band (PpIX 1-20  $\mu\text{M}$ ) and Q bands (PpIX 20  $\mu\text{M}$ ), respectively. In order to analyze the sonobleaching of PpIX, it was selected the Soret band since it is the



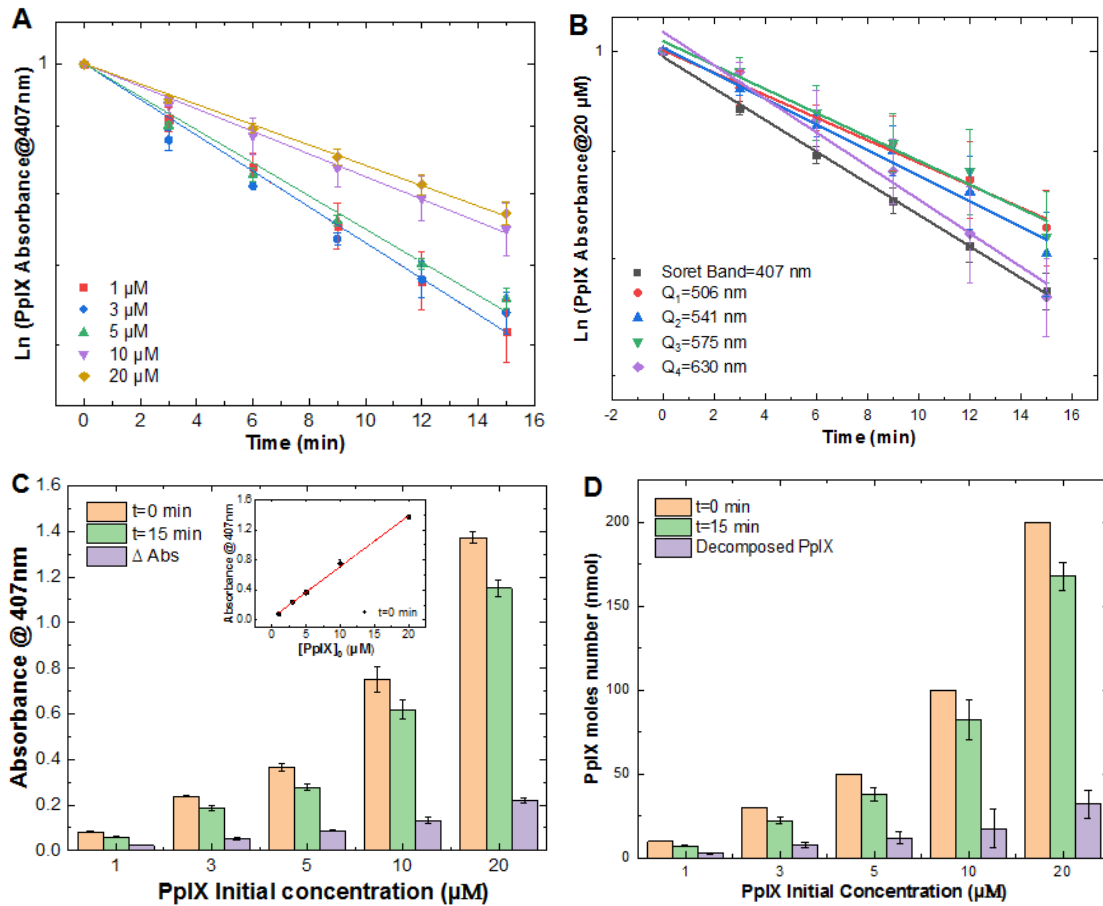


**Figure 33** – (A) The mean absorbance values at 280 nm over sonication time. (B) The mean absorbance values at 280 nm before and after ultrasound irradiation for each solution (1-20  $\mu\text{M}$ ). The solid line and error bars represent the linear fit and standard deviation, respectively.

Source: By the author

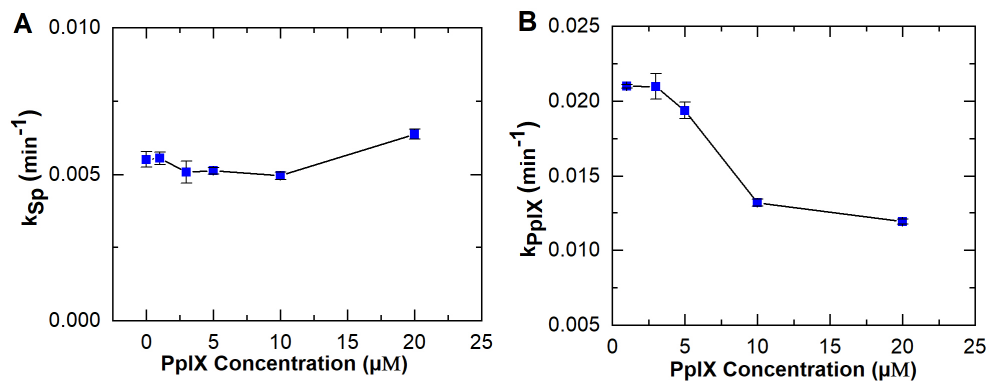
predominant absorption band. The initial PpIX absorbance at this band showed a good linear dependence with PpIX concentration, according the Beer–Lambert law (little graphic in Figure 34-C). Performing the linear fitting as shown in Figure 34-A, the PpIX decay rate ( $k$ ) was calculated according Eq.3.3 and graphed in Figure 35-B, getting that  $k$  decreased as PpIX concentration increased, however, the PpIX absorbance variation at Soret band after 15 min of sonication was greater in solutions with higher PpIX concentration (Figure 34-C). So, the amount of decomposed PpIX moles showed in Fig. 34-D (purple bar), which was calculated multiplying the variation of PpIX concentration after sonication time with the initial amount of PpIX solution, increased from  $3.0 \pm 0.4$  nmol ( $27 \pm 1\%$  of the PpIX initial moles number) to  $8 \pm 2$  nmol ( $26 \pm 1\%$ ),  $12 \pm 3$  nmol ( $24 \pm 2\%$ ),  $18 \pm 6$  nmol ( $18 \pm 2\%$ ) and then to  $32 \pm 5$  nmol ( $16 \pm 2\%$ ) when the PpIX initial concentration was increased from 1  $\mu\text{M}$  to 3, 5, 10 and then to 20  $\mu\text{M}$  respectively. This results were similar to those obtained by Haobo, X. *et al.*, who studied the ultrasound-mediate PpIX degradation in Human THP-1 cells culture.<sup>18</sup> It is important to mention here that during and after of the sonication, the remaining Soret and Q-bands do not show any wavelength shift as well changes in the band broadening, which indicates that aggregates were also not formed in this process.<sup>95</sup>

Under the ultrasound parameters used in these experiments, it was detected a temperature increase from  $26 \pm 1$  °C to  $29 \pm 1$  °C after 15 min of sonication. In order to evaluate the heating effect on PpIX degradation or modification, a 5 $\mu\text{M}$  PpIX solution (diluted in DMSO) was heated to 45 °C, followed immediately by the absorption spectrum measurement of the solution shown in the Figure 36. As the absorbance values in the Soret and Q bands did not decrease significantly, heating effects were not considered in the analyze of the PpIX degradation obtained by the sonodynamic action.



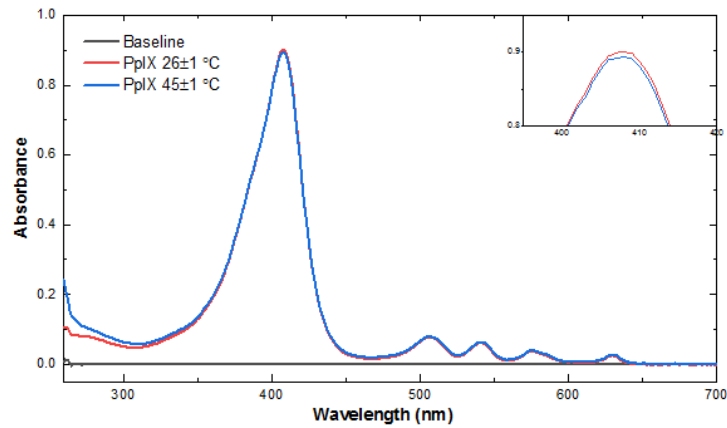
**Figure 34** – Graphic representation of the natural logarithm of the mean normalized absorbance at (A) Soret band (1-20  $\mu\text{M}$ ) and (B) Q bands (PpIX 20  $\mu\text{M}$ ) over sonication time. (C) The mean absorbance at Soret band before and after sonication. (D) The mean number of decomposed moles of PpIX by 15 min of sonication (purple bars). Solid line and error bars represent the linear fit and standard deviation, respectively.

Source: By the author



**Figure 35** – (A) The mean Sp formation rate  $k_{Sp}$  at approx. 280 nm and (B) the mean PpIX decay rate  $k_{PpIX}$  at Soret band according the PpIX initial concentration. The error bars represent the standard deviation.

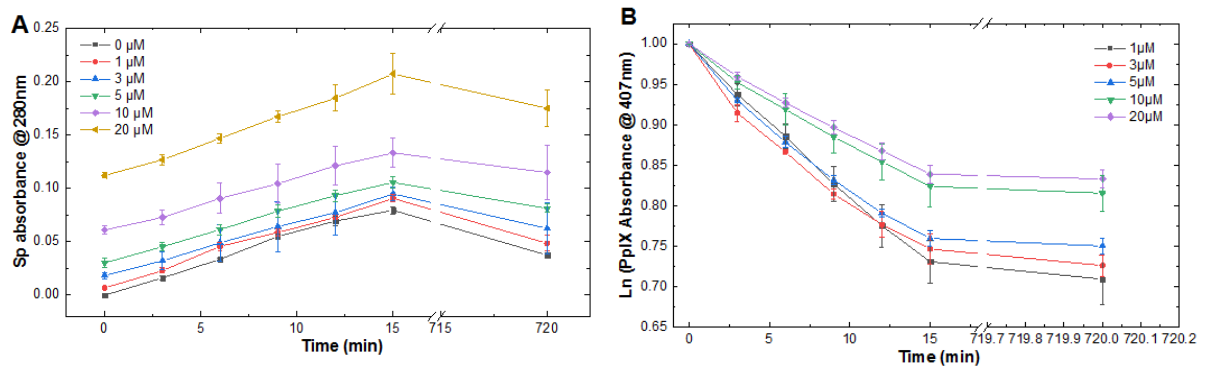
Source: By the author



**Figure 36** – The absorption spectrum of PpIX solution before and after being heated up to 45 °C

Source: By the author

After 12 hours of the experiment, period in which the sonified solutions were kept in a dark room, the PpIX absorption spectra was measured again. It was noted that the absorbance at 280 nm band had decreased significantly, evidencing the Sp instability (Fig. 37-A). However, the absorbance at Soret band did not changed significantly, evidencing the stability of the PpIX solutions (Fig. 37-B).



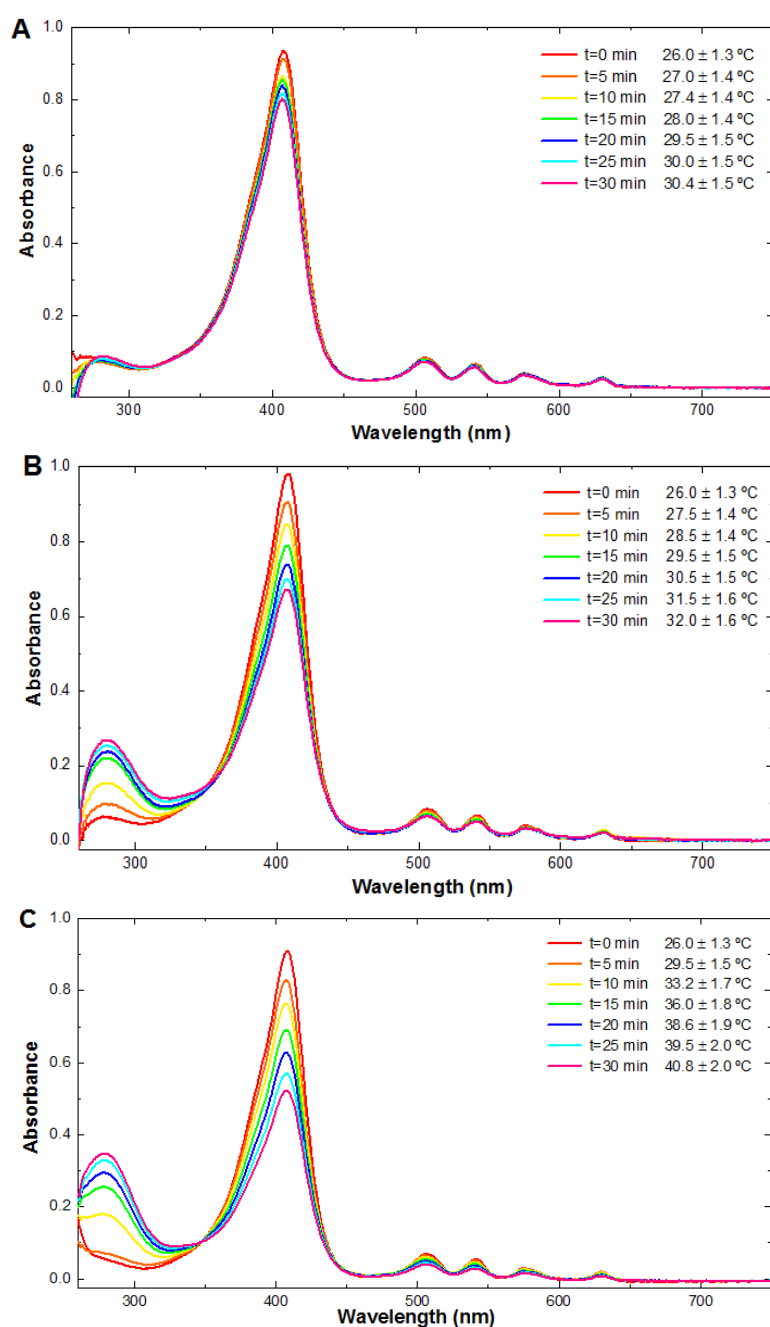
**Figure 37** – (A) The mean Sp absorbance at 280 nm and (B) the natural logarithm of the mean PpIX normalized absorbance at Soret band during 15 min of ultrasound irradiation and 12 hours after that. Error bars represent the standard deviation.

Source: By the author

#### 4.1.2 Effects of the SD, PD and SPD action on PpIX solutions at different source intensities.

At **SD group**, the PPIX 5  $\mu\text{M}$  solutions were sonicated with pulse repetition frequency of 100 Hz, duty cycle of 50% and US intensities of 1, 1.5 and 2  $\text{W}/\text{cm}^2$  during 30 minutes. The Figure 38 showed that the absorbance values at Soret and Q bands decreased, while in 280 nm the absorbance values increased every 5 min of sonication. It's important

to note that despite using a pulsed ultrasound, the temperature of the solution increases with the source intensity.

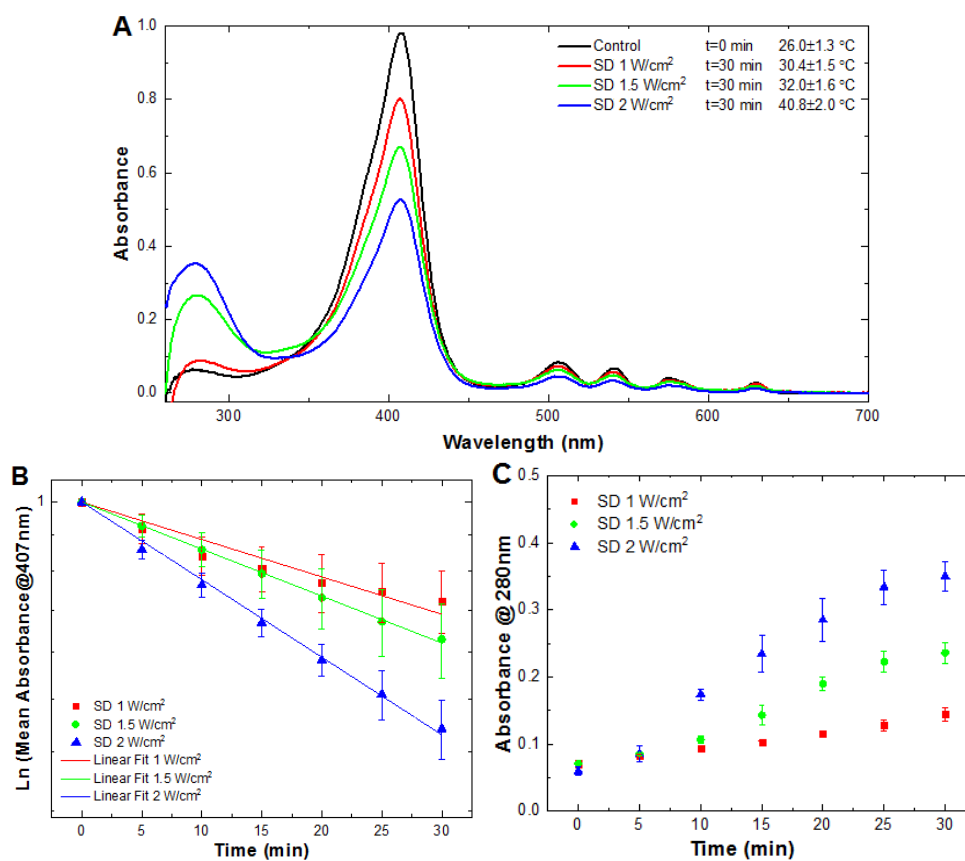


**Figure 38** – The absorption spectra and temperature of the PpIX 5  $\mu\text{M}$  solution each 5 min of sonication with pulse repetition frequency of 100 Hz, duty cycle of 50% and ultrasound intensity of (A) 1, (B) 1.5 and (C) 2  $\text{W}/\text{cm}^2$ .

Source: By the author

Comparing the PpIX absorption spectra recorded immediately after 30 minutes of sonication applying three different US intensities (Figure 39-A), we can see that PpIX absorbance values at Soret and Q bands decreased as a higher US intensity was applied.

That is, the degradation of the PpIX molecules can be intensified increasing the US intensity. In order to analyze the sonobleaching of PpIX, it was selected the Soret band since it is the predominant absorption peak. The natural logarithm of the PpIX normalized absorbance ( $Abs_t/Abs_0$ ) in this band decreased linearly over sonication time for the three cases, as shown in Figure 39-B. Performing the linear fitting, it was obtained that PpIX decay rate ( $k$ ) values increased from  $(0.008 \pm 0.001) \text{ min}^{-1}$  to  $(0.01 \pm 0.0001) \text{ min}^{-1}$  and then to  $(0.02 \pm 0.0003) \text{ min}^{-1}$  when the US intensity was increased from 1 to 1.5 and then to  $2 \text{ W/cm}^2$ , respectively as shown in Table 9. In order to measure the Pp formation in solution, it was analyzed the 280 nm band. Figure 39-C shows that the absorbance in this band increases over sonication time for the three US intensities, but the greatest Sp production was found to be associated with higher-ultrasound intensity irradiation.



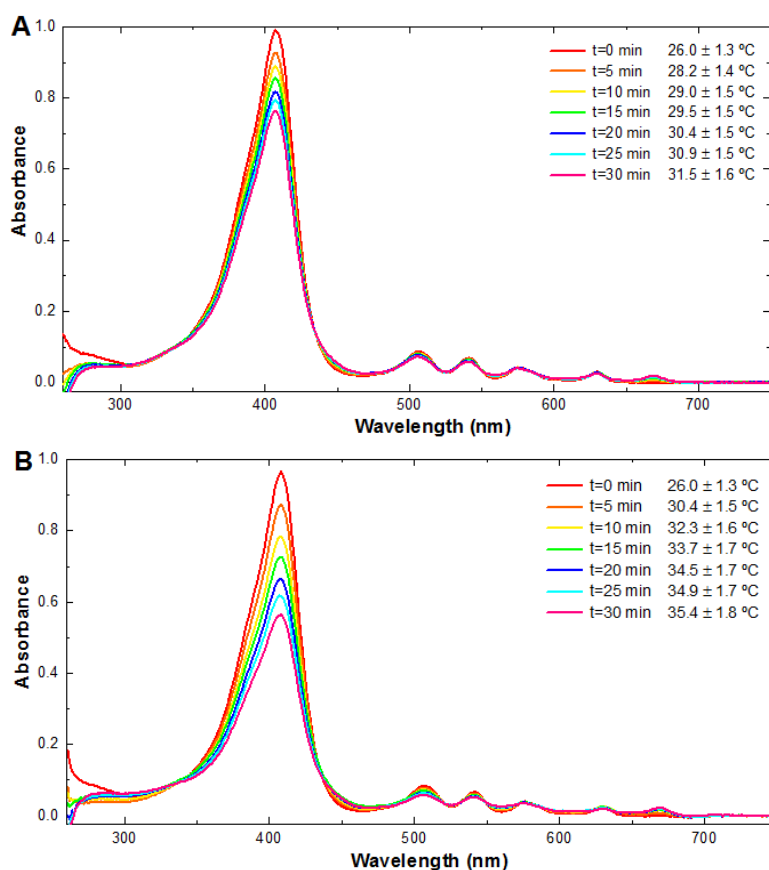
**Figure 39** – (A) The absorption spectra and temperature of the PpIX  $5 \mu\text{M}$  solution before and after 30 min of sonication with three different US intensities. (B) Graphic representation of the natural logarithm of the mean normalized absorbance of PpIX at Soret band over sonication time. (C) Mean absorbance at 280 nm band over sonication time. Error bars represent the standard deviation.

Source: By the author

On the other hand, based on the fact that the sonoluminescence phenomenon is a possible mechanisms that occurs during the sonodynamic action, it was expected to observe the formation of some photoproducts (Pp) at 670 nm in the absorption spectrum, as

results of the interaction of US-mediated light with PpIX, however, under the parameters used, it was not observed. Therefore, we assumed that the US-mediated PpIX degradation was predominantly through the mechanical forces or the formation of ROS.

At **PD group**, the PPIX 5  $\mu\text{M}$  solutions were exposed to red laser light with irradiance of 30 and 50  $\text{mW}/\text{cm}^2$  during 30 minutes. The Figure 40 showed that the absorbance values at Soret and Q bands decreased, while the temperature and the absorbance values in 670 nm increased every 5 min of illumination.

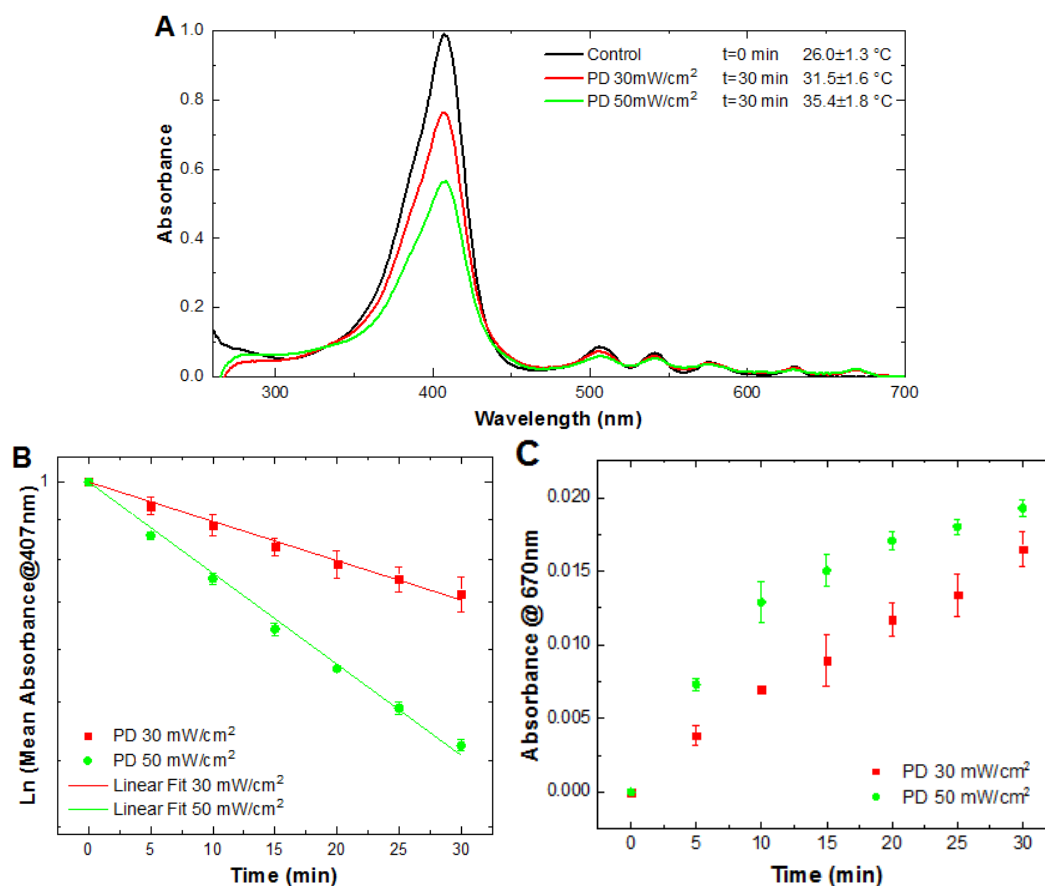


**Figure 40** – The absorption spectra and temperature of the PpIX 5  $\mu\text{M}$  solution each 5 min of red light irradiation with irradiance of (A) 30 and (B) 50  $\text{mW}/\text{cm}^2$ .

Source: By the author

Comparing the PpIX absorption spectra recorded at 30 min time of illumination under both irradiances (Figure 41-A), it's clearly seen that the PpIX absorbance values at Soret and Q bands decreased as a higher irradiance was applied. That is, the degradation of the PpIX molecules can be intensified increasing the irradiance. As in the previous group, the Soret band was selected to measure the photobleaching of PpIX. The natural logarithm of the PpIX normalized absorbance values shown in Figure 41-B decreased linearly over light irradiation time for the two cases. Performing the linear fitting, it was obtained that PpIX decay rate ( $k$ ) values at Soret band increased from  $(0.008 \pm 0.001) \text{ min}^{-1}$  to  $(0.020 \pm 0.0003) \text{ min}^{-1}$  when the irradiance was increased from 30 to 50  $\text{W}/\text{cm}^2$ ,

respectively as shown in Table 9. In order to measure the Pp formation in solution, it was analyzed the 670 nm band. Figure 41-C shows that the absorbance in this band increases over illumination time for both light intensities, but the greatest production of photoproducts was found to be associated with higher-irradiance.<sup>87,98</sup>

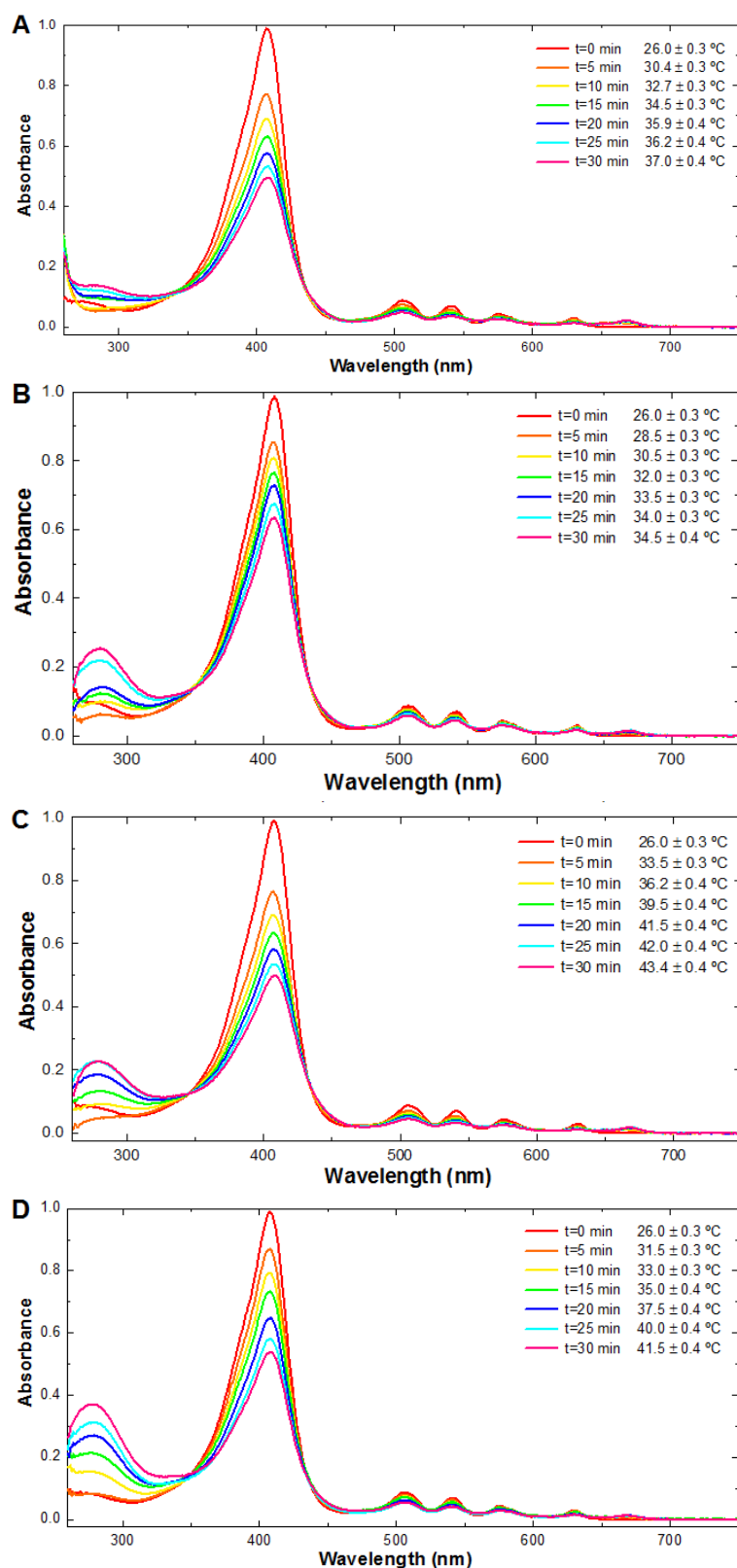


**Figure 41** – (A) The absorption spectra and temperature of the PpIX 5  $\mu$ M solution before and after 30 min of illumination with two different irradiances. (B) Graphic representation of the natural logarithm of the mean normalized absorbance of PpIX at Soret band over illumination time. (C) Mean absorbance at 670 nm band over illumination time. The error bars represent the standard deviation.

Source: By the author

At **SPD group**, the PPIX 5  $\mu$ M solutions were simultaneously sonicated and illuminated during 30 min under different US and light intensities. The Figure 42 showed that every 5 min of combined irradiation, the absorbance values at Soret and Q bands decreased evidencing PpIX degradation, while the absorbance values in 280 and 670 nm band increased evidencing the Sp and Pp formation, respectively.

The PpIX absorption spectra shown in Figure 43-A allowed us to compare PpIX absorbance at Soret band, as well as the Sp and Pp formation after 30 minutes of combined irradiation under different ultrasound and light intensities. As shown in Figure 43-B, the natural logarithm of the PpIX normalized absorbance values at Soret band decreased

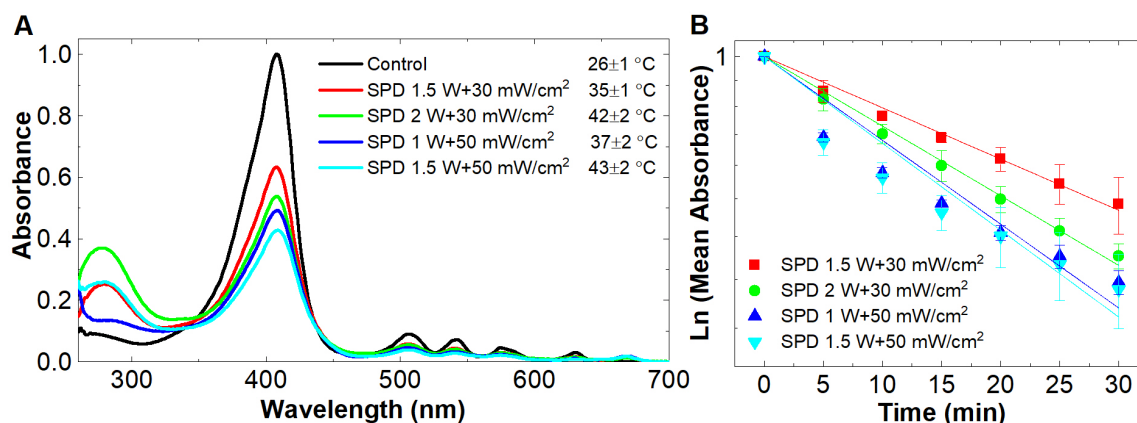


**Figure 42** – The absorption spectra and temperature of the PpIX 5  $\mu$ M solution each 5 min of simultaneous US and light irradiation. The US intensity and irradiance applied were: (A) 1  $W/cm^2$ -50  $mW/cm^2$ , (B) 1.5-30, (C) 1.5-50 and (D) 2-30, respectively.

Source: By the author



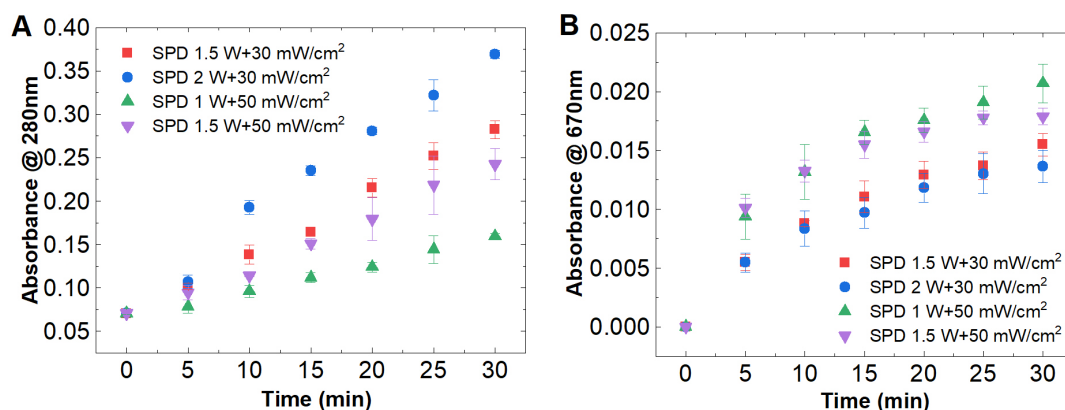
linearly over irradiation time in all 4 cases. Performing the linear fitting, it was obtained the PpIX decay rate ( $k$ ) values at Soret band (Table 9), which evidenced an increase in the PpIX degradation when a higher intensity of the sources, either one or both, was applied. Besides, it was noticed that the PpIX decay rate obtained by the SPD action ( $k_{SPD}$ ) is approximately the sum of the PpIX decay rate obtained by SD ( $k_{SD}$ ) and PD ( $k_{PD}$ ) action, that is the SPD action had an additive PpIX decay rate ( $k_{SPD} \simeq k_{SD} + k_{PD}$ ).



**Figure 43** – (A) The absorption spectra and temperature of the PpIX 5  $\mu\text{M}$  solution before and after 30 min of both ultrasound and light irradiation simultaneously under four different intensity values; (B) Graphic representation of the natural logarithm of the mean normalized absorbance of PpIX at Soret band over irradiation time. Solid line and error bars represent the linear fit and standard deviation, respectively.

Source: By the author

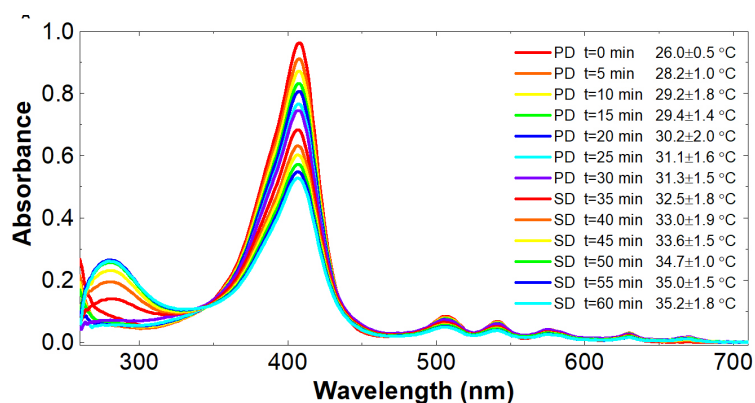
In this group, both Sp and Pp were formed since ultrasound and light were involved in the excitation process. As shown at 44-A, the Sp absorbance at approx. 280 nm increased as US intensity increased (1-2  $W/cm^2$ ). Comparing two experiments in which solutions were sonicated with the same US intensity but illuminated with different red laser irradiance (red-cyan line), it was noted that absorbance at 280 nm increased slightly faster over time, by applying 30  $mW/cm^2$  than 50  $mW/cm^2$  of irradiance. This suggested that light could influence the formation of Sp. As shown at 44-B, the Pp absorbance at approx. 670 nm visibly increased with increasing irradiance (30-50  $W/cm^2$ ). Comparing two experiments in which solutions were illuminated with the same irradiance but sonicated with different US intensity (blue-cyan and red-green line), it was noted that absorbance at 670 nm increased slightly faster over time, by applying lower US. In fact, the higher US and light intensities, the more Sp and Pp formation, respectively. However, the effect of light irradiation on Sp formation as well as the US irradiation on Pp formation, and how these Sp and Pp influence the PpIX degradation, need to be further studied.



**Figure 44** – The mean absorbance at (A) 280 nm and (B) 670 nm over irradiation time, under SPD action. Error bars represent the standard deviation.

Source: By the author

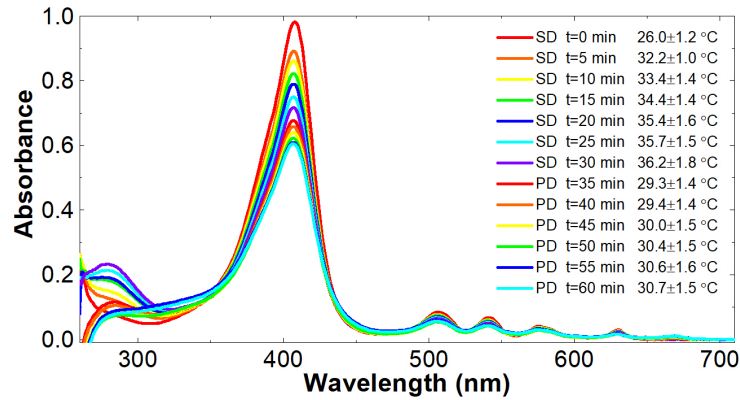
At **PD+SD group**, the PpIX 5  $\mu\text{M}$  solutions were illuminated with 30  $\text{mW}/\text{cm}^2$  for 30 min followed by an immediate sonication with 1.5  $\text{W}/\text{cm}^2$  for more 30 min. The absorption spectra of PpIX solutions recorded every five minutes of irradiation to analyze the PD+SD action, is shown in Figure 45. The PpIX absorbance values at Soret band decreased over illumination and sonication time. During the first phase (PD action), the Pp was formed at 670 nm but it was interrupted and partially degraded by the ultrasound irradiation during the second phase (SD action) as shown in Figure 47-A.



**Figure 45** – The absorption spectra and temperature of the PpIX 5  $\mu\text{M}$  solution each 5 min of irradiation during PD+SD action.

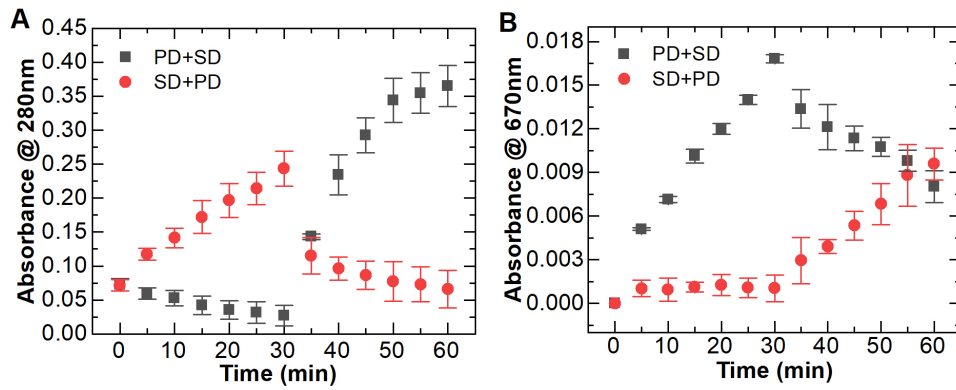
Source: By the author

At **SD+PD group**, the PpIX 5  $\mu\text{M}$  solutions were sonicated with 1.5  $\text{W}/\text{cm}^2$  for 30 min followed by an immediate illumination with 30  $\text{mW}/\text{cm}^2$  for more 30 min. The absorption spectra of PpIX solutions recorded every five minutes of irradiation to analyze the SD+PD action, is shown in Figure 46. The PpIX absorbance values at Soret band decreased over sonication and illumination time. During the first phase (SD action), the Sp were formed at 280 nm but it was interrupted and completely degraded by illumination during the second phase (PD action) as shown in Figure 47-B.



**Figure 46** – The absorption spectra and temperature of the PpIX 5  $\mu$ M solution each 5 min of irradiation during SD+PD action.

Source: By the author



**Figure 47** – The mean absorbance at (A) 280 nm and (B) 670 nm over irradiation time under PD+SD and SD+PD action. Error bars represent the standard deviation.

Source: By the author

**Table 9** – The mean PpIX decay rate ( $k$ ) at Soret band for each action and the additive decay rates ( $k_a$ ) for the combined action. Average  $\pm$  standard deviation.

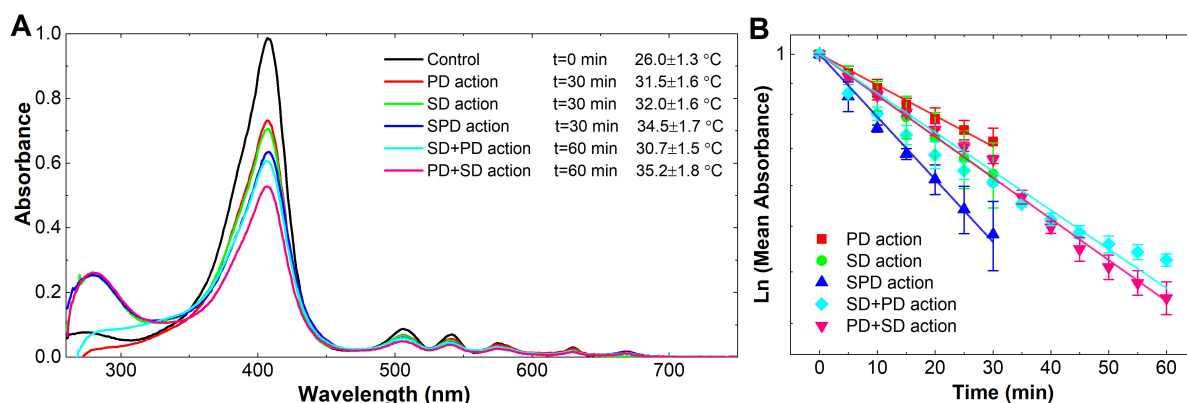
Action	US Intensity ( $W/cm^2$ )	Irradiance ( $mW/cm^2$ )	Experimental decay rate $k_e$ ( $min^{-1}$ )	Additive decay rate $k_a$ ( $min^{-1}$ )
SD	1		$0.008 \pm 0.001$	
	1.5		$0.01 \pm 0.0001$	
	2		$0.02 \pm 0.0003$	
PD		30	$0.008 \pm 0.0002$	
		50	$0.02 \pm 0.0003$	
SPD	1	50	$0.03 \pm 0.002$	$0.03 \pm 0.001$
	1.5	30	$0.02 \pm 0.0004$	$0.02 \pm 0.0003$
	1.5	50	$0.03 \pm 0.002$	$0.03 \pm 0.0004$
	2	30	$0.02 \pm 0.0004$	$0.02 \pm 0.001$
SD+PD	1.5	30	$0.01 \pm 0.0003$	$0.02 \pm 0.0003$
PD+SD	1.5	30	$0.01 \pm 0.0001$	$0.02 \pm 0.0003$

Source: By the author

#### 4.1.3 Spectroscopic comparison among SD, PD, SPD, PD+SD and SD+PD action

In order to compare the effects of each action on the PpIX degradation, some parameters such as PpIX concentration, irradiation time, US intensity and irradiance were fixed to 5  $\mu\text{M}$ , 30 minutes, 1.5  $\text{W}/\text{cm}^2$  and 30  $\text{mW}/\text{cm}^2$ , respectively. The light and US intensities were chosen taking into account the increase in temperature they generated, so that the heating effects could be excluded.

As shown in Figure 48-A, after total irradiation, the PpIX final absorbance at Soret and Q bands decreased more applying a combined action (SPD, SD+PD and PD+SD action) than applying either SD or PD action. That is, PpIX concentration significantly decreased and PpIX molecules were highly degraded using the combined action. The natural logarithm of the PpIX normalized absorbance values shown in Figure 48-B decreased linearly over exposure time for the five cases.

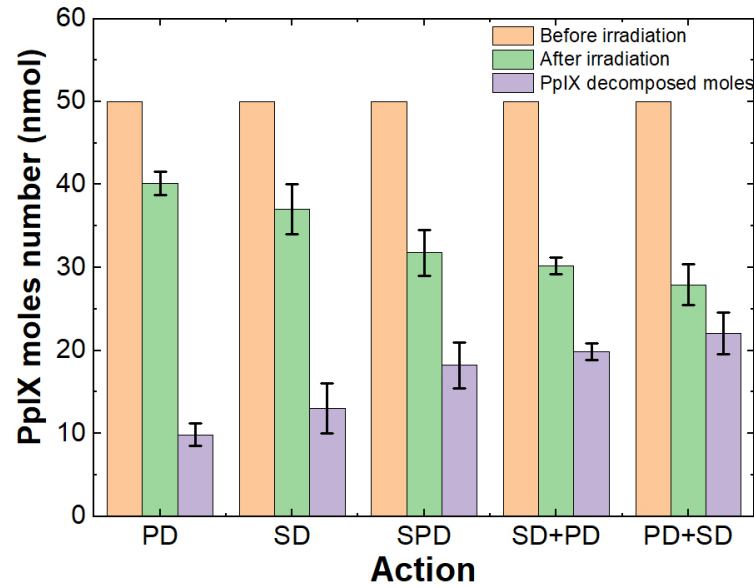


**Figure 48** – (A) The absorption spectra and the temperature of the PpIX solutions after 30 min of irradiation for each action; (B) Graphic representation of the natural logarithm of the mean normalized absorbance of PpIX at Soret band over irradiation time. Applying U.S. intensity of 1.5  $\text{W}/\text{cm}^2$  and irradiance of 30  $\text{mW}/\text{cm}^2$ . The solid line and error bars represent the linear fit and standard deviation, respectively.

Source: By the author

Performing the linear fitting, the PpIX decay rate ( $k$ ) corresponding to each applied action was calculated and shown in Table 9. The  $k$  values obtained for the SPD action were higher instead of others. That is, applying SPD action (blue line), PpIX bleaching was elicited faster than other actions. However, it was observed in Figure 48-A that the lowest absorbance value after irradiation was obtained during the PD+SD action (pink line), and the amount of decomposed PpIX moles shown at Fig.49 increased from  $(10 \pm 1)$  nmol to  $(13 \pm 3)$  nmol,  $(18 \pm 3)$  nmol,  $(20 \pm 1)$  nmol and then to  $(22 \pm 3)$  nmol under the PD, SD, SPD, SD+PD and PD+SD action, respectively.

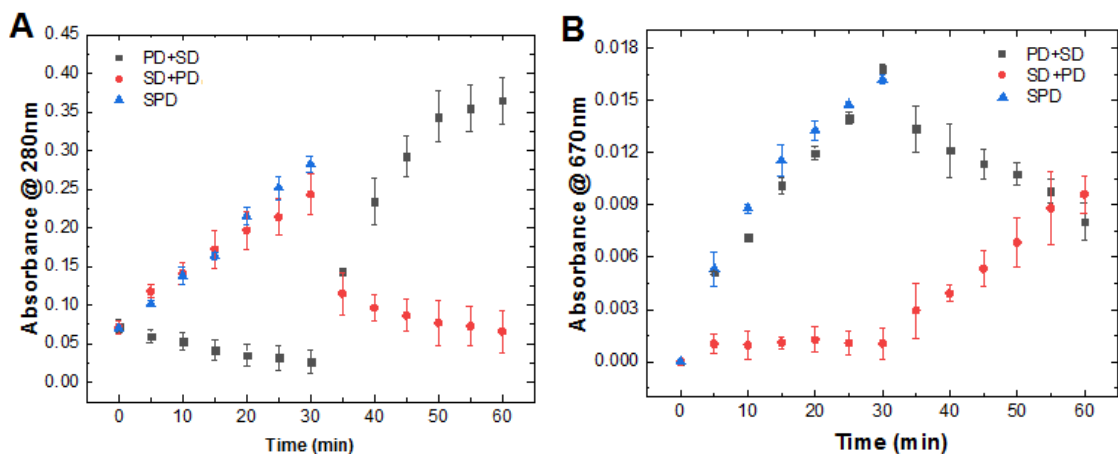
It was observed that the Sp were formed at approx. 280 nm band during the experiments based on the SD, SPD, SD+PD and PD+SD action. The Sp formed during the SD+PD action, suffered an interruption and high degradation by the light irradiation



**Figure 49** – The amount of decomposed PpIX moles by SD, PD, SPD, PD+SD and SD+PD action.

Source: By the author

during the last 30 min of exposure. While, the Sp grew continuously during SPD action (Figure 50-A). During the experiments based on the PD, SPD, SD+PD and PD+SD action, the Pp were formed at approx. 670 nm band. The Pp formed during the PD+SD action, suffered an interruption and partial degradation by the sonication during the last 30 min of exposure. While, the Pp grew continuously during SPD action (Figure 50-B).



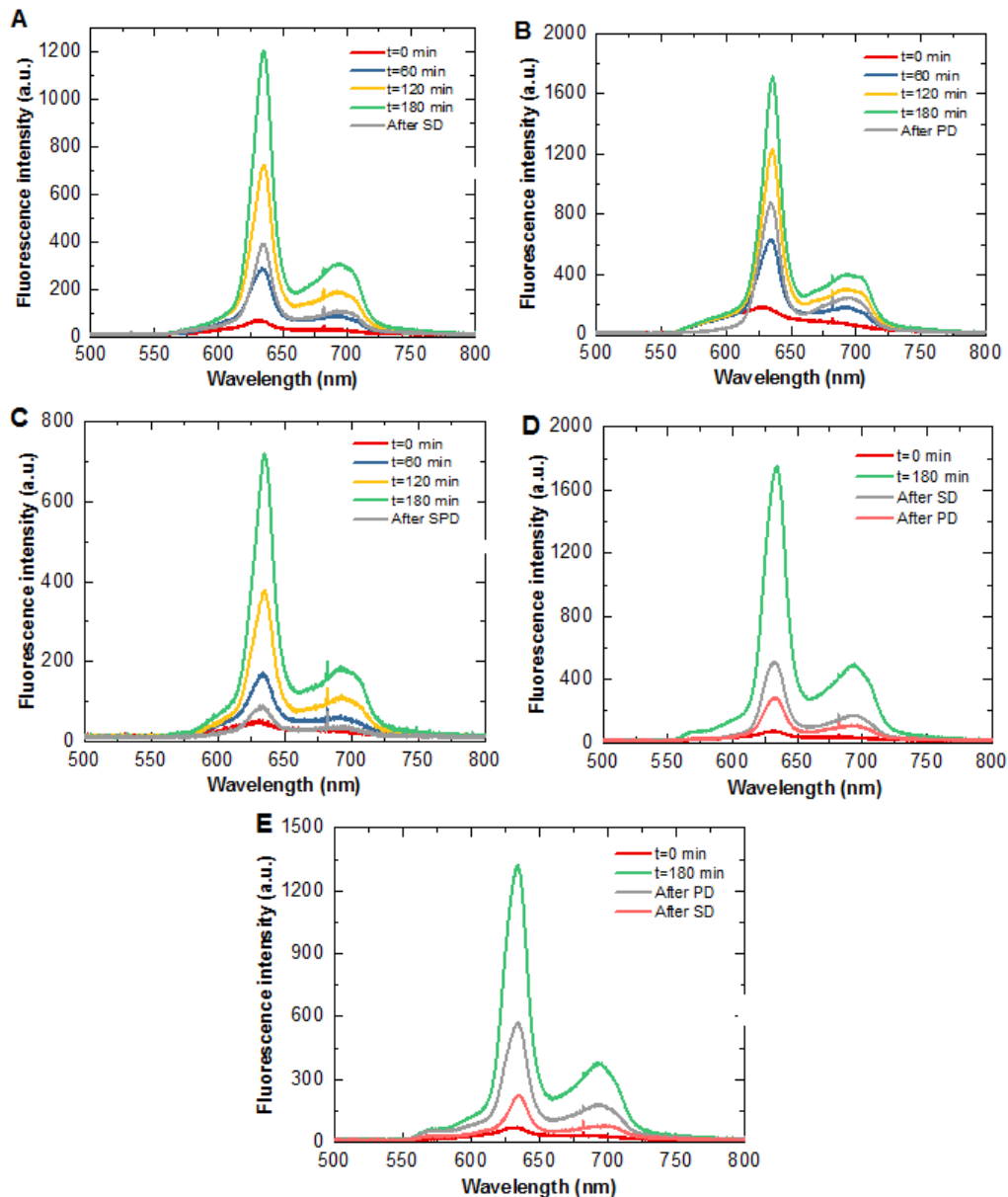
**Figure 50** – (A) The sonoproducts formation in 280nm band and (B) the photoproducts formation in 670nm band during PD+SD, SD+PD and SPD action.

Source: By the author

## 4.2 *In vivo* experiments

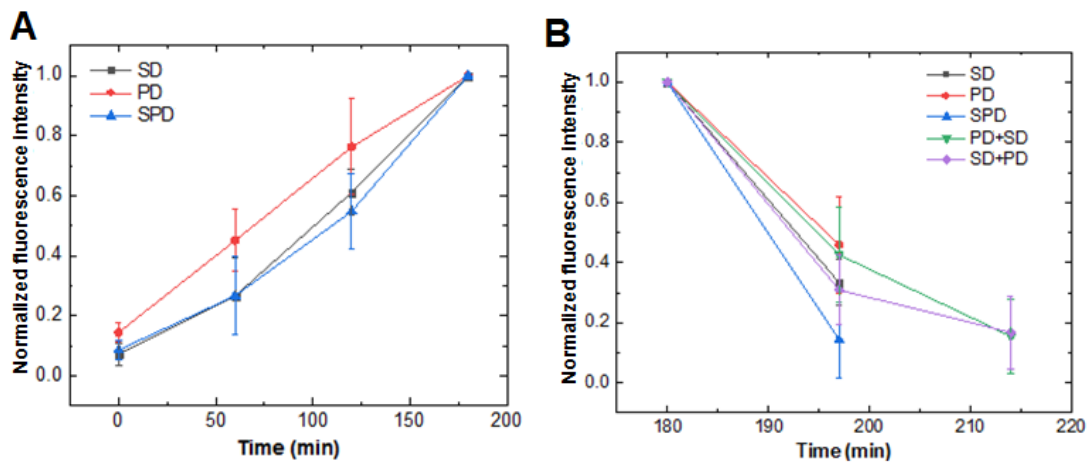
### 4.2.1 Fluorescence detection of PpIX in rat liver

In this study, 5-ALA was adopted as a sono-photosensitizer taking into account the reported antitumor effects, which were sonodynamically and photodynamically induced with the use of 5-ALA in animal model.<sup>85,86,99,100</sup> The mean fluorescence spectra not normalized (three different sites of the liver surface) are shown in Figure 51 and refers to measurements of one animal per group.



**Figure 51** – The not normalized fluorescence spectra recorded before ALA administration, during 3 hours of ALA accumulation, and immediately after (A) SD, (B) PD, (C) SPD, (D) SD+PD and (E) PD+SD action. Maximum fluorescence intensity was detected at 635 nm. Fluorescence emission was scanned from 500 to 800 nm.

Before ALA injection (red line), it was possible to observe the average spectrum of the liver's endogenous fluorescence with one band centered in 630 nm. After ALA injection, The ALA-induced PpIX-related fluorescence was characterized by a dual-peaked fluorescence at 635 nm and 690 nm, with the predominant band at 635 nm. Both peaks of fluorescence emission are clearly seen in all the spectra. Although the dose of ALA administered to each animal was the same, the fluorescence intensity after 3 hours varied from one animal to another. The spectra recorded at every hour clearly showed a continuous increase in fluorescence intensity of both peaks, evidencing the PpIX incorporation into the liver. In all the experiments, the fluorescence spectrum recorded after treatment showed a great decrease at the predominant fluorescence peak of PpIX (635nm), indicating a significant induced PpIX degradation (Figure 52).



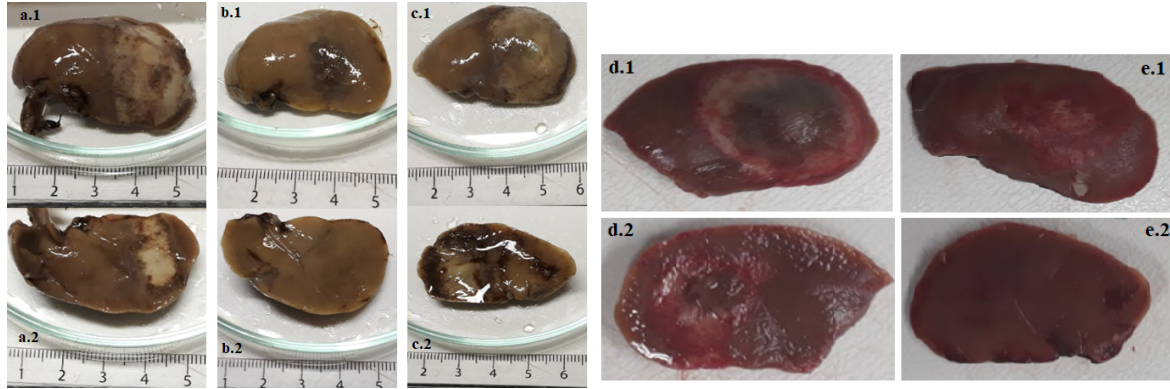
**Figure 52** – (A) Normalized fluorescence intensity at 630 nm band recorded at 0, 60, 120 and 180 min after ALA administration. (B) Normalized fluorescence intensity at 630 nm band recorded after treatment at 197 min (SD, PD and SPD action) and 214 min (PD+SD, SD+PD action). The symbols and error bars represent the mean experimental values and standard deviation, respectively.

Source: By the author

#### 4.2.2 Macroscopic observations.

The average temperature on the liver surface before treatment was  $30 \pm 2$  °C, and after irradiation under the establish parameters for each group, increased approx.  $4 \pm 1$  °C. As the temperature increase was not high, under the light and US intensity parameters we used, the heating effects, was not attributed to the rat liver necrosis induced by each action.<sup>101</sup>

After 30 h of treatment, the animals were sacrificed and livers were removed. The non-sensitized liver (control group) did not show signs of necrosis at any of the applied actions, while, all the sensitized livers presented a visible necrosis area on the liver surface, which had a circular shape in all groups (Figure 53). The sensitized liver exposed to the



**Figure 53** – Necrosis area: on the rat liver after 30 hours of apply the (a) SD, (b) PD, (c) SPD, (d) PD+SD and (e) SD+PD action. (1) Front side, (2) Reverse side.

Source: By the author

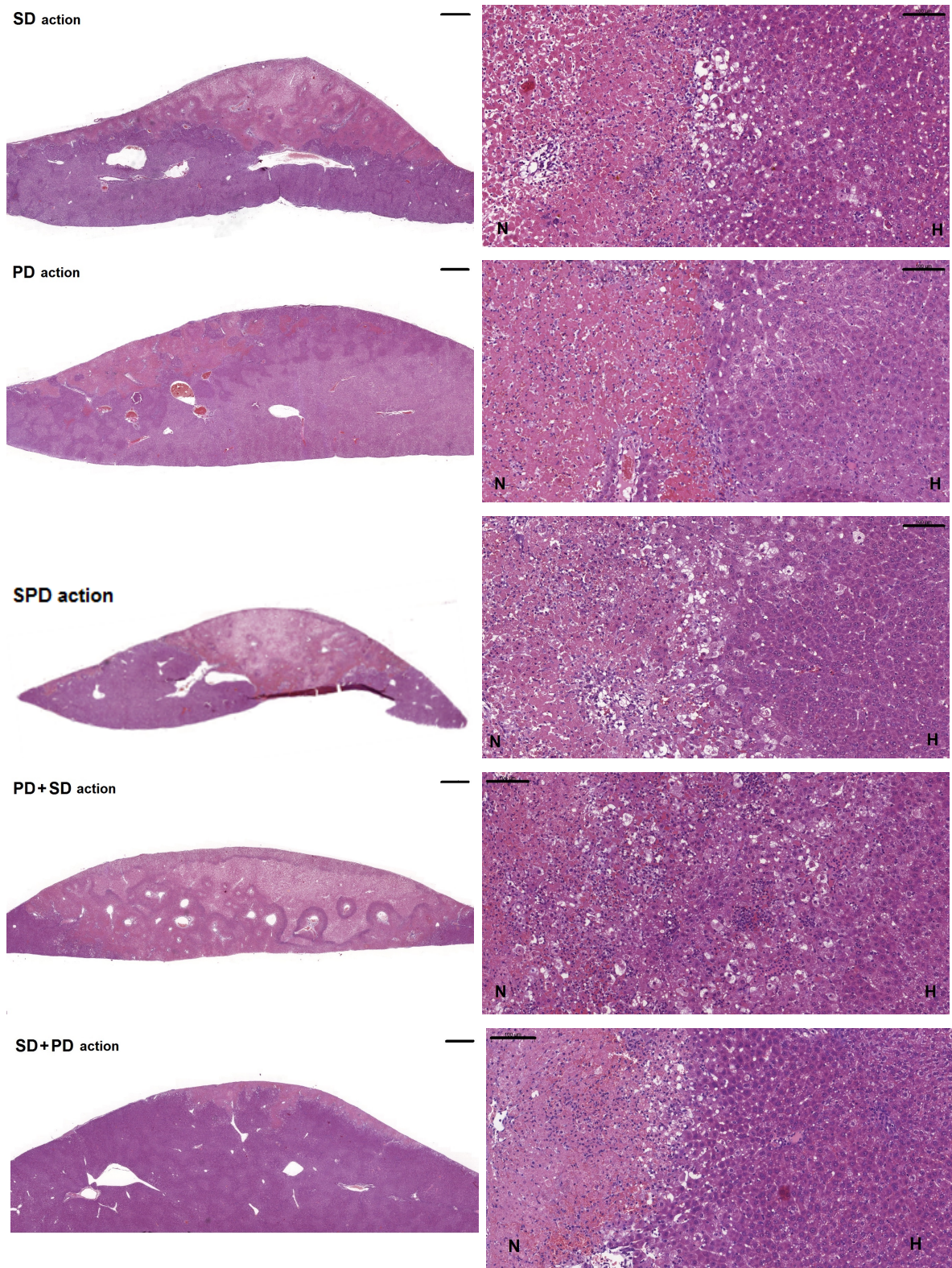
PD and SD+PD action showed a necrosis area corresponding to a disk slightly bigger than the illuminated effective area with a mean superficial width of necrosis of  $7 \pm 2$  mm. The sensitized liver exposed to the SD, SPD and PD+SD action showed a necrosis area slightly bigger than the effective area of the transducer, with a superficial width of necrosis of  $20 \pm 2$  mm. This could have happened due to the lateral diffusion of light and US reaching surface regions not directly illuminated. Observing the removed liver exposed to the SD action, it was perceived that the small surface region that remains below the laser output area (which was kept off during the treatment according to the protocol), also suffer a superficial damage. This may be because the diameter of the laser output in the middle of the transducer is small enough for the ultrasound waves to travel through this area, since the gel layer applied on the liver covers the exact region of contact with the transducer.

#### 4.2.3 Histological observations.

All the histological slides were classified into five groups according each action: SD, PD, SPD, SD+PD and PD+SD action.

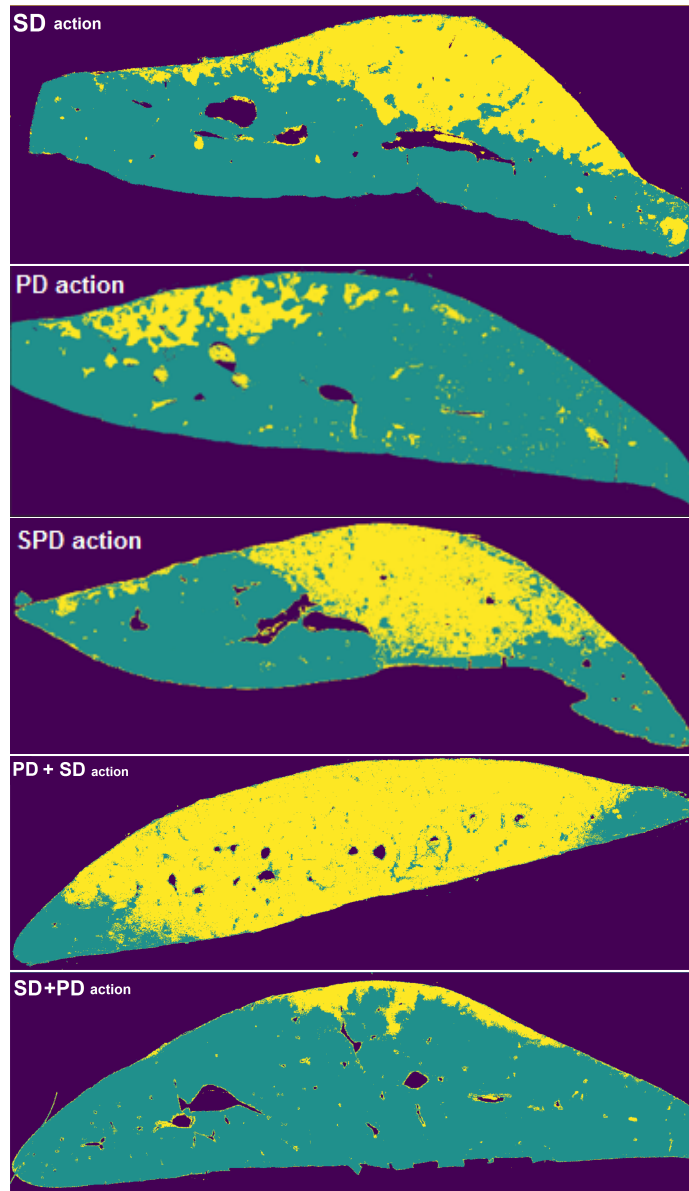
*Necrosis area measurement.* The figure 54 illustrates at left column, the scanned histological slides. This images were processed using a classification algorithm by the random forest method to differentiate the damaged tissue from the non-damaged as shown in Figure 55. The random forest method was implemented with 100 decision trees, trained with part of the image pixels, and used to classify all the image pixels. This process was repeated for each image. The three RGB (red, green, and blue) channels of each pixel was used as the input information to training the classifier. After that, the Random Forest sought to classify all the image pixels into three different classes (blank, non-damaged tissue, and damaged tissue), as well as measure each region in square pixels ( $px^2$ ) based on its RGB values.





**Figure 54** – Digitized histological slides of liver tissue: (left) the necrosis area and (right) the transition between necrotic (N) and healthy (H) tissue induced by each action. The bars in the left column represents 1000  $\mu\text{m}$  for SD and PD group; 2000  $\mu\text{m}$  for SPD group. The bars in the right column represents 100  $\mu\text{m}$ .

Source: By the author

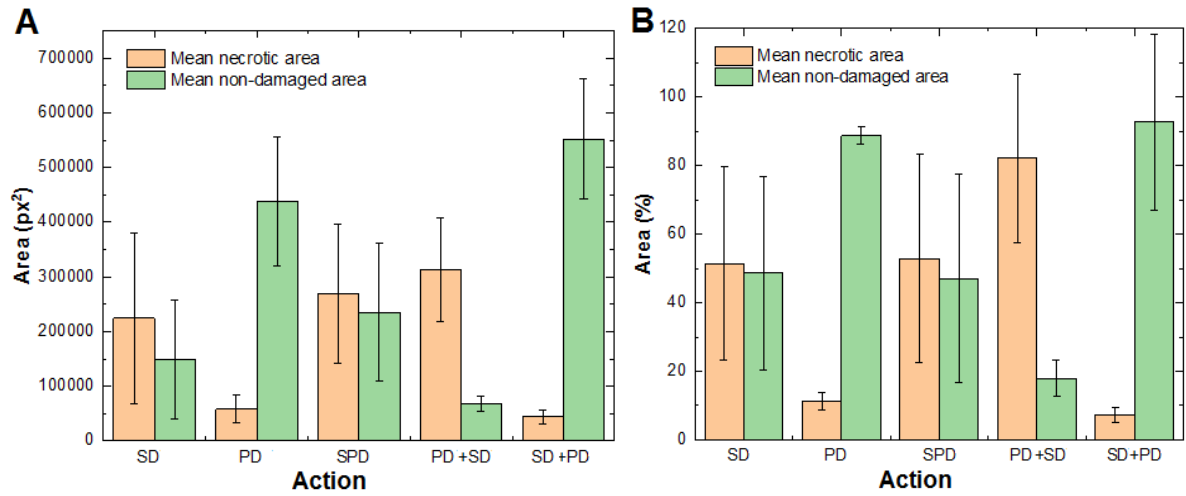


**Figure 55** – Image processing of the scanned histological slides by the random forest method, showing (yellow region) the necrotic and (green region) non-damaged tissue induced by each action.

Source: By the author

Under the US and light parameters used at *in vivo* experiments, the area of necrosis ( $A_{NEC}$ ) obtained by applying the SPD and PD+SD actions was much greater than under the PD action, evidencing that the scope of necroses area was improved by combining light irradiation with ultrasound, except for the SD+PD action (Figure 56). Comparing the necrosis area achieved applying SPD, SD+PD, PD+SD actions, we could see that despite delivering the same dose of light and ultrasound, the order in which each source was applied influenced in the necrosis area triggered by these actions. It was induced a great percentage of  $A_{NEC}$  under SD, SPD and PD+SD actions, however the  $A_{NEC}$  was visibly less under the SD+PD action than the previous two (Figure 56). These results

could be related to those obtained at *in vitro* procedures, since the PpIX decay rate values  $k$  obtained for SPDT and PDT+SDT groups were greater than SDT+PDT group.



**Figure 56** – Measurements of the mean damaged and non-damaged area obtained through image processing in (A) pixel squared and (B) percentage. Bars represent the SD.

Source: By the author

*Necrotic-healthy tissue transition.* The figure 54 (right column) illustrate sections of the sample corresponding to each action at 12x magnification, whereby it was possible to study the damaged tissue. It was observed coagulative necrosis, centrilobular vein necrosis and inflammatory regions induced by each action. In previous studies, where the necrosis in rat liver induced by PD action was analyzed, it was observed a well-defined transition line between necrotic and healthy tissue.<sup>90,92</sup> Unlike those observations, in this study, the transition between necrotic and healthy liver tissue induced by the PD action was not well-defined. This was thought to be due to the use of the acoustic gel on the surface of the liver in all experiments. Besides, It was perceived a great structural disorganization (small spaces) produced by the actions that involve ultrasound irradiation (e.g. SD, SPD, PD+SD and PD+SD action).



## 5 CONCLUSIONS

This study explored the association of the sonodynamic (SD) and the photodynamic (PD) action using Protoporphyrin IX as a sono-photosensitizer, aiming for a greater understanding of the mechanisms and effects of the combined action. In the first group of experiments of the *in vitro* stage, it was observed that PpIX can effectively be degraded by ultrasound irradiation with a first order mechanism in relation to the PpIX concentration. The sonobleaching rate of PpIX depends on the initial PpIX concentration, since the US-mediated PpIX degradation becomes more rapid as the initial PpIX concentration decreases. This result was shown to be the same by analyzing the absorption spectra of PpIX in any of the five absorption bands of PpIX. On the other hand, an absorption band growth occurs at 280 nm as a result of ultrasound irradiation, this Sp formation did not show a significant variation due to the change in the initial PpIX concentration of the solutions. In the second group of experiments, it was concluded that both sonobleaching and photobleaching of PpIX, likewise, the formation of sonoproducts at approx. 280 nm and photoproducts at approx. 670nm, have a direct relation with ultrasound and light intensity, respectively. Besides, the simultaneously ultrasound and light irradiation (SPD action) showed an additive PpIX decay rate: ( $k_{SPD} \simeq k_{SD} + k_{PD}$ ). Finally, the sonoluminescence phenomenon was not a predominant mechanism during the US-mediated PpIX degradation, since there was no formation of photoproducts which could evidence the generation of light flashes during sonification. Therefore, we assumed that the US-mediated PpIX degradation was predominantly through sonomechanical forces or the formation of reactive oxygen radicals. In the third experimental group, where the combination of ultrasound and light irradiation was applied simultaneously (SPD action), and one followed by another (SD+PD, PD+SD action), it was found that a greater PpIX degradation can be obtained by the PD+SD, SD+PD and SPD action, than by the SD or PD action. Although the SD+PD and PD+SD actions induced a slightly higher PpIX degradation than SPD action, the PpIX decay rate obtained under the SPD action was higher than the other two combined actions. This is because the irradiation time for the SPD action is half the total irradiation time under the PD+SD and SD+PD action.

For the *in vivo* stage, it was possible to develop a sono-photodynamic equipment to irradiate the organ of the animal with light and ultrasound simultaneously, modulating the intensity of each source according to the desired one. Through this equipment, we were able to induce a PD, SD and combined action (SPD, PD+SD and SD+PD action) using a single probe.

The scanned histological slides, let us observe that it was possible to induce a greater percentage of the necrosis area (longitudinal section of the liver) by the combined

action than only PD action. Also, the order in which the sensitized organ is irradiated, influences the degradation of protoporphyrin (PpIX), since applying light irradiation following ultrasound irradiation (SD+PD action), did not induce as much necrosis in the rat liver as applying the other action using both sources (SPD, PDT+SD). This finding was not explored in this work, but it certainly must be more widely studied. On histological appearance, it was observed coagulative necrosis, centrilobular vein necrosis and inflammatory regions induced by each action. The transition between the necrotic and healthy tissue was not well-defined in any of the experimental groups. Besides, the transition necrotic-healthy tissue presented a great structural disorganization produced by the actions that involve ultrasound irradiation (e.g. SD, SPD, PD+SD and PD+SD action).

These results support that the combined action could improve the drug decay rate, as well as having a greater scope than either PD or SD action, so it is worthy of further investigation to get a successful application at wide variety of tumors.

## REFERENCES

- 1 ALLISON, R. R. *et al.* Photosensitizers in clinical pdt. **Photodiagnosis and Photodynamic Therapy**, v. 1, n. 1, p. 27 – 42, 2004. DOI:[10.1016/S1572-1000\(04\)00007-9](https://doi.org/10.1016/S1572-1000(04)00007-9).
- 2 BAGNATO, V. S. *et al.* Photodynamic reactions: cancer and microbiological control. In: ROBERTIS, E. D. (Ed.). **Proceedings of the Workshop on Cell biology and genetics**. Vatican: Pontifical Academy of Sciences, 2018. p. 247–268.
- 3 INSTITUTE, N. C. **Estimativa 2020: incidência de câncer no Brasil**. Disponível em: <<https://www.inca.gov.br/sites/ufu.sti.inca.local/files//media/document/estimativa-2020-incidencia-de-cancer-no-brasil.pdf>>.
- 4 BORISSEVITCH, I.; FERREIRA, L. **A luz na medicina moderna: fotoquimioterapia**. São Paulo: Livraria da Física, 2016. 76 p.
- 5 WAN, M.; LIN, J. Current evidence and applications of photodynamic therapy in dermatology. **Clinical, Cosmetic and Investigational Dermatology**, v. 7, p. 145–163, 2014. DOI:[10.2147/CCID.S35334](https://doi.org/10.2147/CCID.S35334).
- 6 BAGNATO, V. **Terapia fotodinâmica dermatológica: programa TFD Brasil**. São Carlos: Compacta, 2015. 239 p.
- 7 MARTELLI, F. *et al.* **Light propagation through biological tissue and other diffusive media: theory, solutions, and software**. Washington: SPIE Ppublications, 2010. 298 p.
- 8 AGOSTINIS, P. *et al.* Photodynamic therapy of cancer: an update. **CA: a cancer journal for clinicians**, v. 61, n. 4, p. 250–281, 2011. DOI:[10.3322/caac.20114](https://doi.org/10.3322/caac.20114).
- 9 GERALDE, M. C. *et al.* Photodynamic reactions for the treatment of oral-facial lesions and microbiological control. In: STÜBINGER, S. *et al.* (Ed.). **Lasers in oral and maxillofacial surgery**. Cham: Springer International Publishing, 2020. p. 45–57.
- 10 YASUI, K. **Acoustic cavitation and bubble dynamics**. Berlin: Springer, 2018.
- 11 RENGENG, L. *et al.* Sonodynamic therapy, a treatment developing from photodynamic therapy. **Photodiagnosis and Photodynamic Therapy**, v. 19, p. 159–166, 2017. DOI:[10.1016/j.pdpdt.2017.06.003](https://doi.org/10.1016/j.pdpdt.2017.06.003).
- 12 CHOI, V. *et al.* Activating drugs with sound: Mechanisms behind sonodynamic therapy and the role of nanomedicine. **Bioconjugate Chemistry**, v. 31, n. 4, p. 967–989, 2020. DOI:[10.1021/acs.bioconjchem.0c00029](https://doi.org/10.1021/acs.bioconjchem.0c00029).
- 13 RAJORA, M. *et al.* Advancing porphyrin’s biomedical utility via supramolecular chemistry. **Chemical Society Reviews**, v. 46, n. 21, p. 6433–6469, 2017. DOI:[10.1039/c7cs00525c](https://doi.org/10.1039/c7cs00525c).
- 14 PUTTERMAN, S. J.; WENINGER, K. R. Sonoluminescence: how bubbles turn sound into light. **Annual Review of Fluid Mechanics**, v. 32, n. 1, p. 445–476, 2000. DOI:[10.1146/annurev.fluid.32.1.445](https://doi.org/10.1146/annurev.fluid.32.1.445).

- 15 UMEMURA, S.-i. *et al.* Mechanism of cell damage by ultrasound in combination with hematoporphyrin. **Japanese Journal of Cancer Research**, v. 81, n. 9, p. 962–966, 1990. DOI:[10.1111/j.1349-7006.1990.tb02674.x](https://doi.org/10.1111/j.1349-7006.1990.tb02674.x).
- 16 ROSENTHAL, I. *et al.* Sonodynamic therapy—a review of the synergistic effects of drugs and ultrasound. **Ultrasonics Sonochemistry**, v. 11, n. 6, p. 349–363, 2004. DOI:[10.1016/j.ultsonch.2004.03.004](https://doi.org/10.1016/j.ultsonch.2004.03.004).
- 17 FLANNIGAN, D.; SUSLICK, K. Plasma formation and temperature measurement during single-bubble cavitation. **Nature**, v. 434, p. 52–55, 2005. DOI:[10.1038/nature03361](https://doi.org/10.1038/nature03361).
- 18 HAOBO, X. *et al.* The decomposition of protoporphyrin ix by ultrasound is dependent on the generation of hydroxyl radicals. **Ultrasonics Sonochemistry**, v. 27, p. 623–630, 2015. DOI:[10.1016/j.ultsonch.2015.04.024](https://doi.org/10.1016/j.ultsonch.2015.04.024).
- 19 GIUNTINI, F. *et al.* Insight into ultrasound-mediated reactive oxygen species generation by various metal-porphyrin complexes. **Free Radical Biology and Medicine**, v. 121, p. 190–201, 2018. DOI:[10.1016/j.freeradbiomed.2018.05.002](https://doi.org/10.1016/j.freeradbiomed.2018.05.002).
- 20 REQUENA, M. B. *et al.* Use of dermograph for improvement of ppix precursor's delivery in photodynamic therapy: experimental and clinical pilot studies. **Photodiagnosis and Photodynamic Therapy**, v. 29, p. 101599, 2020. DOI:[10.1016/j.pdpdt.2019.101599](https://doi.org/10.1016/j.pdpdt.2019.101599).
- 21 LIU, Y. *et al.* Sinoporphyrin sodium triggered sono-photodynamic effects on breast cancer both in vitro and in vivo. **Ultrasonics Sonochemistry**, v. 31, p. 437–448, 2016. DOI:[10.1016/j.ultsonch.2016.01.038](https://doi.org/10.1016/j.ultsonch.2016.01.038).
- 22 JIN, Z. *et al.* Combination effect of photodynamic and sonodynamic therapy on experimental skin squamous cell carcinoma in c3h/hen mice. **The Journal of Dermatology**, v. 27, p. 294–306, 2000. DOI:[10.1111/j.1346-8138.2000.tb02171.x](https://doi.org/10.1111/j.1346-8138.2000.tb02171.x).
- 23 WANG, X. *et al.* Sonodynamic and photodynamic therapy in advanced breast carcinoma: A report of 3 cases. **Integrative Cancer Therapies**, v. 8, n. 3, p. 283–287, 2009. DOI:[10.1177/1534735409343693](https://doi.org/10.1177/1534735409343693).
- 24 KENYON, N. *et al.* Activated cancer therapy using light and ultrasound - a case series of sonodynamic photodynamic therapy in 115 patients over a 4 year period. **Current Drug Therapy**, v. 4, p. 179–193, 2009. DOI:[10.2174/157488509789055036](https://doi.org/10.2174/157488509789055036).
- 25 NORMAN, J.; FULLER, R. Outcome measures following sonodynamic photodynamic therapy – a case series. **Current Drug Therapy**, v. 6, n. 1, p. 12–16, 2011. DOI:[10.2174/157488511794079059](https://doi.org/10.2174/157488511794079059).
- 26 LI, L. Q. *et al.* Primary clinical use of the sono-photo-dynamic therapy for advanced esophagocadiac and gastric adenocarcinoma. **Journal of Clinical Oncology**, v. 32, n. 15\_suppl, p. e15024–e15024, 2014. DOI:[10.1200/jco.2014.32.15\\_suppl.e15024](https://doi.org/10.1200/jco.2014.32.15_suppl.e15024).
- 27 XU, J. *et al.* Combination of photodynamic therapy with radiotherapy for cancer treatment. **Journal of Nanomaterials**, v. 2016, p. 1–7, 01 2016. DOI:[10.1155/2016/8507924](https://doi.org/10.1155/2016/8507924).
- 28 GWYNNE, P.; GALLAGHER, M. Light as a broad-spectrum antimicrobial. **Frontiers in Microbiology**, v. 9, 02 2018. DOI:[10.3389/fmicb.2018.00119](https://doi.org/10.3389/fmicb.2018.00119).



- 
- 29 JACQUES, S. L. Optical properties of biological tissues: a review. **Physics in Medicine and Biology**, v. 58, n. 11, p. 37–61, 2013. DOI:[10.1088/0031-9155/58/11/R37](https://doi.org/10.1088/0031-9155/58/11/R37).
- 30 PLAETZER, K. *et al.* Photophysics and photochemistry of photodynamic therapy: fundamental aspects. **Lasers in Medical Science**, v. 24, n. 2, p. 259–268, 2009. DOI:[10.1007/s10103-008-0539-1](https://doi.org/10.1007/s10103-008-0539-1).
- 31 TUCHIN, V. V. Tissue optics and photonics: biological tissue structures. **Journal of Biomedical Photonics & Engineering**, v. 1, n. 1, 2015. DOI:[10.18287/jbpe-2015-1-1-3](https://doi.org/10.18287/jbpe-2015-1-1-3).
- 32 TUCHIN, V. V. Tissue optics and photonics: light-tissue interaction. **Journal of Biomedical Photonics & Engineering**, v. 1, n. 2, p. 98–134, 2015. DOI:[10.18287/JBPE16.02.030201](https://doi.org/10.18287/JBPE16.02.030201).
- 33 TUCHIN, V. V. Light interaction with biological tissues: overview. In: NOSSAL, R. J. *et al.* (Ed.). **Static and dynamic light scattering in medicine and biology**. CA, United States: SPIE, 1993. v. 1884, p. 234–272. DOI:[10.1117/12.148348](https://doi.org/10.1117/12.148348).
- 34 GOLDMAN, L. Chromophores in tissue for laser medicine and laser surgery. **Lasers in Medical Science**, v. 5, p. 289 – 292, 1990. DOI:[10.1007/BF02032656](https://doi.org/10.1007/BF02032656).
- 35 BASHKATOV, A. N. *et al.* Optical properties of skin, subcutaneous, and muscle tissues: a review. **Journal of Innovative Optical Health Sciences**, v. 04, n. 01, p. 9–38, 2011. DOI:[10.1142/S1793545811001319](https://doi.org/10.1142/S1793545811001319).
- 36 LYONS, S. *et al.* Imaging mouse cancer models in vivo using reporter transgenes. **Cold Spring Harbor Protocols**, v. 2013, 08 2013. DOI:[10.1101/pdb.top069864](https://doi.org/10.1101/pdb.top069864).
- 37 BAGNATO. **Novas técnicas ópticas para as áreas da saúde**. São Paulo: Livraria da Física, 2008. 239 p.
- 38 BOCK, G. R.; HARNETT, S. **Photosensitizing compounds: their chemistry, biology and clinical use**. New York: John Wiley & Sons, 2008.
- 39 WILSON, B.; PATTERSON, M. The physics, biophysics and technology of photodynamic therapy. **Physics in Medicine and Biology**, v. 53, p. 61–109, 2008. DOI:[10.1088/0031-9155/53/9/R01](https://doi.org/10.1088/0031-9155/53/9/R01).
- 40 GRECCO, C. *et al.* Single led-based device to perform widefield fluorescence imaging and photodynamic therapy. **Biophotonics South America**, v. 9531, p. 953121, 2015. DOI:[10.1117/12.2185925](https://doi.org/10.1117/12.2185925).
- 41 SÁNCHEZ, V. *et al.* Physiological considerations acting on triplet oxygen for explicit dosimetry in photodynamic therapy. **Photodiagnosis Photodynamic Therapy**, v. 19, p. 298–303, 2017. DOI:[10.1016/j.pdpdt.2017.07.008](https://doi.org/10.1016/j.pdpdt.2017.07.008).
- 42 HENDERSON, B. W.; DOUGHERTY, T. J. How does photodynamic therapy work? **Photochemistry and Photobiology**, v. 55, p. 145–157, 1992. DOI:[10.1111/j.1751-1097.1992.tb04222.x](https://doi.org/10.1111/j.1751-1097.1992.tb04222.x).
- 43 BAPTISTA, M. *et al.* Type I and type II photosensitized oxidation reactions: guidelines and mechanistic pathways. **Photochemistry and Photobiology**, v. 93, n. 4, p. 912–919, 2017. DOI:[10.1111/php.12716](https://doi.org/10.1111/php.12716).

- 44 NIEMZ, M. M. **Laser-tissue interactions: fundamentals and applications**. New York: Springer Science & Business Media, 2014. 307 p.
- 45 YAROSLAVSKY, A. *et al.* Cell death pathways in photodynamic therapy of cancer. **Cancers (Basel)**, v. 3, n. 2, p. 2516–2539, 2011. DOI:[10.3390/cancers3022516](https://doi.org/10.3390/cancers3022516).
- 46 BUYTAERT, E. *et al.* Molecular effectors of multiple cell death pathways initiated by photodynamic therapy. **Biochimica et Biophysica Acta**, v. 1776, n. 1, p. 86–107, 2007. DOI:[10.1016/j.bbcan.2007.07.001](https://doi.org/10.1016/j.bbcan.2007.07.001).
- 47 SCHULZE-OSTHOFF, K. How cells die: apoptosis and other cell death pathways. In: RODE, H. (Ed.). **Apoptosis, cytotoxicity and cell proliferation**. Mannheim, Germany: Roche Diagnostics GmbH, 2008. v. 4, p. 178.
- 48 EDINGER, A. L.; THOMPSON, C. B. Death by design: apoptosis, necrosis and autophagy. **Current Opinion in Cell Biology**, v. 16, n. 6, p. 663–669, 2004. DOI:[10.1016/j.ceb.2004.09.011](https://doi.org/10.1016/j.ceb.2004.09.011).
- 49 WAN, G.-Y. *et al.* Recent advances of sonodynamic therapy in cancer treatment. **Cancer Biology & Medicine**, v. 13, n. 3, p. 325, 2016. DOI:[10.20892/j.issn.2095-3941.2016.0068](https://doi.org/10.20892/j.issn.2095-3941.2016.0068).
- 50 CANAVESE, G. *et al.* Nanoparticle-assisted ultrasound: a special focus on sonodynamic therapy against cancer. **Chemical Engineering Journal**, v. 340, p. 155–172, 2018. DOI:[10.1016/j.cej.2018.01.060](https://doi.org/10.1016/j.cej.2018.01.060).
- 51 MASON, T. J.; PETERS, D. **Practical sonochemistry**. New York: Elsevier, 1991.
- 52 O'BRIEN, W. D. Ultrasound–biophysics mechanisms. **Progress in Biophysics and Molecular Biology**, v. 93, n. 1-3, p. 212–255, 2007. DOI:[10.1016/j.pbiomolbio.2006.07.010](https://doi.org/10.1016/j.pbiomolbio.2006.07.010).
- 53 ZISKIN, M. C. Fundamental physics of ultrasound and its propagation in tissue. **Radiographics**, v. 13, n. 3, p. 705–709, 1993. DOI:[10.1148/radiographics.13.3.8316679](https://doi.org/10.1148/radiographics.13.3.8316679).
- 54 BOUAKAZ, A.; ESCOFFRE, J.-M. **Therapeutic ultrasound**. Switzerland: Springer, 2016. 465 p.
- 55 ADEWUYI, Y. G. Sonochemistry: environmental science and engineering applications. **Industrial & Engineering Chemistry Research**, v. 40, n. 22, p. 4681–4715, 2001. DOI:[10.1021/ie010096l](https://doi.org/10.1021/ie010096l).
- 56 SUSLICK, K. S. **Ultrasound: its chemical, physical, and biological effects**. New Jersey: VCH Publishers, 1988.
- 57 CRUM, L. A. *et al.* **Sonochemistry and sonoluminescence**. Berlin: Springer Science & Business Media, 1998.
- 58 CHURCH, C. C. *et al.* A theoretical study of inertial cavitation from acoustic radiation force impulse imaging and implications for the mechanical index. **Ultrasound in Medicine & Biology**, v. 41, n. 2, p. 472–485, 2015. DOI:[10.1016/j.ultrasmedbio.2014.09.012](https://doi.org/10.1016/j.ultrasmedbio.2014.09.012).

- 
- 59 SUSLICK, K. S. The chemical effects of ultrasound. **Scientific American**, v. 260, n. 2, p. 80–87, 1989. DOI:[10.2307/24987145](https://doi.org/10.2307/24987145).
- 60 SUSLICK, K. S. *et al.* Sonochemical hot spot. **Journal of the American Chemical Society**, v. 108, n. 18, p. 5641–5642, 1986. DOI:[10.1021/ja00278a0557](https://doi.org/10.1021/ja00278a0557).
- 61 FLINT, E. B.; SUSLICK, K. S. The temperature of cavitation. **Science**, v. 253, n. 5026, p. 1397–1399, 1991. DOI:[10.1126/science.253.5026.1397](https://doi.org/10.1126/science.253.5026.1397).
- 62 MAKINO, K. *et al.* Chemical effects of ultrasound on aqueous solutions. formation of hydroxyl radicals and hydrogen atoms. **The Journal of Physical Chemistry**, v. 87, n. 8, p. 1369–1377, 1983.
- 63 RIESZ, P. *et al.* Free radical generation by ultrasound in aqueous and nonaqueous solutions. **Environmental Health Perspectives**, v. 64, p. 233–252, 1985. DOI:[10.1289/ehp.8564233](https://doi.org/10.1289/ehp.8564233).
- 64 CRUM, L. A.; ROY, R. A. Sonoluminescence. **Science**, v. 266, n. 5183, p. 233–234, 1994. DOI:[10.1126/science.266.5183.233](https://doi.org/10.1126/science.266.5183.233).
- 65 BYUN, K.-T. *et al.* Sonoluminescence characteristics from micron and submicron bubbles. **Journal of the Korean Physical Society**, v. 47, p. 1010–1022, 12 2005.
- 66 SUSLICK, K. S.; FLANNIGAN, D. J. Inside a collapsing bubble: sonoluminescence and the conditions during cavitation. **Annual Review of Physical Chemistry**, v. 59, n. 1, p. 659–683, 2008. DOI:[10.1146/annurev.physchem.59.032607.093739](https://doi.org/10.1146/annurev.physchem.59.032607.093739).
- 67 NEPPIRAS, E. A. Acoustic cavitation. **Physics Reports**, v. 61, n. 3, p. 159–251, 1980. DOI:[10.1016/0370-1573\(80\)90115-5](https://doi.org/10.1016/0370-1573(80)90115-5).
- 68 NOLTINGK, B. E.; NEPPIRAS, E. A. Cavitation produced by ultrasonics. **Proceedings of the Physical Society. Section B**, v. 63, n. 9, p. 674, 1950. DOI:[10.1088/0370-1301/63/9/305](https://doi.org/10.1088/0370-1301/63/9/305).
- 69 HILL, C. R. *et al.* **Physical principles of medical ultrasonics**. England: Acoustical Society of America, 2004. 497 p.
- 70 OTTO, C. M. **Textbook of clinical echocardiography E-Book**. New York: Elsevier Health Sciences, 2013.
- 71 CARSTENSEN, E. Interaction of ultrasound with tissues. In: WHITE, D.; BARNES, R. (Ed.). **Ultrasound in medicine**. Boston: Springer, 1976. p. 517–517. DOI:[10.1007/978-1-4613-4307-3\\_125](https://doi.org/10.1007/978-1-4613-4307-3_125).
- 72 STARKEY, C. **Therapeutic modalities**. [S.l.]: FA Davis, 2013.
- 73 YUMITA, N. *et al.* Synergistic effect of ultrasound and hematoporphyrin on sarcoma 180. **Japanese Journal of Cancer Research**, v. 81, n. 3, p. 304–308, 1990. DOI:[10.1111/j.1349-7006.1990.tb02565.x](https://doi.org/10.1111/j.1349-7006.1990.tb02565.x).
- 74 OSAKI, T. *et al.* Sonodynamic therapy using 5-aminolevulinic acid enhances the efficacy of bleomycin. **Ultrasonics**, v. 67, p. 76–84, 2016. DOI:[10.1016/j.ultras.2016.01.003](https://doi.org/10.1016/j.ultras.2016.01.003).

- 75 CHEN, H. *et al.* Recent progress in development of new sonosensitizers for sonodynamic cancer therapy. **Drug Discovery Today**, v. 19, n. 4, p. 502–509, 2014. DOI:[10.1016/j.drudis.2014.01.010](https://doi.org/10.1016/j.drudis.2014.01.010).
- 76 BRAULT, D. Physical chemistry of porphyrins and their interactions with membranes: the importance of ph. **Journal of Photochemistry and Photobiology B**, v. 6, n. 1-2, p. 79–86, 1990. DOI:[10.1016/1011-1344\(90\)85076-9](https://doi.org/10.1016/1011-1344(90)85076-9).
- 77 YUMITA, N. *et al.* Sonodynamically-induced apoptosis, necrosis, and active oxygen generation by mono-l-aspartyl chlorin e6. **Cancer Science**, v. 99, n. 1, p. 166–172, 2008. DOI:[10.1111/j.1349-7006.2007.00653.x](https://doi.org/10.1111/j.1349-7006.2007.00653.x).
- 78 SONG, W. *et al.* Apoptosis of sas cells induced by sonodynamic therapy using 5-aminolevulinic acid sonosensitizer. **Anticancer Research**, v. 31, n. 1, p. 39–45, 2011.
- 79 LI, Y. *et al.* Apoptosis induced by sonodynamic treatment by protoporphyrin ix on mda-mb-231 cells. **Ultrasonics**, v. 52, n. 4, p. 490–496, 2012. DOI:[10.1016/j.ultras.2011.10.013](https://doi.org/10.1016/j.ultras.2011.10.013).
- 80 WANG, X. *et al.* The tumoricidal effect of sonodynamic therapy (sdt) on s-180 sarcoma in mice. **Integrative Cancer Therapies**, v. 7, n. 2, p. 96–102, 2008. DOI:[10.1177/1534735408319065](https://doi.org/10.1177/1534735408319065).
- 81 Y, L. *et al.* Low-intensity ultrasound combined with 5-aminolevulinic acid administration in the treatment of human tongue squamous carcinoma. **Cellular Physiology & Biochemistry**, v. 30, p. 321–333, 2012. DOI:[10.1159/000339067](https://doi.org/10.1159/000339067).
- 82 VALENTINE, R. M. *et al.* Modelling fluorescence in clinical photodynamic therapy. **Photochemical & Photobiological Sciences**, v. 12, n. 1, p. 203–213, 2013. DOI:[10.1039/C2PP25271F](https://doi.org/10.1039/C2PP25271F).
- 83 KENNEDY, J. *et al.* Photodynamic therapy with endogenous protoporphyrin ix: basic principles and present clinical experience. **Journal of Photochemistry and Photobiology B**, v. 6, n. 1-2, p. 143–148, 1990. DOI:[10.1016/1011-1344\(90\)85083-9](https://doi.org/10.1016/1011-1344(90)85083-9).
- 84 BAGDONAS, S. *et al.* Phototransformations of 5-aminolevulinic acid-induced protoporphyrin IX in vitro: a spectroscopic study. **Photochemistry and Photobiology**, v. 72, n. 2, p. 186–192, 2000. DOI:[10.1562/0031-8655\(2000\)0720186POAAIP2.0.CO2](https://doi.org/10.1562/0031-8655(2000)0720186POAAIP2.0.CO2).
- 85 OTAKE, M. *et al.* Selective accumulation of ala-induced ppix and photodynamic effect in chemically induced hepatocellular carcinoma. **Laser Physics Letters**, v. 89, n. 6, p. 730–736, 2003. DOI:[10.1002/lapl.200710014](https://doi.org/10.1002/lapl.200710014).
- 86 SVANBERG, K. *et al.* Photodynamic therapy using intravenous  $\delta$ -aminolaevulinic acid-induced protoporphyrin ix sensitisation in experimental hepatic tumours in rats. **British Journal of Cancer**, v. 74, n. 10, p. 1526–1533, 1996. DOI:[10.1038/bjc.1996.584](https://doi.org/10.1038/bjc.1996.584).
- 87 GUDGIN, E.; POTTIER, R. On the role of protoporphyrin IX photoproducts in photodynamic therapy. **Journal of Photochemistry and Photobiology B**, v. 29, p. 91–93, 1995. DOI:[10.1016/1011-1344\(95\)90267-8](https://doi.org/10.1016/1011-1344(95)90267-8).
- 88 MA, L. *et al.* The photosensitizing effect of the photoproduct of protoporphyrin IX. **Journal of Photochemistry and Photobiology B**, v. 60, n. 2, p. 108–113, 2001. DOI:[10.1016/s1011-1344\(01\)00133-6](https://doi.org/10.1016/s1011-1344(01)00133-6).

- 
- 89 CAMPOS, C. de P. *et al.* Fluorescence spectroscopy in the visible range for the assessment of uvb radiation effects in hairless mice skin. **Photodiagnosis and Photodynamic Therapy**, v. 20, p. 21 – 27, 2017. DOI:[10.1016/j.pdpdt.2017.08.016](https://doi.org/10.1016/j.pdpdt.2017.08.016).
- 90 FERREIRA-STRIXINO, J. *et al.* Necrosis characteristics of photodynamic therapy in normal rat liver. **Laser Physics**, v. 2, p. 209–212, 2003.
- 91 FERREIRA, J. *et al.* Experimental determination of threshold dose in photodynamic therapy in normal rat liver. **Laser Physics Letters**, v. 4, n. 6, p. 469, 2007. DOI:[10.1002/lapl.200710014](https://doi.org/10.1002/lapl.200710014).
- 92 FERRAZ, R. *et al.* Determination of threshold dose of photodynamic therapy to measure superficial necrosis. **Photomedicine and Laser Surgery**, v. 27, p. 93–9, 03 2009. DOI:[10.1089/pho.2007.2207](https://doi.org/10.1089/pho.2007.2207).
- 93 HO, T. K. Random decision forests. In: INTERNATIONAL CONFERENCE ON DOCUMENT ANALYSIS AND RECOGNITION. **Proceedings of 3rd International conference on document analysis and recognition**. Montreal: IEEE, 1995. v. 1, p. 278–282. DOI:[10.1109/ICDAR.1995.598994](https://doi.org/10.1109/ICDAR.1995.598994).
- 94 SEE, J.-A. *et al.* Consensus recommendations on the use of daylight photodynamic therapy with methyl aminolevulinic acid cream for actinic keratoses in Australia. **Australasian Journal of Dermatology**, Wiley Online Library, v. 57, n. 3, p. 167–174, 2016. DOI:[10.1111/ajd.12354](https://doi.org/10.1111/ajd.12354).
- 95 YANG, Y.-T. *et al.* Absorption and fluorescence spectral properties of hematoporphyrin in liposomes, micelles, and nanoparticles. **Dyes and Pigments**, v. 96, n. 3, p. 763 – 769, 2013. DOI:[10.1016/j.dyepig.2012.09.014](https://doi.org/10.1016/j.dyepig.2012.09.014).
- 96 KIDA, M. *et al.* Sonochemical formation of hydrogen peroxide. 2017. DOI:[10.3390/ecws-2-04957](https://doi.org/10.3390/ecws-2-04957).
- 97 WEISSLER, A. Formation of hydrogen peroxide by ultrasonic waves: free radicals. **Journal of the American Chemical Society**, v. 81, n. 5, p. 1077–1081, 1959. DOI:[10.1021/ja01514a015](https://doi.org/10.1021/ja01514a015).
- 98 BRANCALEON, L. *et al.* Characterization of the photoproducts of protoporphyrin IX bound to human serum albumin and immunoglobulin G. **Biophysical Chemistry**, v. 109, p. 351–360, 2004. DOI:[10.1016/j.bpc.2003.12.008](https://doi.org/10.1016/j.bpc.2003.12.008).
- 99 JEONG, E.-J. *et al.* Sonodynamically induced antitumor effects of 5-aminolevulinic acid and fractionated ultrasound irradiation in an orthotopic rat glioma model. **Ultrasound in Medicine & Biology**, v. 38, n. 12, p. 2143 – 2150, 2012. DOI:[10.1016/j.ultrasmedbio.2012.07.026](https://doi.org/10.1016/j.ultrasmedbio.2012.07.026).
- 100 WU, S.-K. *et al.* Mr-guided focused ultrasound facilitates sonodynamic therapy with 5-aminolevulinic acid in a rat glioma model. **Scientific Reports**, v. 9, n. 10465, 2019. DOI:[10.1038/s41598-019-46832-2](https://doi.org/10.1038/s41598-019-46832-2).
- 101 KEMMERER, J. P.; OELZE, M. L. Ultrasonic assessment of thermal therapy in rat liver. **Ultrasound in medicine & biology**, Elsevier, v. 38, n. 12, p. 2130–2137, 2012. DOI:[10.1016/j.ultrasmedbio.2012.07.024](https://doi.org/10.1016/j.ultrasmedbio.2012.07.024).



## **Annex**





**ANNEX A – CERTIFICATE OF THE ETHICS COMMITTEE IN THE USE OF ANIMALS (CEUA) OF THE SAO CARLOS INSTITUTE OF PHYSICS (IFSC)**

**Figure 57** – Approval of the proposal with protocol No. 2564110719.



**IFSC** UNIVERSIDADE  
DE SÃO PAULO  
Instituto de Física de São Carlos

**COMISSÃO DE ÉTICA  
NO USO DE ANIMAIS**

### CERTIFICADO

Certificamos que a proposta intitulada "ESTUDO DOS ASPECTOS FUNDAMENTAIS DA CONJUGAÇÃO DAS TERAPIAS FOTODINÂMICA E SONODINÂMICA PARA O TRATAMENTO DE CÂNCER DE PELE NÃO-MELANOMA", protocolada sob o CEUA nº 2564110719, sob a responsabilidade de **Lilian Tan Moriyama** e equipe; *Erika Toneth Ponce Ayala; Fernanda Alves Dias de Sousa; José Dirceu Vollet Filho; Sebastião Pratavieira* - que envolve a produção, manutenção e/ou utilização de animais pertencentes ao filo Chordata, subfilo Vertebrata (exceto o homem), para fins de pesquisa científica ou ensino - está de acordo com os preceitos da Lei 11.794 de 8 de outubro de 2008, com o Decreto 6.899 de 15 de julho de 2009, bem como com as normas editadas pelo Conselho Nacional de Controle da Experimentação Animal (CONCEA), e foi **aprovada** pela Comissão de Ética no Uso de Animais da Instituto de Física de Sao Carlos - Universidade de Sao Paulo (CEUA/IFSC) na reunião de 07/08/2019.

We certify that the proposal "INVESTIGATION OF FUNDAMENTAL ASPECTS OF CONJUGATED PHOTODYNAMIC AND SONODYNAMIC THERAPIES FOR NON-MELANOMA SKIN CANCER TREATMENT", utilizing 12 Heterogenics rats (12 males), protocol number CEUA 2564110719, under the responsibility of **Lilian Tan Moriyama and team; Erika Toneth Ponce Ayala; Fernanda Alves Dias de Sousa; José Dirceu Vollet Filho; Sebastião Pratavieira** - which involves the production, maintenance and/or use of animals belonging to the phylum Chordata, subphylum Vertebrata (except human beings), for scientific research purposes or teaching - is in accordance with Law 11.794 of October 8, 2008, Decree 6899 of July 15, 2009, as well as with the rules issued by the National Council for Control of Animal Experimentation (CONCEA), and was **approved** by the Ethic Committee on Animal Use of the Physics Institute of Sao Carlos - Sao Paulo University (CEUA/IFSC) in the meeting of 08/07/2019.

Finalidade da Proposta: **Pesquisa (Acadêmica)**

Vigência da Proposta: de **07/2019** a **12/2019** Área: **Grupo de Óptica / Fcm**

Origem: **Serviço de Biotério da Prefeitura da USP - Campus de Ribeirão Preto**

Espécie: **Ratos heterogênicos**

sexo: **Machos**

idade: **8 a 12 semanas** N: **12**

Linhagem: **Wistar Hannover**

Peso: **300 a 400 g**

Local do experimento: Sala de Experimentação Animal do Grupo de Óptica

Sao Carlos, 03 de setembro de 2019

Prof. Dr. Fernando Fernandes Paiva  
Coordenador da Comissão de Ética no Uso de Animais  
Instituto de Física de Sao Carlos - Universidade de Sao Paulo

Profa. Dra. Ana Paula Ulian de Araújo  
Vice-Coordenadora da Comissão de Ética no Uso de Animais  
Instituto de Física de Sao Carlos - Universidade de Sao Paulo

**Figure 58** – Approval of the proposal amendment with protocol No. 2564110719.2



**COMISSÃO DE ÉTICA  
NO USO DE ANIMAIS**

Sao Carlos, 21 de fevereiro de 2020  
CEUA N 2564110719

Ilmo(a). Sr(a).  
Responsável: Lilian Tan Moriyama  
Área: Grupo De óptica / Fcm  
Sebastião Pratavieira (orientador)

Título da proposta: "ESTUDO DOS ASPECTOS FUNDAMENTAIS DA CONJUGAÇÃO DAS TERAPIAS FOTODINÂMICA E SONODINÂMICA PARA O TRATAMENTO DE CÂNCER DE PELE NÃO-MELANOMA".

**Parecer Consubstanciado da Comissão de Ética no Uso de Animais IFSC**

A Comissão de Ética no Uso de Animais da Instituto de Física de Sao Carlos - Universidade de Sao Paulo, no cumprimento das suas atribuições, analisou e **APROVOU** a Emenda (versão de 01/fevereiro/2020) da proposta acima referenciada.

Resumo apresentado pelo pesquisador: "Faço o pedido de emenda do projeto de pesquisa supracitado. Tal solicitação se faz necessária pelo motivo de adição de grupos experimentais. Baseando-se nos resultados obtidos até o presente momento e em estudos publicados na literatura, optou-se pela inclusão de novos grupos de estudo, a fim de avaliar e compreender novos protocolos de tratamento. Pretende-se verificar os efeitos dos seguintes protocolos: aplicação da terapia fotodinâmica e, após 1 minuto de intervalo, aplicar a terapia sonodinâmica. Da mesma forma, pretende-se avaliar o oposto: realizar a terapia sonodinâmica seguida da terapia fotodinâmica. É importante ressaltar que, para tais procedimentos, serão realizados os mesmos protocolos de anestesia, sacrifício, uso de analgésicos, manutenção e alojamento dos animais descritos no projeto inicial e já aprovados pelo CEUA. Para tal modificação experimental, necessita-se alterar o número total de animais previamente aprovados, bem como prorrogar o prazo para execução do projeto, com vigência de 07/2019 a 12/2019. Desta forma, solicitamos 9 animais extras (três novos grupos experimentais, n = 3 para cada grupo) e prorrogação do prazo de execução do projeto para Junho de 2020. "

Comentário da CEUA: "Após apreciação por parte dos relatores da CEUA/IFSC e na ausência de objeções, a emenda foi aprovada ad referendum pelo Presidente da Comissão."

Prof. Dr. Fernando Fernandes Paiva  
Coordenador da Comissão de Ética no Uso de Animais  
Instituto de Física de Sao Carlos - Universidade de Sao Paulo

Prof. Dra. Ana Paula Ulian de Araújo  
Vice-Coordenadora da Comissão de Ética no Uso de Animais  
Instituto de Física de Sao Carlos - Universidade de Sao Paulo